Physics of Fluids

Approach to select optimal cross-correlation parameters for light field particle image velocimetry

Cite as: Physics of Fluids (in press) (2022); https://doi.org/10.1063/5.0098933
Submitted: 13 May 2022 • Accepted: 15 June 2022 • Accepted Manuscript Online: 17 June 2022

Xiaoyu Zhu, Chuanlong Xu, Md. Moinul Hossain, et al.

Accepted to Phys. Fluids 10.1063/5.0098933

Approach to select optimal cross-correlation parameters for light field particle image velocimetry

Xiaoyu Zhu (朱效宇),[1] Chuanlong Xu (许传龙),[1,a)] Md. Moinul Hossain,[2] Jian Li (李健),[1] Biao Zhang (张彪),[1] Boo Cheong Khoo[3,a)]

[1] National Engineering Research Center of Power Generation Control and Safety, School of Energy and Environment, Southeast University, Nanjing 210096, China

[2] School of Engineering, University of Kent, Canterbury, Kent, CT2 7NT, UK

[3] Department of Mechanical Engineering, National University of Singapore, 119260, Singapore

[a)]Authors to whom correspondence should be addressed: *chuanlongxu@seu.edu.cn*, *mpekbc@nus.edu.sg*

Abstract: The light field particle image velocimetry (LF-PIV) has shown a great potential for three-dimensional (3D) flow measurement in space-constrained applications. Usually, the parameters of the cross-correlation calculation in the LF-PIV are chosen based on empirical analysis or introduced from conventional planar PIV, which lowers the accuracy of 3D velocity field measurement. This study presents an approach to selecting optimal parameters of the cross-correlation calculation and thereby offers systematic guidelines for experiments. The selection criterion of the interrogation volume size is studied based on the analysis of the valid detection probability of the correlation peak. The optimal seeding concentration and the size of tracer particles are then explored through synthetic Gaussian vortex field reconstruction. The optimized parameters are employed in a cylinder wake flow measurement in a confined channel. A comparative study is conducted between the LF-PIV and a planar PIV system. Results indicate that the LF-PIV along with the optimized parameters can measure the 3D flow velocity of the cylinder wakes accurately. It has been observed that the mean and max errors of velocity decrease by 32.6% and 18.8%, respectively compared to the related LF-PIV techniques without consideration of optimal parameters. Therefore, it is suggested that the optimized cross-correlation parameters in the LF-PIV can improve the accuracy of 3D flow measurement.

Keywords: 3D flow measurement, Light field PIV, Cross-correlation parameters, Valid detection probability, Cylinder wake flow

1. Introduction

Flow exists in various space-constraint industrial applications. For instance, in a turbine, the steam accelerates in the narrow stationary blades and then spins the rotating blades [1]. In a jet engine, the gas expands in the jet nozzle and injects into the atmosphere for the generation of thrust [2]. In these processes, the flows are inherently 3D and unsteady, mostly highly turbulent on a large temporal-spatial dynamic scale. For an in-depth insight into these complex flow structures, it is necessary to develop an advanced flow diagnostic technique for instantaneous 3D flow velocity measurement [3–7]. In most industrial processes, the optical access to the measurement area of internal flows is limited due to the confined space, high temperature and pressure conditions. Therefore, the volumetric velocimetry techniques with fewer optical access requirements are very attractive [8]. The particle image velocimetry (PIV) based on the light field (LF) imaging technique shows an inherent capability to measure the 3D velocity field via a single perspective [9–11]. Through the use of a lenslet-based LF camera, the depth and lateral location information of the flow field can be captured in a single snapshot, simultaneously [12]. The 3D distribution of the tracer particles in the flow can be retrieved through tomographic reconstruction techniques [13], and the flow velocity field can then be measured by analyzing the reconstructed particle motion.

In the LF-PIV, the particle displacement between two successive frames is determined by the cross-correlation calculation. In principle, the measurement volume is divided into box-like interrogation volumes, and the cross-correlation coefficient is then calculated for the same interrogation volume at two instants. The mean displacement in each interrogation volume is estimated by locating the peak of the correlation coefficient [14]. The probability that the located correlation peak corresponds to the true particle displacement is defined as the valid detection probability (VDP) [15]. The VDP is closely related to the cross-correlation parameters, including the interrogation volume size, tracer particle properties and time interval between two successive frames [16,17]. Studies have indicated that a VDP of 95% should be achieved in the cross-correlation calculation to avoid clusters of erroneous displacement vectors in the velocity measurement [18,19]. To achieve that, in the planar-PIV, it is recommended that the selection of the two-dimensional (2D) interrogation window should follow the ‘one-quarter rule’ [20], that is, limiting the local particle displacement to one-quarter of the interrogation window dimension. Moreover, the paired particle number within each interrogation window should be kept greater than 6 to perform robust cross-correlation calculations [21]. To avoid the peak locking effect in locating the correlation peak and keep a high contrast of the particle images, a particle image diameter of 2 to 3 pixels is preferred [22]. The measurement area should be placed in the focal plane of the camera and thus the particle images are captured in focus [23]. Furthermore, a short time interval between two successive recordings is required for the accurate measurement of the instantaneous velocity field [24], otherwise, significant errors will be produced due to the flow acceleration or curved streamlines. The lower limit of the time interval is usually determined by the dynamic velocity range (DVR) [25].

The aforementioned criteria of the cross-correlation parameters have been extensively validated in the planar-PIV studies [26–30]. However, due to the differences in the measurement principles between the LF-PIV and the planar-PIV, the applicability of these criteria in the LF-PIV faces some challenges to select optimal cross-correlation parameters. For examples;

(i) *Tracer particle properties*: Different from the planar-PIV that the particle displacement is

extracted from the particle raw images, in the LF-PIV, the 3D particle motion analysis is based on the reconstructed particle distributions. Thus, the achievable VDP in the cross-correlation calculation is largely dependent on the reconstruction accuracy of the particle location. Studies indicated that the reconstruction accuracy is greatly influenced by the tracer particle concentration [31,32]. A very dense concentration of the tracer particles degrades the reconstruction accuracy significantly [33]. Therefore, the tracer particle concentration should be determined by balancing the trade-off between the accuracy of the particle reconstruction and the robustness of the cross-correlation algorithm. In addition to the particle concentration, the reconstruction accuracy is also affected by the particle size. It has been demonstrated that severe elongation effects can be produced in particle reconstructions with the use of large tracer particles [34,35], which subsequently decreases the accuracy in locating the correlation peak. Therefore, the selection of the particle size should also consider its effects on particle reconstruction accuracy.

(ii) *Interrogation volume size*: To alleviate the loss-of-pair effect [21,36], which leads to a drastic decrease in the VDP, the upper limit of the ratio of the local particle displacement to the interrogation volume size should be determined. Although the 3D cross-correlation calculation is regarded as an extension of the 2D cross-correlation, whether the 'one-quarter rule' can be extended to the third direction (i.e., depth) remains to be verified according to the achievable VDP. Besides, as the VDP is related to the number of particles in each interrogation volume, the criterion of the interrogation volume size should be given at different particle concentrations. Hence the spatial resolution of the velocity measurement can be optimized with the assurance of accuracy.

(iii) *Location of the measurement volume*: In the LF-PIV, studies have indicated that the particle reconstruction accuracy is also dependent on the LF imaging resolution and varies significantly with the image depths [37,38]. Therefore, the measurement volume should be located in the high-resolution depth zone to facilitate an accurate velocity measurement. It has been demonstrated that the imaging resolution is lowest near the nominal focal plane of a LF camera [39], hence the criterion in the planar-PIV is not applicable in the LF-PIV and the measurement volume should be away from the focal plane. The optimal location of the measurement volume remains to be explored.

(iv) *Time interval between two frames*: In the LF-PIV, the imaging resolution should be considered for the selection of the time interval between two successive frames. This is due to the trade-off in the LF imaging that the lateral spatial resolution is sacrificed for recording the directional information of the incoming light rays [40,41], which is then used to retrieve the depth locations of the particles [42,43]. Therefore, the time interval should be large enough to ensure that the particle motions can be resolved from the LF images. Otherwise, the reconstructed particle fields from two successive frames will be the same. Furthermore, the selected time interval should also allow a low-velocity measurement uncertainty [44].

This study aims to investigate the effects of the cross-correlation parameters on the LF-PIV measurement accuracy and to provide a fundamental guideline for the optimum parameter selection for cross-correlation calculation, thus improving the accuracy of 3D flow velocity measurement. Firstly, the selection criterion of the interrogation volume size is studied based on the VDP analysis

in the 3D cross-correlation calculation. Secondly, the optimal particle concentration and size, as well as the measurement volume location are determined through numerical reconstructions of the 3D motion field around a Gaussian vortex ring. Finally, all the selected cross-correlation parameters are employed in the experimental measurements of the cylinder wake flow in a confined channel. The accuracy of velocity measurement is quantitatively evaluated and compared with the planar-PIV. The flow characteristics of the confined cylinder wakes are further analyzed.

2. Principle of light field PIV

The LF-PIV technique measures the flow velocity by following the principle

$$V = \Delta X / \Delta t \tag{1}$$

i.e., the ratio of the tracer particle displacement (ΔX) to the time interval between two successive frames (Δt) returns the velocity (V). To achieve that, the 3D particle distributions are firstly reconstructed from the LF raw images and the displacement field can then be estimated through the 3D cross-correlation calculation. The working principle of the LF-PIV is illustrated in Fig. 1.

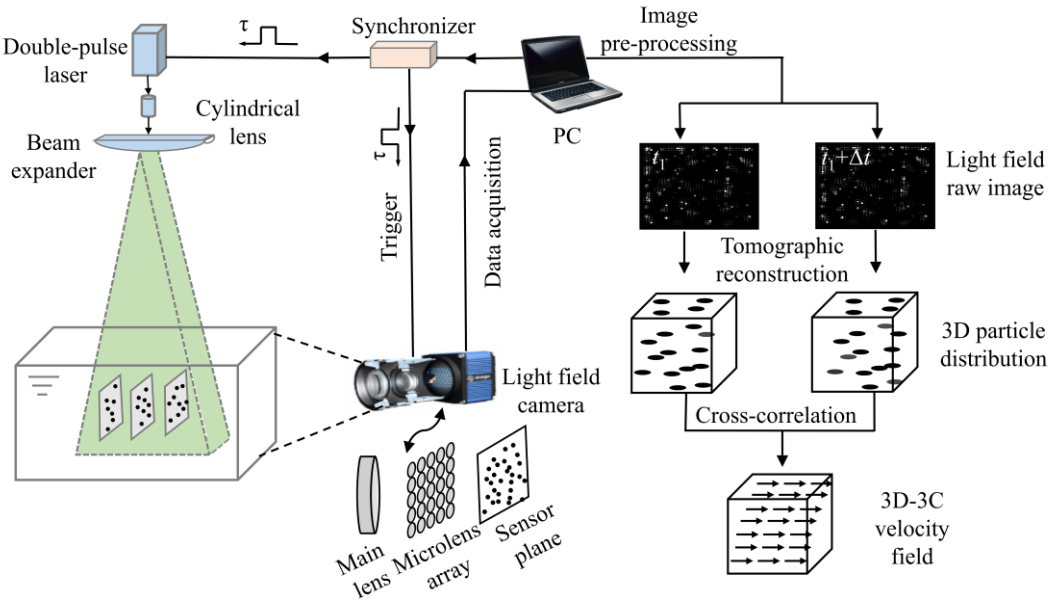

Fig. 1 Working principle of the LF- PIV.

The novel aspect of the LF-PIV technique lies in the imaging process of the 3D flow field. With the insertion of a dense microlens array (MLA) in front of the image sensor, the 4D light field information of the flow can be recorded via a single snapshot. Fig. 2 illustrates the principle concept of LF imaging. In this figure, four rays (depicted in different colors) are emitted in different directions from the object's point. The rays pass through the main lens and focus on a microlens firstly, and the microlens redirects the light rays further to different pixels on the image sensor. In this process, the positions and directions of the light rays are registered on the MLA and the pixels behind each microlens, respectively. A detailed description of the LF imaging can be found elsewhere in [12,45].

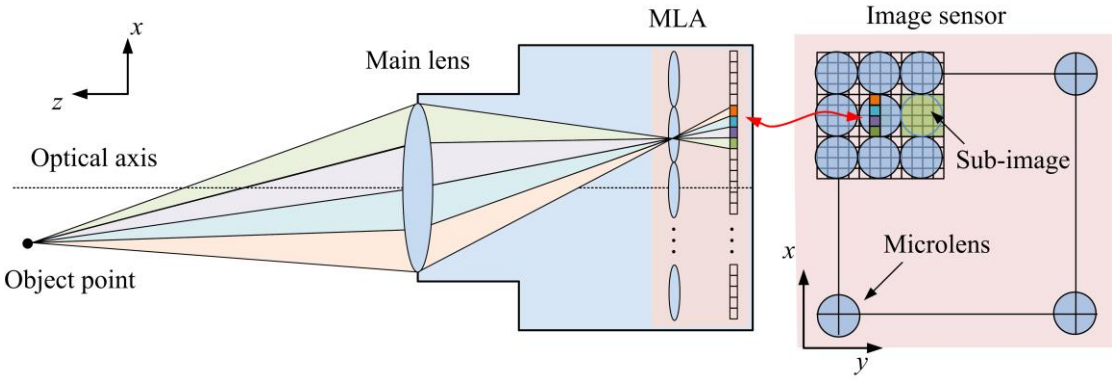

Fig. 2 Principle concept of LF imaging.

In the LF-PIV, the intensity of an image pixel is formed by the intensity projection of the 3D measurement volume. For ease of representation, the measurement volume is typically discretized as the cubic voxel elements, and the relation of the intensities between the voxels and pixels can then be written as a linear equation defined as follows:

$$\sum_{j\in N_i} w_{i,j} E\left(X_j, Y_j, Z_j\right) = I\left(x_i, y_i\right) \tag{2}$$

where $E\,(X_j, Y_j, Z_j)$ and $I\,(x_i, y_i)$ denote the intensity of the j_{th} voxel and the i_{th} pixel, respectively, N_i denotes the voxel number in the line-of-the-sight of the i_{th} pixel, $w_{i,j}$ is the weight coefficient that describes the intensity contribution of the j_{th} voxel to i_{th} pixel. With the acquired LF images of the flow field, tomographic reconstruction algorithms [13] will be employed to reconstruct the particle locations. The required weight coefficients can then be calculated by the ray-tracing methods as described in [46,47].

To estimate the particle displacements, the 3D cross-correlation calculation can be carried out subsequently with the reconstructed particle distributions. To achieve that, the measurement volume is divided into box-like interrogation volumes and the normalized cross-correlation coefficient R in each pair of interrogation volumes is calculated as [48]

$$R(l,m,n) = \frac{\sum_{i,j,k=1}^{I,J,K} E(i,j,k,t) \times E(i-l, j-m, k-n, t+\Delta t)}{\sqrt{\sum_{i,j,k=1}^{I,J,K} E(i,j,k,t)^2 \times \sum_{i,j,k=1}^{I,J,K} E(i,j,k,t+\Delta t)^2}} \tag{3}$$

where E denotes the intensity distribution in the interrogation volume, (I, J, K) denotes the total voxel numbers in the x, y and z-directions, (i, j, k) denotes the number of a discrete voxel, and (l, m, n) denotes the 3D displacement in voxels. R is from -1 to 1, and a larger R corresponds to a high correlation. The mean displacement within the interrogation volume is estimated as the peak location of the cross-correlation coefficient. According to Eq. (3), several parameters can affect the calculation result of the cross-correlation coefficient and hence the measurement accuracy of the velocity field. These parameters mainly include the time interval between two successive frames, the interrogation volume size, the tracer particle properties, and the location of the measurement volume. Therefore, it is important to optimize these cross-correlation parameters carefully for accurate velocity measurement. The selection processes are discussed in Section 3.

3. Selection of optimum cross-correlation parameters

3.1 Time interval between two frames

In the PIV technique, the time interval between two frames (Δt) should be firstly adapted to the flow of interest to ensure that the estimated displacement ΔX can represent the actual particle trajectory. If the time interval is too long, bias errors may be caused by the curved streamlines or accelerations. An example is illustrated in Fig. 3, for the short time interval Δt_1, the estimated displacement demonstrates the travel path of the particle in a good approximation. However, for the larger time interval Δt_2, the estimated particle displacement is significantly different from the actual streamline. From this perspective, prior knowledge of the similar test flow achieved by the computational fluid dynamics (CFD) [49–51] or other experimental flow diagnosis techniques [52–55] is required, which helps to understand the unsteady flow characteristics and determine the upper limit of the time interval (Δt_{up}) for LF-PIV recordings.

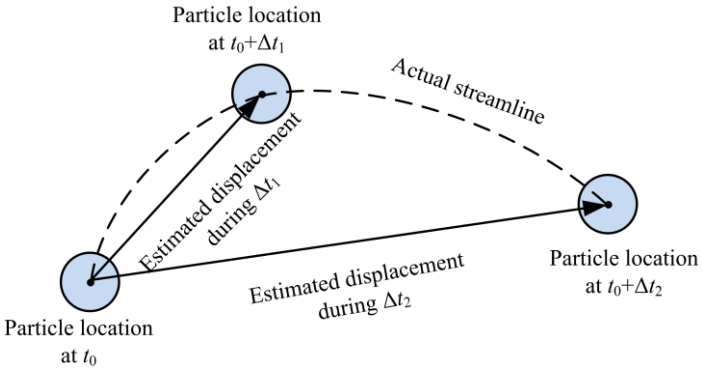

Fig. 3 Example of estimated particle displacements and actual particle trajectories.

The lower limit of the time interval should consider the limitation of the imaging resolution and ensure that the particle motions can be resolved by the LF camera. Fig. 4 shows two LF images of the cylinder wakes at the Reynolds number (Re_d) of 40 (i.e., based on the free-stream velocity and cylinder diameter). The time interval between two frames is 0.1 ms. Theoretically, the reverse flow behind the cylinder is formed at this Re_d [56]. However, only the large particle displacements in the acceleration region (marked by circles) are observed, whereas the small displacements in the wake flow (marked by rectangles) cannot be resolved accurately from the LF images. Thus, the time interval of 0.1 ms is too short to investigate the wake flow structures. Therefore, the lower limit of the time interval (Δt_{low}) for LF-PIV recordings should be

$$\Delta t_{low} > Res / v_f \tag{4}$$

where Res denotes the resolution of the LF imaging, and v_f denotes the free-stream velocity of the flow of interest. The lateral spatially resolution (Res_l) of an unfocused LF camera can be calculated as

$$Res_l = p_m / |M| \tag{5}$$

where M denotes the main lens magnification and p_m denotes the microlens pitch (typically 10 to 30 times larger than the pixel). The depth resolution (Res_d) of a LF camera is lower than the lateral resolution and varies significantly with the depth. More details about the quantitative

characterization of the LF imaging resolution can be found in [39].

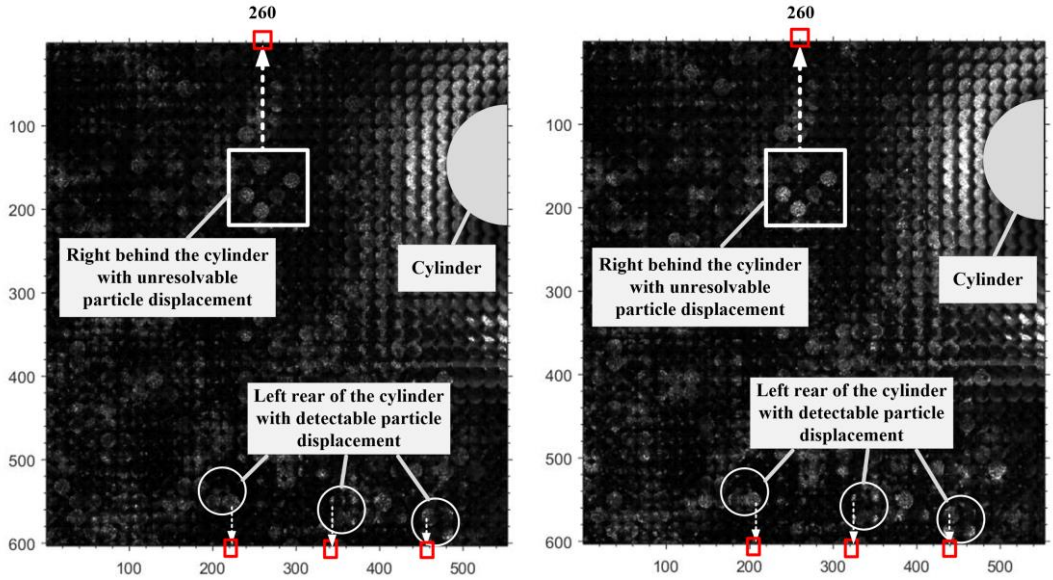

(a) LF image at time t_0 (b) LF image at time t_0 + 0.1ms

Fig. 4 LF images of the cylinder wake flow captured at (a) time t_0 and (b) time t_0 + 0.1ms. The coordinate unit in the figures is in pixels.

Once the lower and upper limits are determined, Δt should be optimized further to achieve low measurement uncertainty. The relative uncertainty in the velocity measurement can be characterized by the dynamic velocity range (DVR) defined as [26]

$$\mathrm{DVR}=\Delta X_{\max}/\sigma_{\Delta x} \tag{6}$$

where $\Delta X_{\max}$ denotes the maximum particle displacement between two frames, $\sigma_{\Delta x}$ denotes the precision in locating the correlation peak and it is fixed for a PIV measurement system. A large DVR corresponds to a low measurement uncertainty [44,57]. According to Eq. (6), a large time interval (between the lower and upper limits) is preferred in experiments to acquire velocity measurement results with low uncertainty.

3.2 Size of interrogation volume

In the LF-PIV, the particle displacement during the time interval between two successive frames is calculated via the cross-correlation calculation [Eq. (3)]. The probability that the detected correlation peak corresponds to the true particle displacement is called valid detection probability (VDP), which is closely related to the size of the interrogation volume. Small interrogation volumes may cause the loss-of-pairs effect, which further leads to the generation of random correlation peaks and hence the erroneous vectors. Large interrogation volume allows 100% VDP, but the spatial resolution of the generated velocity vector decreases accordingly. A previous study indicates that a VDP of 95% is usually a good compromise between accuracy and resolution [21]. To determine the appropriate interrogation volume size, a 3D measurement volume is constructed and discretized as 512×512×512 cubic voxels. Tracer particles are seeded in the measurement volume by randomly setting the locations of voxels with intensity. With the acquired particle distribution at instant t_1, a uniform particle motion field that contains uniform displacement in three directions (displacement unit is in voxels) is then employed to generate a new particle distribution at instant t_2. The normalized cross-correlation coefficients between the particle intensity distribution at t_1 and t_2 are

calculated through Eq. (3).

An example of the calculated result is shown in Fig. 5. In this figure, the 3D interrogation volumes are simplified to 2D boxes (in green) for easier interpretation. The grey values in each box represent the normalized correlation coefficients at different locations. A darker point corresponds to a larger correlation coefficient. As the particle displacements in x, y and z-directions are given, thus the theoretical peak location that corresponds to the true particle displacement can firstly be determined (marked with a blue square). In addition to the theoretical peak location, somewhere else in the interrogation volume that has the highest correlation coefficient can also be found. This location is called the secondary peak location (marked with a red circle). Theoretically, the correlation coefficient at the theoretical peak location (R_1) should always be larger than that at the secondary peak location (R_2). However, it can be seen from Fig. 5 that R_1 is sometimes smaller than R_2 (see the boxes with dotted lines). Under this case, the correlation peak is detected as the secondary peak location rather than the theoretical peak location. The erroneous displacement vector is hence returned.

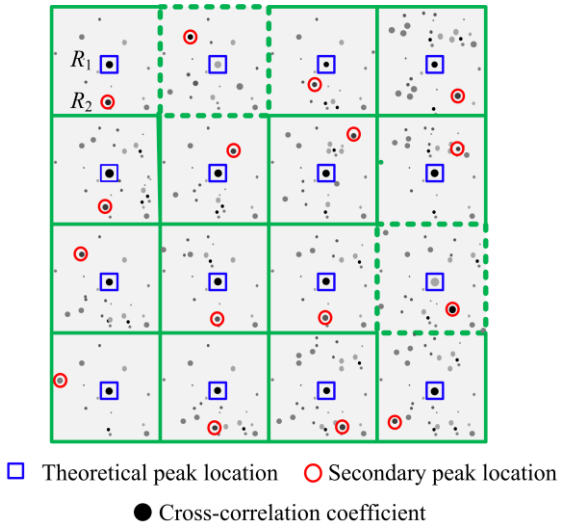

Fig. 5 An example of the normalized cross-correlation coefficient calculated result.

The overall VDP in the cross-correlation calculation can be calculated as

$$\mathrm{VDP} = \int_0^1 pdf_2(R_2) \times \int_{R_2}^1 pdf_1(R_1)\, dR_1 dR_2 \tag{7}$$

where pdf_1 and pdf_2 denote the probability density function of R_1 and R_2 in all the interrogation volumes, respectively. Fig. 6 illustrates the distributions of pdf_1 (orange bars) and pdf_2 (green bars) under the same interrogation volume size (I_s) but with different particle displacements (DIR, i.e., ratio of the particle displacement to the interrogation volume size). The particle numbers per interrogation volume (N_I) are fixed at 20. It can be seen from Fig. 6 (a) that for a small particle displacement that DIR is 6.3%, the correlation coefficient at the theoretical peak location (R_1) is always larger than that at the secondary peak location (R_2). The corresponding VDP reaches 100%, indicating that the detected correlation peaks at all the interrogation volumes match well with the true particle displacements. In contrast, for a larger DIR of 37.5%, Fig. 6 (b) shows that R_1 decreases significantly and is even smaller than R_2. As a result, the overall VDP decreases to 66.8% accordingly.

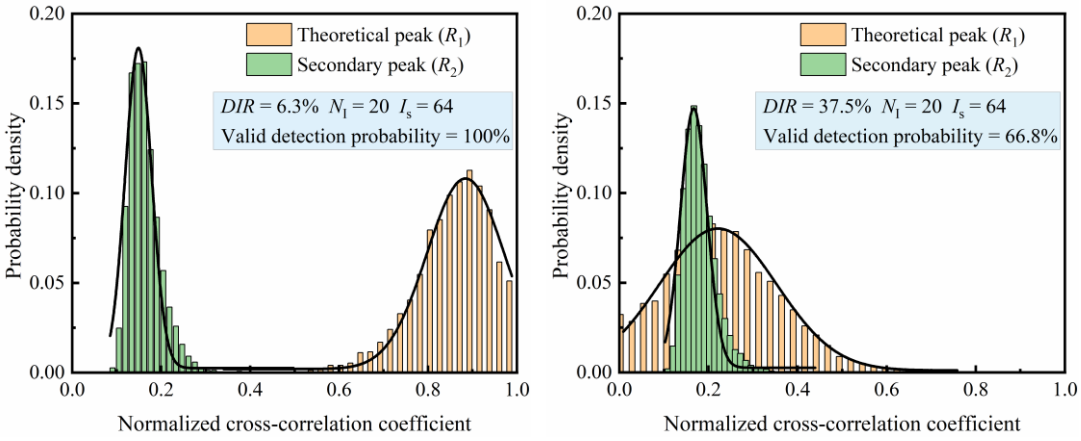

(a) DIR = 6.3%, VDP = 100% (b) DIR = 37.5%, VDP = 66.8%

Fig. 6 Probability density distribution of the normalized correlation coefficient at the theoretical peak (R_1) and secondary peak (R_2). The DIR is set as (a) 6.3% and (b) 37.5%, and the corresponding VDP is 100% and 66.8%, respectively.

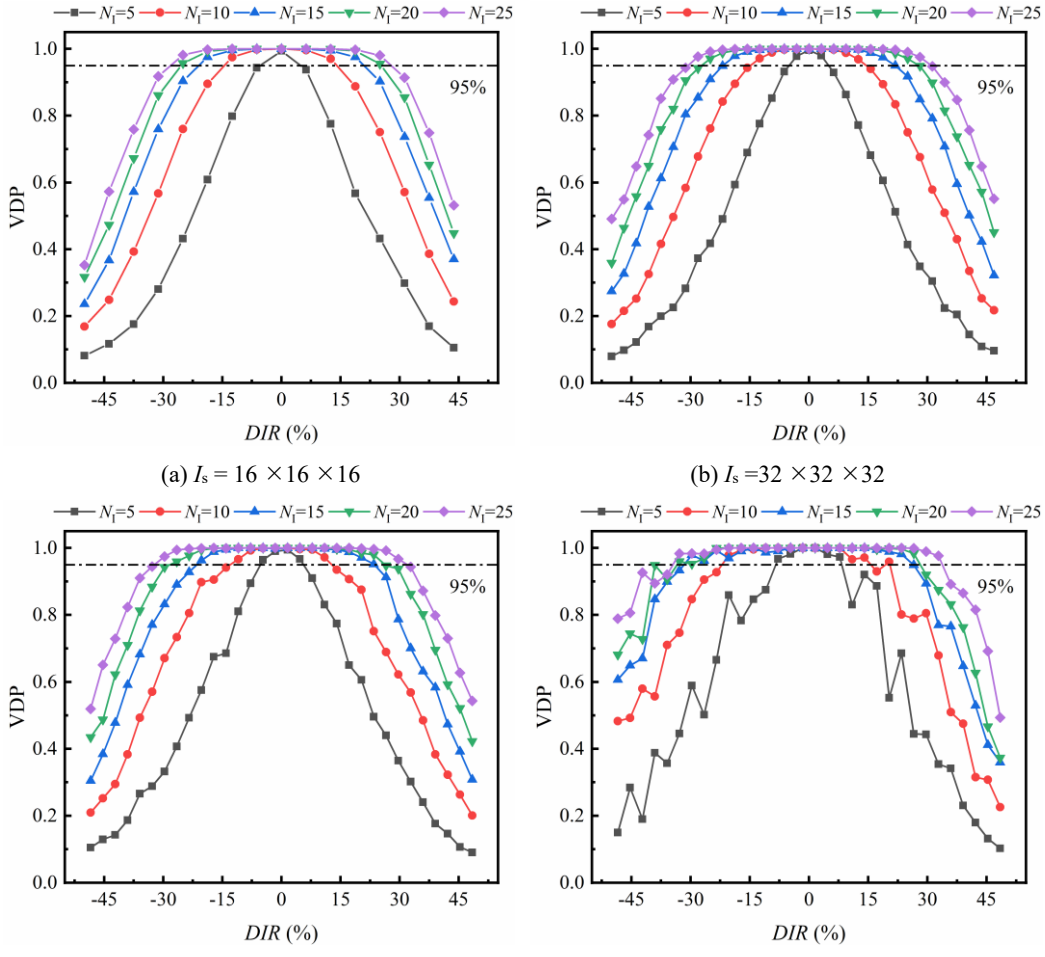

(a) I_s = 16 ×16 ×16 (b) I_s =32 ×32 ×32

(c) I_s = 64 ×64 ×64 (d) I_s = 128 ×128 ×128

Fig. 7 Variation of the VDP with DIR and N_I. The recommended VDP of 95% from [21] is adopted to select the proper DIR. The interrogation volume size I_s is set as (a) 16 ×16 ×16, (b) 32 ×32 ×32, (c) 64 ×64 ×64, and (d) 128 ×128 ×128 voxels.

The variation of the VDP with the particle displacement (*DIR*) and particle number per interrogation volume (N_I) is illustrated in Fig. 7. The negative and positive *DIR* denotes the direction of displacement. The VDP decreases sharply from 100% to 10% with the increase of *DIR* from 0 to 45%, indicating that a small particle displacement is preferred for accurate localization of the correlation peak. Fig. 7 also shows that the VDP is closely related to the particle number. A larger number of particles facilitate a higher VDP at a certain particle displacement. To achieve a VDP of 95% for accurate velocity measurement [21], the upper limits of *DIR* at different particle numbers are obtained through linear interpolation. The results are summarized in Table 1. From Table 1, it can be concluded that the 'one-quarter rule' proposed in the planar PIV can also be extended to the 3D cross-correlation calculation but should be with the premise that the particle number in each interrogation volume (N_I) exceeds 20. For the case that N_I = 15, 10 and 5, the corresponding *DIR* should not exceed the limit of 20.9%, 13.2% and 5.1%, respectively.

Table 1. Upper limits of *DIR* at different interrogation volume sizes (I_s) and particle numbers (N_I)

I_s	N_I				
	5	10	15	20	25
16	5.1%	14.2%	20.9%	25.4%	28.1%
32	5.1%	14.9%	22.2%	27.5%	30.9%
64	5.5%	13.2%	22.7%	27.3%	32.3%
128	8.4%	18.9%	28.9%	30.9%	34.1%

Once the upper limit of *DIR* is determined, the spatial resolution of the measured velocity field is further considered for the selection of interrogation volume. As suggested in [25], the range of resolvable flow scales in PIV measurement can be characterized by the dynamic spatial range (DSR) defined as

$$\mathrm{DSR} = X_m / X_i \tag{8}$$

where X_m and X_i denote the physical size of the measurement volume and interrogation volume, respectively. For instance, for a 16 mm×16 mm×16 mm measurement volume with the interrogation volume size of 0.32 mm×0.32 mm×0.32 mm, the resulting DSR will be 50. This corresponds to a 50 mm length tape with a scale of 1 mm. To provide dense velocity data for measurement of multi-scale flow structures, a large DSR and hence a relatively small interrogation volume that can meet the requirement of *DIR* (criteria in Table 1) is preferred.

3.3 Concentration and size of tracer particle

With the selection of the interrogation volume, the optimal seeding concentration and size of the tracer particle are further studied. Theoretically, a single pair of tracer particles can generate a detectable correlation peak in the interrogation volume. However, it has been demonstrated in Fig. 7 that insufficient particle leads to a decreased VDP and hence the erroneous displacement vectors. More importantly, the returned displacement vector is inherently a spatially filtered result that represents the mean particle displacement in the interrogation volume [18]. Therefore, insufficient particles may cause significant measurement errors. However, it does not mean that a very dense seeding will correspond to an accurate velocity measurement since the particle concentration also greatly affects the particle reconstruction accuracy in the LF-PIV. Studies [39,58] have indicated

that the elongation effect demonstrated in the particle reconstruction becomes more significant as the particle concentration gets denser, which subsequently degrades the velocity measurement accuracy [34]. Therefore, the optimal particle concentration should balance the trade-off between the particle reconstruction accuracy and the required particle number (for the robustness of the cross-correlation calculation).

In the selection of the tracer particle size, the flow and light scattering properties of the particles must be considered. The small particles can follow the flow with high fidelity [26], while the large particles enable the PIV recordings with high contrast. To balance this trade-off, the previous study [48] suggested that the fog droplets or TiO_2 particles with a diameter of 1 to 5 μm can be used in the gas flow measurement, while the glass spheres with a diameter of 10 to 50 μm can be employed in liquid flow measurement. In the LF-PIV, the particle size also affects the elongation lengths of the reconstructed particles [35] and hence the accuracy of the displacement estimation. From this perspective, the particle size that can alleviate the reconstruction elongation effect is preferred in the LF-PIV.

To investigate the optimal particle concentration and size for the LF-PIV measurement, numerical reconstructions are carried out. The 3D motion field around a Gaussian vortex ring is reconstructed using synthetic LF images. The optical parameters of the LF camera, which is employed to generate the synthetic LF images are listed in Table 2. For the generation of the synthetic LF images, the measurement volume is discretized into the cubic voxels, and different seeding concentrations are realized by changing the number of voxels with intensity. As the synthetic LF images are generated through the ray-tracing method, the particle size is simulated by setting the sub-area of a voxel as the starting point of the ray tracing. More details about the generation of the synthetic LF image can be found in [31,37].

Table 2: Numerical setting of the LF camera parameters

Symbol	Parameter	Value
M	Magnification ratio of the main lens	-1
F_m	Focal length of the main lens	100 mm
$F/\#$	f-number of the main lens	4
P_m	Aperture diameter of the main lens	25 mm
f_m	Focal length of the microlens	0.8 mm
$f/\#$	f-number of microlens	8
p_m	Microlens pitch	0.1 mm
n_x, n_y	Number of microlens on MLA	151×151
p_x	Pixel size	5.5 μm
N_x, N_y	Camera resolution	2501×2501

The analytical expression of the Gaussian vorticity field is given by [59]

$$\Omega(i,j,k)=\frac{\Gamma}{\pi R_c^2}\exp\left[-\frac{(k-z_c)^2+\left(\sqrt{(i-x_c)^2+(j-y_c)^2}-R_0\right)^2}{{R_c}^2}\right] \tag{9}$$

where Ω (i, j, k) is the vorticity magnitude at the location (i, j, k), (x_c, y_c, z_c) is the location of the vortex center (also the measurement volume center), R_c and R_0 are the core radius and outer-ring

radius, respectively, Γ is the circulation. The numerical settings of R_c, R_0, Γ, the measurement volume size (X_m), the particle concentration (C) and size (d_p) are summarized in Table 3. A maximum particle displacement of 3.2 voxels is yielded. Note that since the lateral resolution of the LF camera is governed by the pitch of microlens, the unit of the particle concentration is particle per microlens (ppm) in this study.

Table 3: Numerical settings of the measurement volume and 3D motion field

Symbol	Parameter	Value
X_m	Measurement volume size	$12\times12\times10$ mm^3
N_m	Discrete voxel number	$240\times240\times100$ voxels
R_c	Core radius of Gaussian vortex	25 voxels
R_0	Outer-ring radius of Gaussian vortex	60 voxels
Γ	Circulation of Gaussian vortex	100 voxels
C	Seeding concentration	0.1 ~ 1 ppm
d_p	Particle diameter	10 ~ 50 μm

For reconstruction of the displacement field around the vortex ring, the 3D particle distributions are firstly reconstructed by the pre-recognition simultaneous algebraic reconstruction technique (PR-SART) [33]. The cross-correlation calculation is then performed with the interrogation volume size of $16\times16\times16$ voxels and the overlap of 50%. A total of $30\times30\times12$ velocity vectors are returned in the displacement field. All these numerical calculations are performed on a 44-core workstation by parallel computing (Intel Xeon E5-2696 v4 at 2.2 GHz, 128 GB of RAM, 1 TB solid-state disk).

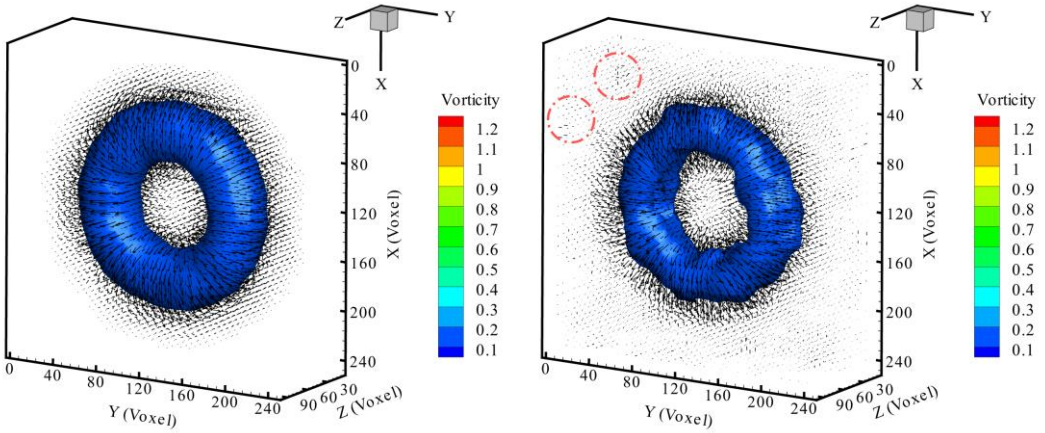

(a) Theoretical distribution (b) Reconstructed

Fig. 8 Reconstructed vorticity field of Gaussian vortex ring. (a) Theoretical distribution is generated from the analytical expression. (b) Reconstructed from the synthetic LF images. The iso-surface of vorticity magnitude (Ω) is 0.12 voxels/voxel. The vectors indicate the displacement distribution.

Fig. 8 shows an example of the reconstructed vorticity field at C = 1 ppm and d_p = 10 μm. The actual vorticity field generated from the analytical expression [Eq. (8)] is also illustrated in this figure for comparison. The x and y-axis correspond to the lateral directions, and the z-axis corresponds to the depth direction. It can be observed from Fig. 8(b) that the torus-shaped vorticity field has been reconstructed, although it has some defects such as not round as the actual one.

Furthermore, some spurious vectors are shown around the ring vortex (in red circles).

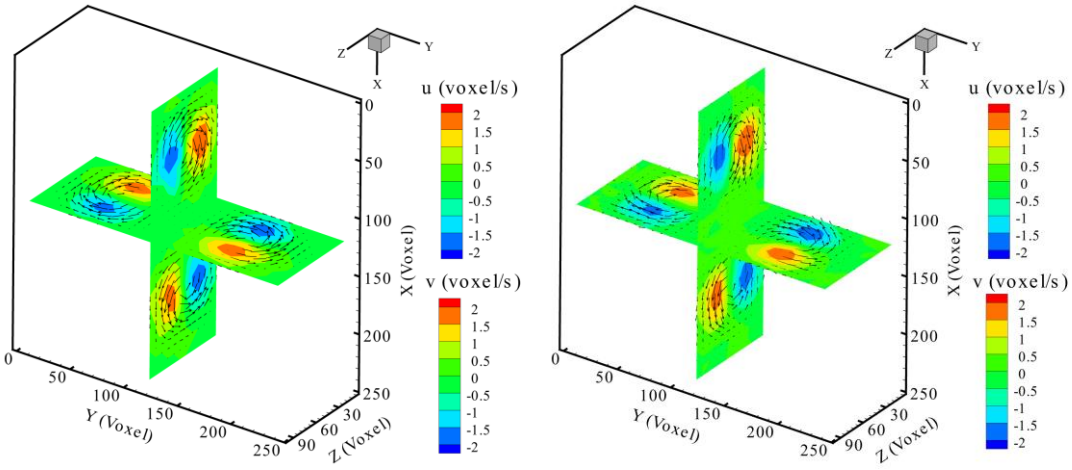

(a) Theoretical distribution (b) Reconstructed

Fig. 9 *u* component of displacement on the central *x*-*z* slice (*y* = 120 voxels) and *v* component of displacement on the central *y*-*z* slice (*x* = 120 voxels). (a) Theoretical distribution. (b) Reconstructed result. The unit is in voxels.

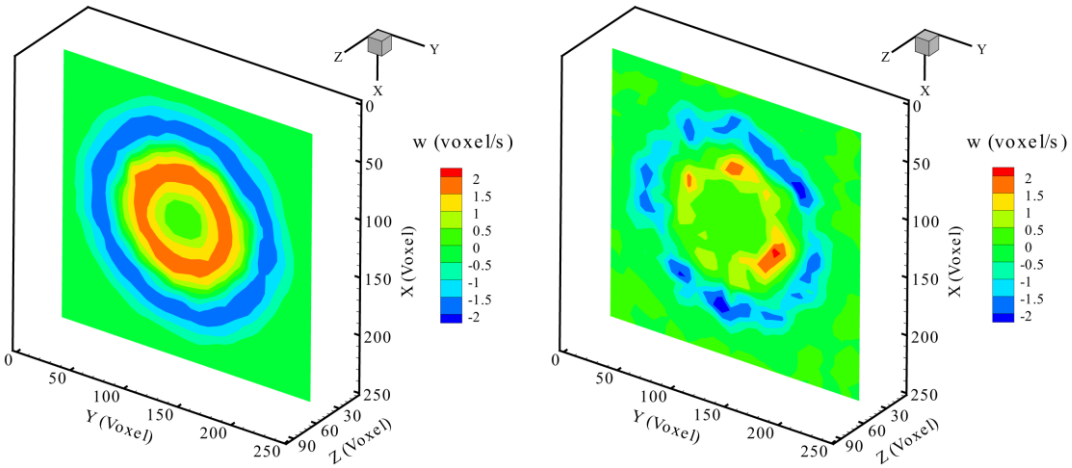

(a) Theoretical distribution (b) Reconstructed

Fig. 10 *w* component of displacement on the central *x*-*y* slice (*z* = 51 voxels). (a) Theoretical distribution. (b) Reconstructed result. The unit is in voxels.

Further comparisons are performed by extracting *u*, *v,* and *w* components of the displacement on different cross-sections. Fig. 9 shows the distributions of *u* component on the central *x*-*z* slice and the *v* component on the central *y*-*z* slice. Fig. 10 illustrates the distribution of the *w* component on the central *x*-*y* slice. It can be seen from Fig. 9 that the reconstructed *u* and *v* components show good consistency with the theoretical distribution. Four symmetrical structures are presented. However, the reconstructed *w* component shows a noticeable difference from the theoretical distribution. The outer and inner ring structures haven't been reconstructed completely. The degraded reconstruction accuracy of the *w* component is mainly attributed to the reconstruction location error and particle elongation effect in the depth direction (*z*).

The reconstruction accuracy of displacement is quantitatively evaluated through the root mean

square error (RMSE) by taking the analytical solution [Eq. (8)] as the ground truth. The RMSE of u, v, and w components at different particle concentrations (C) and sizes (d_p) are depicted in Fig. 11 (a), (b) and (c), respectively. At first glance, the RMSE of u, v and w components varies contrarily with the seeding concentration. A dense seeding allows accurate reconstruction of u and v components but results in large errors in the w component. Theoretically, the larger particle number should improve the detection accuracy of the correlation peak, as illustrated in Fig. 7. However, this is only applicable to the lateral directions of the reconstructed particle field, as severe particle elongations along the depth can be produced at the dense particle concentration. As a result, the particle displacement in depth is damped out in the cross-correlation calculation. This has been demonstrated in the scatter plot of u and w components errors (Δu and Δw) in Fig. 12. It can be found that the distribution of Δu is nearly on the symmetry of $\Delta u = 0$, whereas most of the Δw is negative, indicating that the estimated w components are smaller than the actual values. Fig. 11 (c) also shows that small particle size is preferred for accurate measurement of the w component. This can also be explained from the view of the particle reconstruction that the elongation effect can be largely alleviated with the use of the small particles.

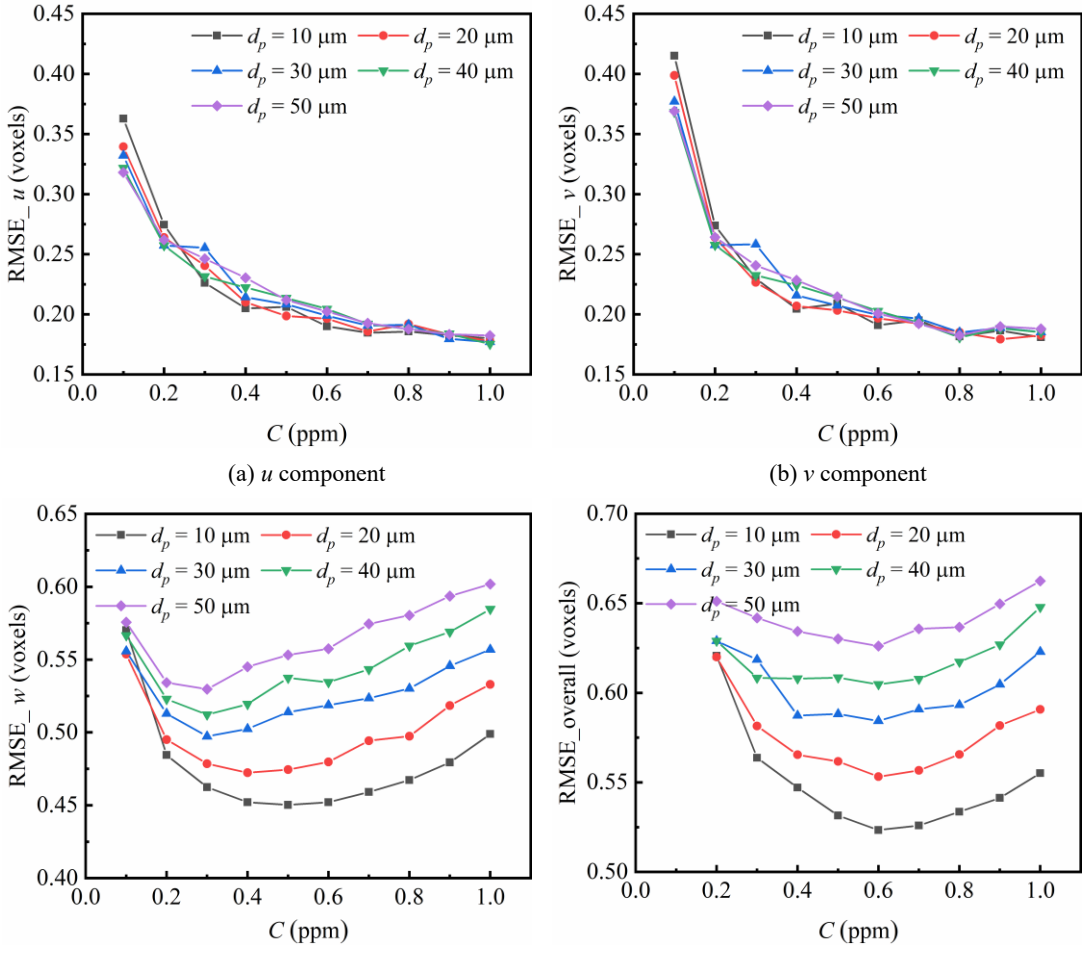

(a) u component (b) v component

(c) w component (d) Overall

Fig. 11 RMSE of the reconstructed displacement at different seeding concentrations and particle sizes. (a) RMSE of u component. (b) RMSE of v component. (c) RMSE of w component. (d) Overall RMSE.

The optimal seeding concentration and particle size are determined based on the overall RMSE

(i.e., RMSE in all three components) depicted in Fig. 11 (d). It can be concluded that the particle diameter of 10 μm and the seeding concentration of 0.6 ppm is preferred, as the reconstruction accuracy of the 3D displacement field is highest in this case. Due to the insufficient particles and severe reconstruction elongation effect, the larger RMSE can be seen at the sparse (e.g., $C < 0.4$ ppm) and dense (e.g., $C > 0.8$ ppm) seeding concentration, respectively.

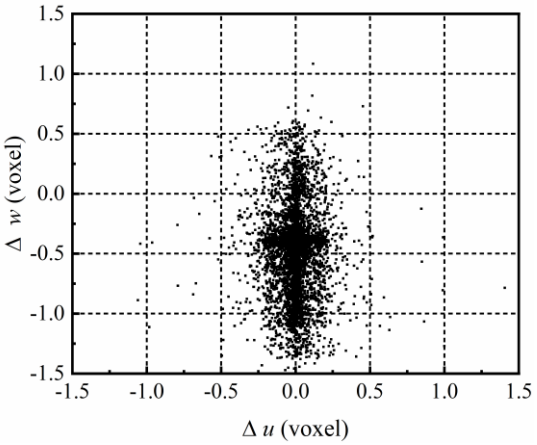

Fig. 12 Reconstruction errors of u and w component at C = 1 ppm and d_p = 10 μm.

3.4 Depth location of measurement volume

In the LF-PIV, the particle reconstruction accuracy is affected by the LF imaging resolution, which varies significantly with the depth location. Thus, the measurement volume should be arranged in the high-resolution zone to achieve an accurate velocity measurement. To investigate the optimal location of the measurement volume, the numerical reconstruction of the Gaussian ring vortex is further carried out by varying the distance of the measurement volume to the LF camera. Specifically, the center of the measurement volume is traversed along the optical axis from the inner focal side (z = -20 mm) to the outer-focal side (z = 20 mm) with a constant step-interval of 2 mm. The optimal seeding concentration of 0.6 ppm and particle size of 10 μm is adopted to reconstruct the measurement volume at different locations.

Fig. 13 illustrates the effect of the measurement volume location on the displacement reconstruction accuracy. It can be found that for the measurement volume that the center is located at z = -10 mm (Fig. 13 (a)), the ring structure of the w component has been reconstructed. In contrast, for the measurement volume that the center is at the focal point (i.e., z = 0 mm), the reconstructed ring structure can hardly be perceived. The degraded reconstruction accuracy is mainly due to the inferior depth resolution of the LF camera around the focal plane [39].

The variation of the RMSE of the reconstructed displacement with the central location of the measurement volume is depicted in Fig. 14. It can be found that the RMSE of u and v components is constant of 0.2 voxels in the depth range of -20 mm < z < 20 mm. In contrast, the RMSE of the w component varies remarkably with the depth. The peak value emerges at the focal point and decreases sharply on both sides. The variation of the overall RMSE is quite like the w component. A relatively smaller RMSE is achieved when the measurement volume center is located at the depth range of -10 mm < z < -6 mm. It is suggested that the whole measurement volume should be away from the focal plane and therefore z = -10 mm becomes an optimal choice for the center of the measurement volume (with a typical depth range of $d_{th} \leqslant 20$ mm). For the measurement volume

with a larger depth range, the particles are difficult to reconstruct accurately by a single LF camera due to the serious overlaps of the particle images. In this case, an additional LF camera should be considered [34].

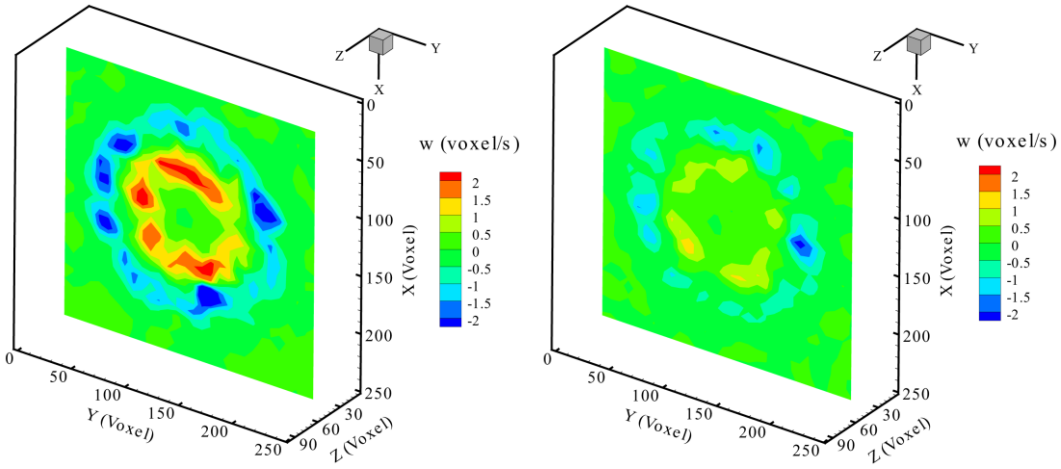

(a) Center at z = -10 mm (b) Center at z = 0 mm

Fig. 13 Reconstructed w component distribution on the central x-y slice. The center of the measurement volume is located at (a) z = -10 mm and (b) z = 0 mm.

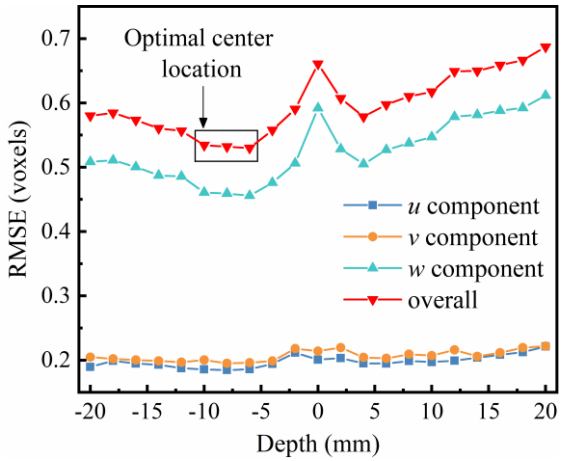

Fig. 14 Variation of the RMSE of the reconstructed displacement with the central location of the measurement volume. Negative and positive depths denote the inner and outer focal sides of the LF camera, respectively.

4. Experiments on a confined cylinder wake flow

4.1 Physical implementation

To evaluate the performance of the LF-PIV with the optimum parameters, experiments on a wake flow behind a confined cylinder are conducted in a low-speed water channel, as shown in Fig. 15. The channel made of acrylic glass has a cross-section of 20 mm×20 mm. A slender cylinder with a diameter (d) of 2 mm is installed at the fully developed section of the channel. As illustrated in the enlarged view of Fig. 15, the cylinder is arranged at the center of the channel and its axis is parallel to the optical axis of the LF camera, which allows the vortex shedding occurs in the lateral direction (x-y plane). The Reynolds number Re_d based on the cylinder diameter d is defined as

$$\mathrm{Re}_d = \bar{v}d/\upsilon \tag{10}$$

where $\bar{v}$ denotes the mean free-stream velocity in the channel and υ denotes the kinematic viscosity of the water. In this study, the range of the flux (Q) controlled by an electric valve is from 35 to 100 L/h, corresponding to the Re_d of 50 to 140. The measurement volume behind the cylinder is set with spans of $5d \times 6.5d \times 6d$ along the x, y, and z-directions.

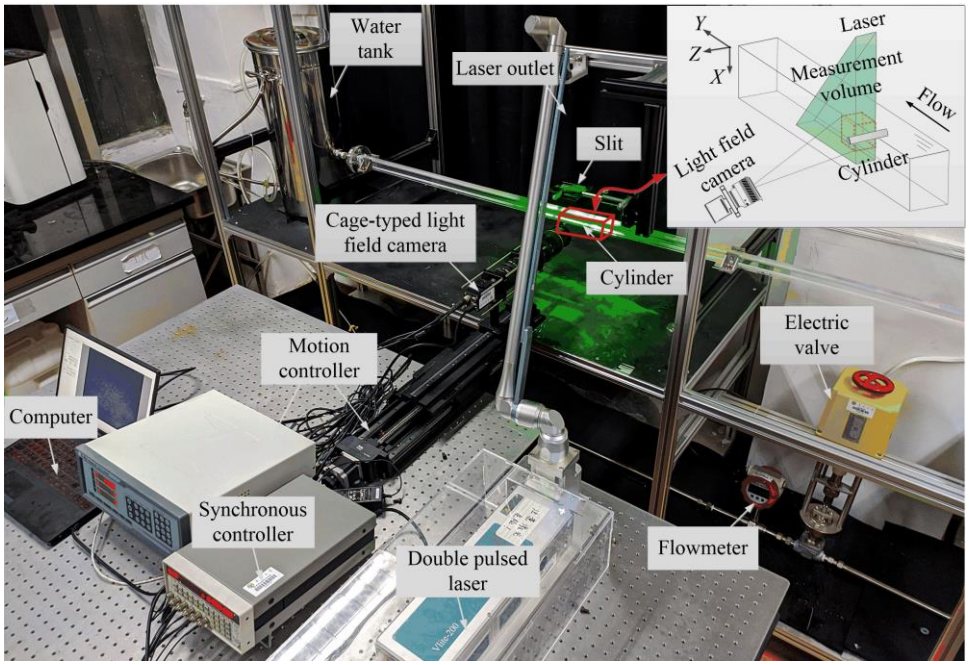

Fig. 15 Experimental setup of the cylinder wake flow measurement. The free-stream flow is along the y-direction. The cylinder axis is along the z-direction and is parallel to the optical axis of the LF camera. The laser illumination enters from the top of the channel.

Table 4: Optical settings of the LF camera and the conventional camera

Symbol	Parameter	Value	
		LF camera	Conventional camera
M	Magnification of the main lens	-1	-1
F_m	Focal length of the main lens	100 mm	100 mm
$F/\#$	f-number of the main lens	4	4
P_m	Aperture diameter of the main lens	25 mm	25 mm
f_m	Focal length of the microlens	0.8 mm	-
$f/\#$	f-number of the microlens	8	-
p_m	Microlens pitch	0.1 mm	-
n_x	Number of the microlens in the x-direction	131	-
n_y	Number of the microlens in the y-direction	99	-
p_x	Pixel size	5.5 μm	5.5μm
N_x	Camera resolution in the x-direction	2352	2352
N_y	Camera resolution in the y-direction	1768	1768

To yield the optimal seeding concentration of 0.6 ppm (Section 3.3), the polyamide particles with a density of 1.02 g/cm^3 and a diameter of 10 μm are carefully weighed and uniformly seeded

in the flow. A Nd:YAG dual pulse laser (Beamtech Vlite, 200 mJ, 532 nm, 15Hz) coupled with a beam expander and a knife-edge slit is used to illuminate the measurement volume. The particle motions are captured using an in-house LF camera with the optical settings listed in Table 4. A detailed description of the camera assembly can be found elsewhere in [33,60].

4.2 Calibration

To ensure that the center of the measurement volume can be located at z = -10 mm for accurate velocity measurement (Section 3.4), a simple calibration procedure is performed. A smart calibration board (with known dot marks) is stuck on the front wall of the channel, and its LF images are recorded with the translation of the LF camera via a high-precision motion controller (Zolix SC 300, resolution of 10 μm). As the dot diameter is the same as the microlens pitch, only a single microlens can be lighted by each dot when the calibration target is in focus (as shown in Fig. 16 (a)), otherwise additional microlens will also be lighted (as shown in Fig. 16 (b) and (c)). Based on this image feature, the focal plane of the LF camera can be determined. After that, the LF camera is further moved towards the channel with a distance (d_m) of

$$d_m = t_b + t_w/n_{ag} + \left(0.5d_{th} + 10\right)/n_w \tag{11}$$

where t_b and t_w denote the thickness of the calibration board and channel wall, respectively. d_{th} denotes the diameter of the channel, n_{ag} and n_w are the refractive index of acrylic glass and water, respectively. In this way, the center of the measurement volume is located at z = -10 mm and aligned with the central depth of the channel. Fig. 17 shows two successive LF images of the confined cylinder wake flow at Re_d = 140.

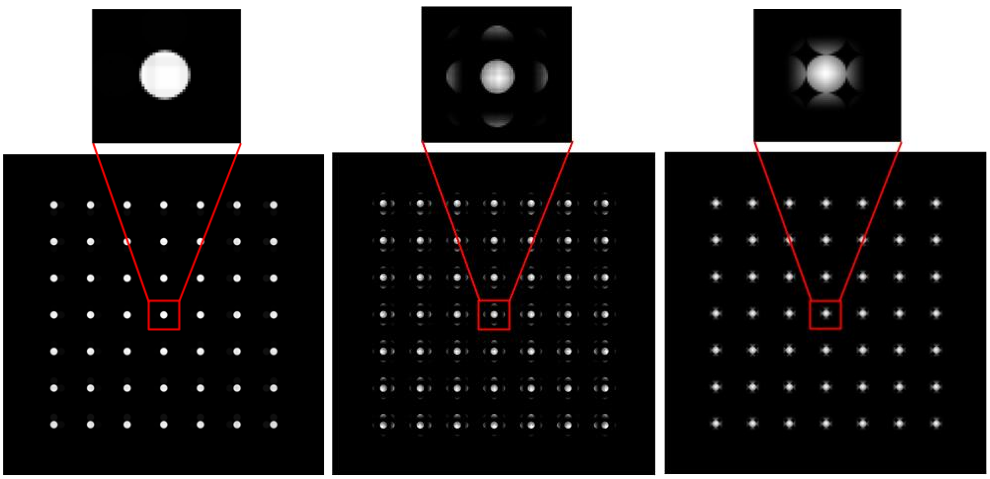

(a) In focus (b) At outer-focal side (c) At inner-focal side

Fig. 16 Different image features are demonstrated on the LF images when the calibration board is located at (a) Focal plane, (b) Outer-focal side with defocus distance of 1 mm, and (c) Inner-focal side with defocus distance of 1 mm.

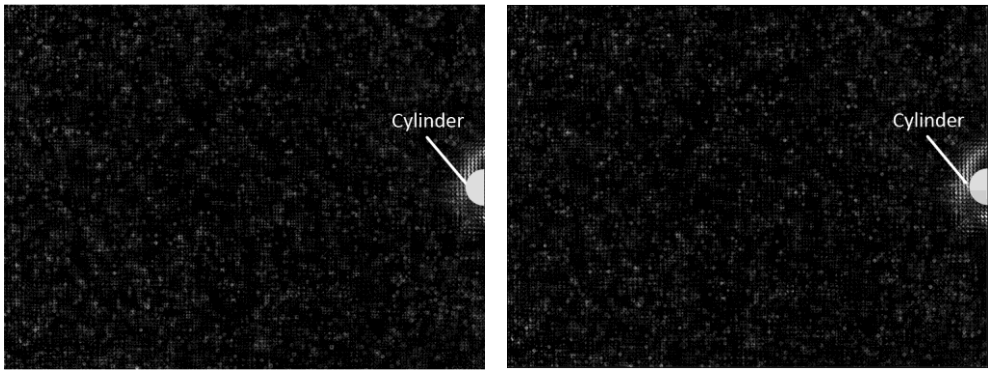

(a) LF image at time t_1 (b) LF image at time $t_1+\Delta t$

Fig. 17 Experimental LF images of cylinder wake flow captured at (a) time t_1 and (b) time $t_1+\Delta t$.

4.3 Generation of velocity fields

The 3D particle distributions are reconstructed by the PR-SART algorithm [33]. The measurement volume is discretized into 200×260×240 voxels with the size of 0.05 mm×0.05 mm×0.05 mm. 200 iterations are performed to ensure the convergence of the PR-SART algorithm. With the consideration of the imaging resolution of the used LF camera [37], the time interval between two frames is set as 1 to 3.3 ms for different free-stream velocities. A maximum particle displacement of 6 voxels between two successive recordings is yielded. To ensure a VDP of 95% in the cross-correlation calculation, the size of the interrogation window is selected as 32×32×32 voxels. The corresponding DIR is 18.8% and each window contains about 40 particles. The criterion in Table 1 can hence be satisfied. With an overlap of 0.75, 25×32×30 vectors with the spatial resolution of 1.6 mm×1.6 mm×1.6 mm are returned from the cross-correlation calculation. For the statistical measurements, a total of 150 instantaneous velocity fields are reconstructed and the time-averaged (mean) velocity field is acquired.

In addition to the LF-PIV, the planar PIV measurements are also conducted in a similar configuration. As a widespread technique in fluid dynamics studies, the planar PIV has been developed for several decades and become mature nowadays. Therefore, the measurement result by the planar PIV can provide a baseline for the quantitative evaluation of the LF-PIV performance. In the planar PIV measurements, the conventional camera is focused on the central depth of the channel via a sharpness evaluation procedure [33], and a thin laser sheet aligning with the camera's focal plane is created by the contracted slit. The optical settings of the conventional camera are listed in Table 4, which generates the same field of view of $5d$ ×$6.5d$ with the LF camera. With a maximum particle image displacement of 55 pixels, the initial and final interrogation windows of the multi-pass cross-correlation algorithm [29] are set as 256×256 pixels and 32×32 pixels, respectively, consequently returning 109×146 velocity vectors with the spatial resolution of 0.176 mm×0.176 mm. A total of 300 image pairs are recorded and processed to acquire the mean velocity field at each flow case.

5. Results and discussions

The mean velocity field measured by the LF-PIV at Q = 100 L/h (Re_d = 140) is illustrated in Fig. 18. The directions of the cylinder axis and the free-stream velocity are along the z-axis and y-axis, respectively. The distance from the cylinder axis is normalized by the cylinder diameter (d).

There are five slices at different depths (z/d = -2.7, -1.35, 0, 1.35, 2.7) displayed in this figure, and the contour shows the magnitude of the streamwise velocity component (v). It can be observed that the reverse flow in the cylinder wake is shown at different depths but with different lengths. It reaches y = 4.5 d at the central depth and gradually shrinks to y = 2.2 d at the front and rear sides of the channel. This result is different from the previous studies at the similar Re_d [10], which indicate that the velocity distributions at different depths are almost the same and the flow reversal is shorter than 3d. The probable reason is that the cylinders in their studies are positioned in the spacious channels, and the velocity used in the definition of the Reynold number is the bulk velocity, which is nearly constant in the channel. In contrast, the free-stream velocity shows a parabolic profile distribution in this study due to the constraint of the channel wall [33]. With the decrease of the free-stream velocity from the center to the wall, the length of the reverse flow shrinks accordingly. Besides, as the confined channel restricts the development of the shear layer attached to the cylinder, the reverse flow at the central depth extends further in this study.

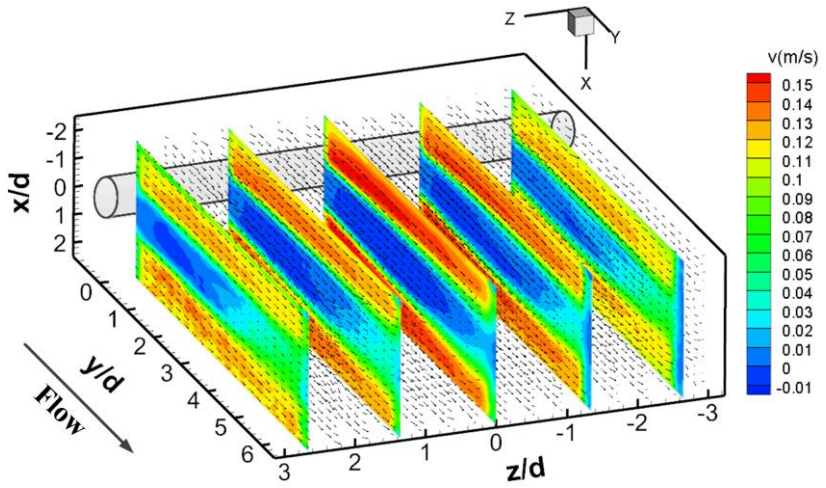

Fig. 18 3D mean velocity field of the cylinder wake flow at Q = 100 L/h (Re_d = 140). Five slices at different depths (z/d = -2.7, -1.35, 0, 1.35, 2.7) are contoured by the streamwise velocity magnitude (v). The skips of the velocity vectors are set as 3 in the x, y, and z directions for a clear illustration.

The mean velocity distribution on the central depth of the channel is further extracted from the 3D data for comparison with the planar-PIV result, as illustrated in Fig. 19. The figures in the top and bottom rows show the streamwise and transverse velocity components (v and u), respectively. Qualitatively, the flow structure measured by the planar-PIV and LF-PIV is consistent with each other. The flow acceleration is demonstrated at the top and bottom of the cylinder and the reverse flow is formed behind the cylinder. The reverse flow almost disappeared downstream (y = 6.5d, x/d = 0) but a significant velocity deficit relative to the free stream remains. Compared with the space-unconstraint case where half of the free-stream velocity can be recovered at about y = 3.75d [61], the recovery of the free-stream velocity in a confined channel requires a longer distance. Furthermore, a nearly symmetrical structure of u component distribution is shown around the cylinder. The transverse velocity components are generated when the flow moves over the cylinder.

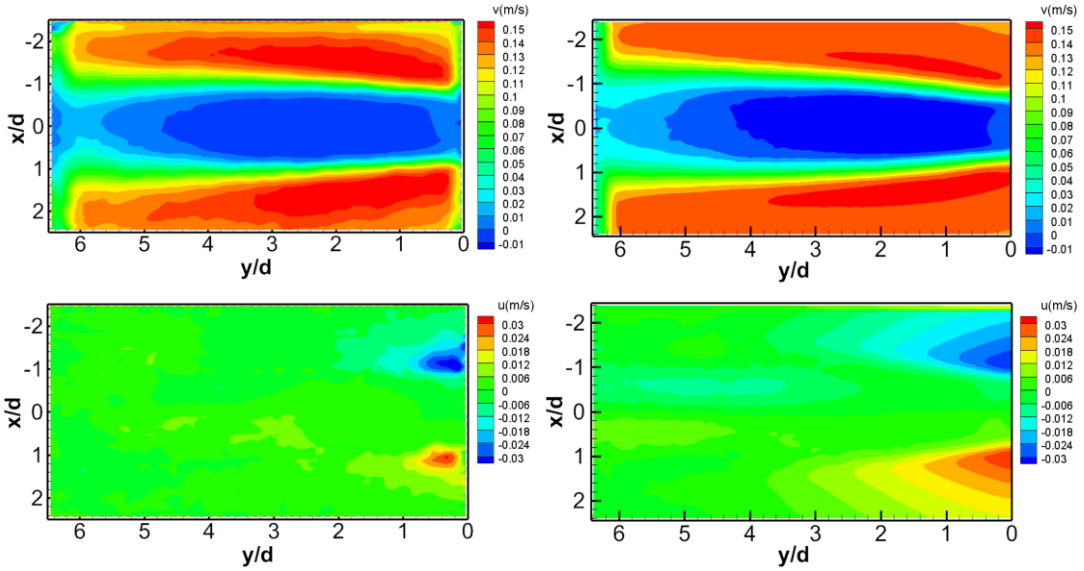

(a) LF-PIV (b) Planar PIV

Fig. 19 Mean velocity distribution on the central depth of the channel (z = 0) at Q = 100 L/h (Re_d = 140). (a) 2D slice extracted from the 3D LF-PIV data and (b) 2D planar-PIV result. The contours in the top and bottom row figures show the streamwise and transverse components (v and u), respectively.

Although a common flow structure can be seen from the results of these two methods, there are still some differences. A noticeable finding is that the velocity gradient is visible in the planar PIV result (especially for u component) but seems not perceivable in the LF-PIV result. This can be largely attributed to the disparity in the achievable spatial resolution of these two methods. As described in Section 4.3, the spatial resolution of the velocity field measured by the LF-PIV is 9 times lower than the planar-PIV. Therefore, the flow structures resolved by the LF-PIV are coarser.

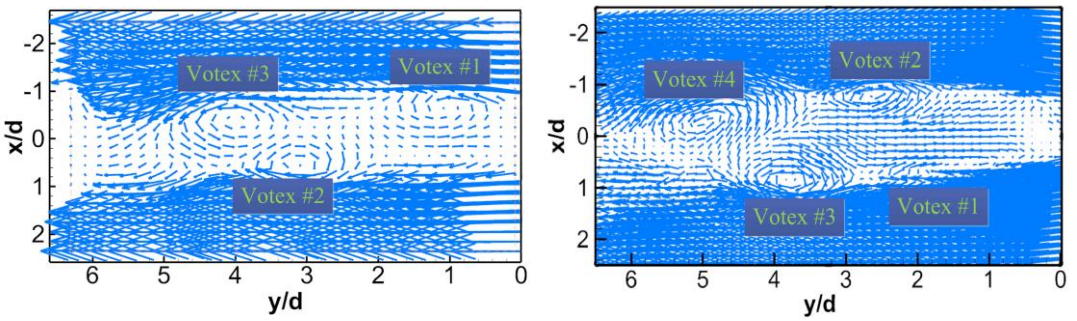

(a) LF-PIV (b) Planar PIV

Fig. 20 Instantaneous velocity field on the central depth of the channel at Q = 100 L/h (Re_d = 140) measured by (a) LF-PIV and (b) planar-PIV.

This difference can also be found in Fig. 20, which shows an example of the instantaneous velocity field measured by these two methods. From Fig. 20, two rows of the staggered vortices shedding from the cylinder are presented. The vortices on the lower and upper sides rotate along with the clockwise and anti-clockwise directions, respectively. These flow characteristics indicate that the Kármán vortex street is formed behind the cylinder at the Re_d of 140. The formed vortices oscillate in the traverse direction (x), although the amplitude is insignificant. Based on the Kutta-

Joukowski theorem [62], the oscillation is mainly caused by the lift on the cylinder, which is generated by the velocity circulation. The direction of the lift is perpendicular to the streamflow and periodically changed with the rotation direction of the vortex. Since the vortices at two rows are alternatively formed and their rotation directions are opposite, thus the reacting force of the lift causes the oscillation of the vortices. The comparison of the measurement results in Fig. 20 indicates that the LF-PIV can outline the vortices, despite the measurement resolution should be further improved for resolving finer flow structures.

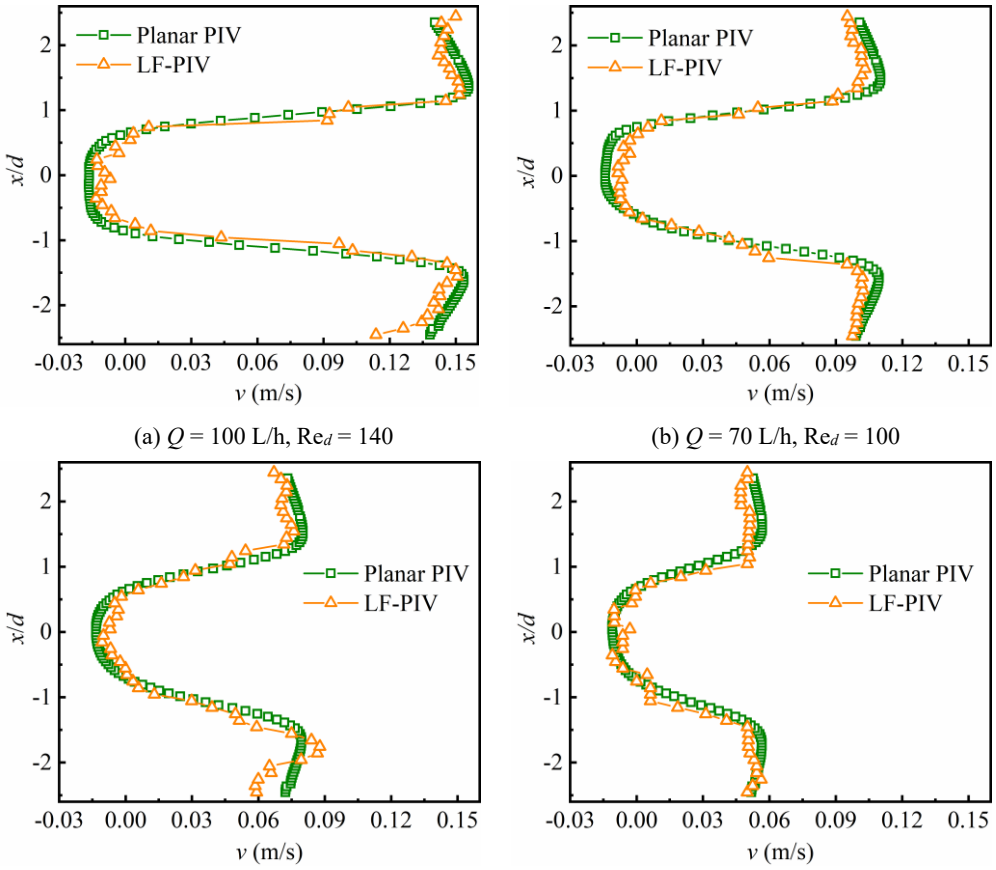

(a) Q = 100 L/h, Re_d = 140 (b) Q = 70 L/h, Re_d = 100

(c) Q = 50 L/h, Re_d = 70 (d) Q = 35 L/h, Re_d = 50

Fig. 21 Mean streamwise velocity (v) distribution along the transverse direction (x) at y/d = 2 and z/d = 0. The flux and the corresponding Reynolds number is (a) Q = 100 L/h, Re_d = 140, (b) Q = 70 L/h, Re_d = 100, (c) Q = 50 L/h, Re_d = 70 and (d) Q = 35 L/h, Re_d = 50.

Further quantitative comparison between the measurement results of the planar PIV and the LF-PIV at different Re_d is carried out by extracting the mean streamwise velocity component (v) at $y = 2d$ and $z = 0$. The results are depicted in Fig. 21. At first glance, the LF-PIV data generally match the main trends of the planar-PIV data at different Re_d. The streamwise velocity sharply increased from the wake flow region (x = 0) to the acceleration region ($x = \pm 1.5d$) and then gradually decreased due to the viscosity of the fluid. With the decrease of Re_d from 140 to 50, the velocity in the acceleration region gradually reduces, while the velocity in the wake flow varies a little. These common features indicate that both the planar-PIV and LF-PIV appear to correctly resolve the flow characteristics behind the cylinder. However, the profiles of the LF-PIV have some outliers and are not smooth as the planar PIV. In addition to the lower spatial resolution of the LF-PIV, another likely

reason is that the number of the instantaneous velocity fields reconstructed by the LF-PIV is only half of the planar PIV. The less sampling in the LF-PIV is mainly due to the large computational cost in the 3D particle reconstruction, which typically requires 40 minutes for reconstructing each pair of the LF images. In contrast, the planar PIV needs no volumetric reconstruction and only costs 2 minutes on the cross-correlation calculation.

Table 5: Error of the streamwise velocity (v) measured by the LF-PIV at different Re_d

Q (L/h)	Re_d	Δt (s)	Mean error		Max error	
			(m/s)	(voxel)	(m/s)	(voxel)
100	140	1×10^{-3}	0.0092	0.184	0.0357	0.714
70	100	1.4×10^{-3}	0.0066	0.185	0.0256	0.717
50	70	2×10^{-3}	0.0068	0.272	0.0198	0.792
30	50	3.3×10^{-3}	0.0051	0.337	0.0123	0.812

Considering the measurement result of the planar PIV as the ground truth, the measurement error of the streamwise velocity by the LF-PIV is calculated and shown in Table 5. For ease of comparison with the previous work, the unit of the velocity error is transformed from meters per second (m/s) to the displacement in voxels, as

$$e_{ms} = \left(e_v \times vox_s\right)/\Delta t \tag{12}$$

where e_{ms} and e_v denote the velocity errors in m/s and voxels, respectively. vox_s denotes the voxel size and Δt denotes the time interval between two successive frames. For example, the velocity error of 0.0092 m/s corresponds to a 0.184 voxel displacement for the time interval of 1 ms. From Table 5, the maximum velocity error achieved corresponds to 0.812 voxel displacement, and the mean error is less than 0.337 voxel. It is demonstrated that the measurement accuracy has been improved compared with the results in [10], which reported that mean and max measurement errors are 0.5 voxels and 1 voxel, respectively. Therefore, the feasibility of the proposed criteria for the selection of cross-correlation parameters in the LF-PIV is verified.

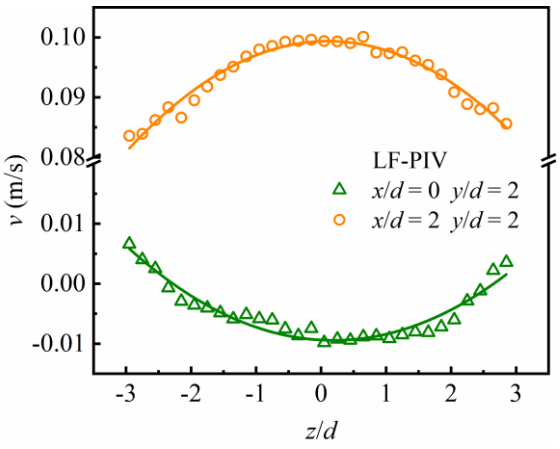

Fig. 22 Streamwise velocity (v) distributions along the depth direction (z) measured by the LF-PIV. The polynomial curve fittings are performed on the measurement results at $x/d = 2$, $y/d = 2$ and $x/d = 0$, $y/d = 2$.

Although with no comparison data, the velocity distribution along the depth direction (z) is

also extracted from the 3D LF-PIV data for qualitative analysis. Similar trends are observed at Re_d = 50 to 140, as an example, the result is shown for Re_d = 100. Fig. 22 shows the v component distribution at the wake flow region (x/d = 0, y/d =2) and the acceleration region (x/d = 2, y/d =2). The polynomial curve fittings are performed on the measurement result. It can be seen that v decreases from the center of the channel to the wall at the acceleration region, which can be interpreted by the effect of the fluid viscosity. The magnitude of v at the wake flow region is much smaller than that in the acceleration region, and the flow direction gradually changed from the center to the wall. This result is following the shrinkage of the reverse flow in Fig. 18. The effect of the constrained channel hereby appears.

The result in Fig. 22 further validates that the single-camera-based LF-PIV with the selected parameters can measure the 3D velocity field. With this attractive feature, the LF-PIV has great potential to be an alternative to the multi-camera-based volumetric velocimetry techniques in space-constrained applications. Further development of the high-speed LF camera and the spectral LF camera may allow access to the temporal information of the unsteady flows and the scalar field measurement [63–65].

6. Conclusion

This work presents a systematic approach to selecting optimum cross-correlation parameters of light field PIV for accurate 3D flow velocity measurement. The concluding criteria can be summarized as follows:

- The ratio of the maximum particle displacement to the interrogation volume size should be limited to 5.1%, 20.9% and 28.1% under the case that the interrogation window contains 5, 15, and 25 particles. A relatively small interrogation volume that can satisfy this criterion is preferred for velocity measurement with high spatial resolution.
- A large seeding concentration of the tracer particles improves the velocity measurement accuracy in the in-plane dimension but decreases the accuracy in the out-of-plane dimension. The optimal seeding concentration is determined as 0.6 ppm by considering the trade-off between the in-plane and out-of-plane measurement accuracy.
- The use of small tracer particles helps to reduce the velocity measurement errors caused by the particle elongation effects in the reconstruction.
- The center of the measurement volume should be located at the inner-focal side of the LF camera with a defocus distance of 10 mm for the lowest RMSE of the measured velocity.

The feasibility of the proposed criteria is verified by the experimental measurements of the cylinder wake flow in a confined channel. The result shows that the Kármán vortex street is formed behind the cylinder at the Reynolds number of 50 to 140. The constraint channel leads to the shrinkage of the wake flow from the channel center to the wall. Through the comparison with the measurement result of the planar PIV, the accuracy of the LF-PIV in the cylinder wake flow measurement is quantitatively evaluated. The result shows improved accuracy in the velocity measurement.

Author Declaration

Conflict of interest

The authors declare that they have no known competing financial interests or personal

relationships that could have appeared to influence the work reported in this paper.

Acknowledgements

The authors wish to express their gratitude to the National Natural Science Foundation of China (No. 51976038) and the Natural Science Foundation of Jiangsu Province, China (No. BK20190366) for supporting this research. The first author would also like to acknowledge the scholarship from China Scholarship Council (Grant No. 202006090162).

References

[1] Poullikkas A. An overview of current and future sustainable gas turbine technologies. Renew Sustain Energy Rev 2005;9:409–43. https://doi.org/10.1016/j.rser.2004.05.009.

[2] Amoo LM. On the design and structural analysis of jet engine fan blade structures. Prog Aerosp Sci 2013;60:1–11. https://doi.org/10.1016/j.paerosci.2012.08.002.

[3] He C, Wang P, Liu Y, Gan L. Flow enhancement of tomographic particle image velocimetry measurements using sequential data assimilation. Phys Fluids 2022;34. https://doi.org/10.1063/5.0082460.

[4] Kempaiah KU, Scarano F, Elsinga GE, Van Oudheusden BW, Bermel L. 3-Dimensional Particle Image Velocimetry Based Evaluation of Turbulent Skin-Friction Reduction By Spanwise Wall Oscillation. Phys Fluids 2020;32. https://doi.org/10.1063/5.0015359.

[5] Gim Y, Jang DK, Sohn DK, Kim H, Ko HS. Three-dimensional particle tracking velocimetry using shallow neural network for real-time analysis. Exp Fluids 2020;61:1–8. https://doi.org/10.1007/s00348-019-2861-8.

[6] Zhu Y, Yuan H, Lee C. Ultrafast tomographic particle image velocimetry investigation on hypersonic boundary layers. Phys Fluids 2020;32. https://doi.org/10.1063/5.0014168.

[7] Discetti S, Coletti F. Volumetric velocimetry for fluid flows. Meas Sci Technol 2018;29:042001. https://doi.org/10.1088/1361-6501/aaa571.

[8] Soria J. Three-component three-dimensional (3C-3D) fluid flow velocimetry for flow turbulence investigations. Proc. 21st Australas. Fluid Mech. Conf. AFMC 2018, 2018.

[9] Zhao Z, Ding J, Shi S, Kaufmann R, Ganapathisubramani B. Volumetric flow characterisation of a rectangular orifice impinging synthetic jet with single-camera light-field PIV. Exp Therm Fluid Sci 2021;123:110327. https://doi.org/10.1016/j.expthermflusci.2020.110327.

[10] Fahringer TW, Lynch KP, Thurow BS. Volumetric particle image velocimetry with a single plenoptic camera. Meas Sci Technol 2015;26. https://doi.org/10.1088/0957-0233/26/11/115201.

[11] Shi S, Ding J, Atkinson C, Soria J, New TH. A detailed comparison of single-camera light-field PIV and tomographic PIV. Exp Fluids 2018;59:1–13. https://doi.org/10.1007/s00348-018-2500-9.

[12] Ng R. Digital light field photography. Stanford Univ 2006:1–203.

[13] Elsinga GE, Scarano F, Wieneke B, Van Oudheusden BW. Tomographic particle image velocimetry. Exp Fluids 2006;41:933–47. https://doi.org/10.1007/s00348-006-0212-z.

[14] Westerweel J. Fundamentals of digital particle image velocimetry. Meas Sci Technol 1997;8:1379–92. https://doi.org/10.1088/0957-0233/8/12/002.

[15] Scharnowski S, Sciacchitano A, Kahler CJ. On the universality of Keane & Adrian's valid detection probability in PIV. Meas Sci Technol 2019;30:035203. https://doi.org/10.1088/1361-6501/aafe9d.

[16] Scharnowski S, Kähler CJ. Particle image velocimetry - Classical operating rules from today's perspective. Opt Lasers Eng 2020;135:106185. https://doi.org/10.1016/j.optlaseng.2020.106185.

[17] Lavoie P, Avallone G, De Gregorio F, Romano GP, Antonia RA. Spatial resolution of PIV for the measurement of turbulence. Exp Fluids 2007;43:39–51. https://doi.org/10.1007/s00348-007-0319-x.

[18] Keane RD, Adrian RJ. Optimization of particle image velocimeters: Optical Methods in Flow and Particle Diagnostics. doi:10.1117/12.35018. Meas Sci Technol 1990;1:139–59.

[19] Sciacchitano A. Uncertainty quantification in particle image velocimetry. Meas Sci Technol 2019;30. https://doi.org/10.1088/1361-6501/ab1db8.

[20] Keane RD, Adrian RJ. Optimization of particle image velocimeters: II. Multiple pulsed systems. Meas Sci Technol 1991;2:963–74. https://doi.org/10.1088/0957-0233/2/10/013.

[21] Keane RD, Adrian RJ. Theory of cross-correlation analysis of PIV images. Appl Sci Res 1992;49:191–215. https://doi.org/10.1007/BF00384623.

[22] Christensen KT. The influence of peak-locking errors on turbulence statistics computed from PIV ensembles. Exp Fluids 2004;36:484–97. https://doi.org/10.1007/s00348-003-0754-2.

[23] Chen J, Katz J. Elimination of peak-locking error in PIV analysis using the correlation mapping method. Meas Sci Technol 2005;16:1605–18. https://doi.org/10.1088/0957-0233/16/8/010.

[24] Westerweel J, Dabiri D, Gharib M. The effect of a discrete window offset on the accuracy of cross-correlation analysis of digital PIV recordings. Exp Fluids 1997;23:20–8. https://doi.org/10.1007/s003480050082.

[25] Adrian RJ. Dynamic ranges of velocity and spatial resolution of particle image velocimetry. Meas Sci Technol 1997;8:1393–8. https://doi.org/10.1088/0957-0233/8/12/003.

[26] Raffel Markus，Christian E. Willert,Fulvio Scarano,Christian J. Kähler,Steve T. Wereley JK. Particle Image Velocimetry：A Practical Guide. 3rd ed. Springer; 2018. https://doi.org/https://doi.org/10.1007/978-3-319-68852-7.

[27] Adrian RJ. Twenty years of particle image velocimetry. Exp. Fluids, vol. 39, 2005, p. 159–69. https://doi.org/10.1007/s00348-005-0991-7.

[28] Lindken R, Merzkirch W. A novel PIV technique for measurements in multiphase flows and its application to two-phase bubbly flows. Exp Fluids 2002;33:814–25. https://doi.org/10.1007/s00348-002-0500-1.

[29] Scarano F, Riethmuller ML. Advances in iterative multigrid PIV image processing. Exp Fluids 2000;29. https://doi.org/10.1007/s003480070007.

[30] Campbell M, Cosgrove JA, Created CA, Jack S, Rockliff D. Review of LDA and PIV applied to the measurement of sound and acoustic streaming. Opt Laser Technol 2000;32:629–39. https://doi.org/10.1016/S0030-3992(00)00091-8.

[31] Shi S, Wang J, Ding J, Zhao Z, New TH. Parametric study on light field volumetric particle image velocimetry. Flow Meas Instrum 2016;49:70–88. https://doi.org/10.1016/j.flowmeasinst.2016.05.006.

[32] Cao L, Zhang B, Li J, Song X, Tang Z, Xu C. Characteristics of tomographic reconstruction of light-field Tomo-PIV. Opt Commun 2019;442:132–47. https://doi.org/10.1016/j.optcom.2019.03.026.

[33] Zhu X, Wu Z, Li J, Zhang B, Xu C. A pre-recognition SART algorithm for the volumetric reconstruction of the light field PIV. Opt Lasers Eng 2021;143:106625. https://doi.org/10.1016/j.optlaseng.2021.106625.

[34] Mei D, Ding J, Shi S, New TH, Soria J. High resolution volumetric dual-camera light-field PIV. Exp Fluids 2019;60:132. https://doi.org/10.1007/s00348-019-2781-7.

[35] Cao L, Zhang B, Hossain MM, Li J, Xu C. Tomographic reconstruction of light field PIV based on a backward ray-tracing technique. Meas Sci Technol 2021;32:044007. https://doi.org/10.1088/1361-

6501/abd281.

[36] Scharnowski S, Grayson K, de Silva CM, Hutchins N, Marusic I, Kähler CJ. Generalization of the PIV loss-of-correlation formula introduced by Keane and Adrian. Exp Fluids 2017;58:1–12. https://doi.org/10.1007/s00348-017-2431-x.

[37] Zhu X, Zhang B, Li J, Xu C. Volumetric resolution of light field imaging and its effect on the reconstruction of light field PIV. Opt Commun 2020;462:125263. https://doi.org/10.1016/j.optcom.2020.125263.

[38] Fahringer TW, Thurow BS. Plenoptic particle image velocimetry with multiple plenoptic cameras. Meas Sci Technol 2018;29. https://doi.org/10.1088/1361-6501/aabe1d.

[39] Deem EA, Zhang Y, Cattafesta LN, Fahringer TW, Thurow BS. On the resolution of plenoptic PIV. Meas Sci Technol 2016;27:084003. https://doi.org/10.1088/0957-0233/27/8/084003.

[40] Sun J, Xu C, Zhang B, Hossain MM, Wang S, Qi H, et al. Three-dimensional temperature field measurement of flame using a single light field camera. Opt Express 2016;24:1118. https://doi.org/10.1364/oe.24.001118.

[41] Zhu S, Lai A, Eaton K, Jin P, Gao L. On the fundamental comparison between unfocused and focused light field cameras. Appl Opt 2018;57:A1. https://doi.org/10.1364/ao.57.0000a1.

[42] Song X, Gu M, Cao L, Tang Z, Xu C. A microparticle image velocimetry based on light field imaging. IEEE Sens J 2019;19:9806–17. https://doi.org/10.1109/JSEN.2019.2927414.

[43] Tan ZP, Thurow BS. Perspective on the development and application of light-field cameras in flow diagnostics. Meas Sci Technol 2021;32:101001. https://doi.org/10.1088/1361-6501/ac026e.

[44] Wieneke B. PIV uncertainty quantification from correlation statistics. Meas Sci Technol 2015;26:074002. https://doi.org/10.1088/0957-0233/26/7/074002.

[45] Zhou P, Cai W, Yu Y, Zhang Y, Zhou G. A two-step calibration method of lenslet-based light field cameras. Opt Lasers Eng 2019;115:190–6. https://doi.org/10.1016/j.optlaseng.2018.11.024.

[46] Zhu X, Hossain discussion M, Li J, Zhang B, Xu C. Weight Coefficient Calculation through Equivalent Ray Tracing Method for Light Field Particle Image Velocimetry. Measurement 2022;193:110982. https://doi.org/10.1016/j.measurement.2022.110982.

[47] Shi S, Ding J, New TH, Liu Y, Zhang H. Volumetric calibration enhancements for single-camera light-field PIV. Exp Fluids 2019;60:21. https://doi.org/10.1007/s00348-018-2670-5.

[48] Scarano F. Tomographic PIV: Principles and practice. Meas Sci Technol 2013;24:012001. https://doi.org/10.1088/0957-0233/24/1/012001.

[49] Buffoni M, Camarri S, Iollo A, Salvetti M V. Low-dimensional modelling of a confined three-dimensional wake flow. J Fluid Mech 2006;569:141–50. https://doi.org/10.1017/S0022112006002989.

[50] Roy A, Bandyopadhyay G. Numerical investigation of confined flow past a square cylinder placed in a channel. J Inst Eng Aerosp Eng J 2004;85:60–3.

[51] Sahin M, Owens RG. A numerical investigation of wall effects up to high blockage ratios on two-dimensional flow past a confined circular cylinder. Phys Fluids 2004;16:1305–20. https://doi.org/10.1063/1.1668285.

[52] Schanz D, Gesemann S, Schröder A. Shake-The-Box: Lagrangian particle tracking at high particle image densities. Exp Fluids 2016;57:57:70. https://doi.org/10.1007/s00348-016-2157-1.

[53] Beresh SJ. Time-resolved particle image velocimetry. Meas Sci Technol 2021;32:102003. https://doi.org/10.1088/1361-6501/ac08c5.

[54] Schröder A, Geisler R, Staack K, Elsinga GE, Scarano F, Wieneke B, et al. Eulerian and Lagrangian views of a turbulent boundary layer flow using time-resolved tomographic PIV. Exp. Fluids, vol. 50,

2011, p. 1071–91. https://doi.org/10.1007/s00348-010-1014-x.

[55] Tan ZP, Johnson K, Clifford C, Thurow BS. Development of a modular, high-speed plenoptic-camera for 3D flow-measurement. Opt Express 2019;27:13400. https://doi.org/10.1364/oe.27.013400.

[56] Zhang HQ, Fey U, Noack BR, König M, Eckelmann H. On the transition of the cylinder wake. Phys Fluids 1995;7:779–94. https://doi.org/10.1063/1.868601.

[57] Sciacchitano A, Wieneke B. PIV uncertainty propagation. Meas Sci Technol 2016;27:084006. https://doi.org/10.1088/0957-0233/27/8/084006.

[58] Shi S, Ding J, New TH, Soria J. Light-field camera-based 3D volumetric particle image velocimetry with dense ray tracing reconstruction technique. Exp Fluids 2017;58:78. https://doi.org/10.1007/s00348-017-2365-3.

[59] Hattori Y, LLewellyn Smith SG. Axisymmetric acoustic scattering by vortices. J Fluid Mech 2002:275–94. https://doi.org/10.1017/S002211200200246X.

[60] Liu Y, Zhu M, Wang T, Lei G, Hossain MM, Zhang B, et al. Spatial resolution of light field sectioning pyrometry for flame temperature measurement. Opt Lasers Eng 2021;140:106545. https://doi.org/10.1016/j.optlaseng.2021.106545.

[61] Elsinga GE, Oudheusden BW Van, Scarano F. Experimental assessment of tomographic-PIV accuracy Experimental assessment of Tomographic-PIV accuracy. 13th Int. Symp. Appl. Laser Tech. to Fluid Mech. (Lisbon, Port., 2014.

[62] Liu LQ, Zhu JY, Wu JZ. Lift and drag in two-dimensional steady viscous and compressible flow. J Fluid Mech 2015;784:304–41. https://doi.org/10.1017/jfm.2015.584.

[63] Tan ZP, Alarcon R, Allen J, Thurow BS, Moss A. Development of a high-speed plenoptic imaging system and its application to marine biology PIV. Meas Sci Technol 2020;31:054005. https://doi.org/10.1088/1361-6501/ab553c.

[64] Gururaj A, Moaven M, Tan ZP, Thurow B, Raghav V. Rotating three-dimensional velocimetry. Exp Fluids 2021;62:1–20. https://doi.org/10.1007/s00348-021-03241-4.

[65] Meng L, Sun T, Kosoglow R, Berkner K. Evaluation of multispectral plenoptic camera. Digit Photogr IX 2013;8660:86600D. https://doi.org/10.1117/12.2006293.

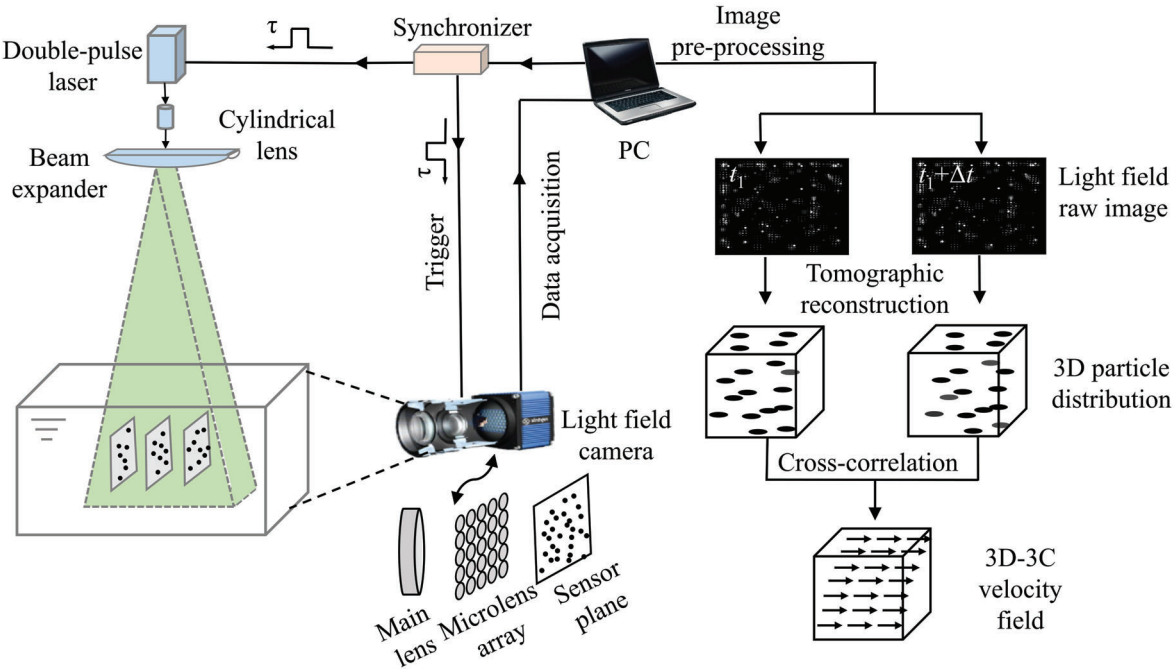

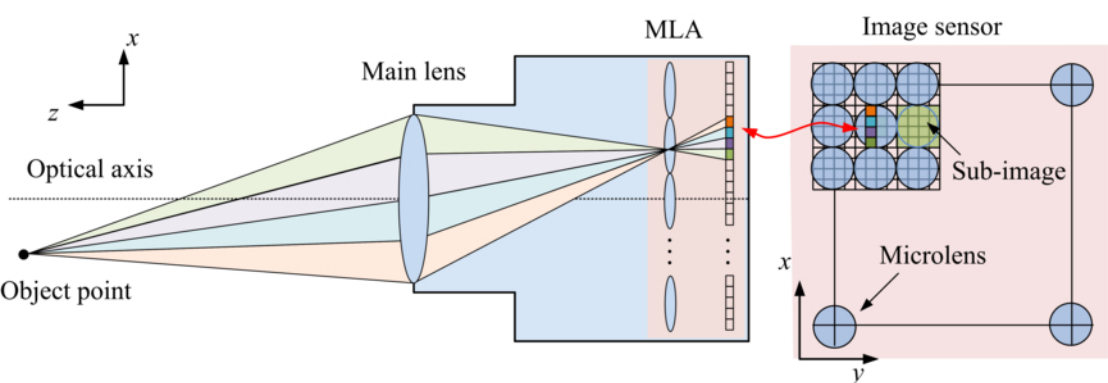
x
z
Main lens
MLA
Image sensor
Optical axis
Sub-image
Microlens
Object point
x
y

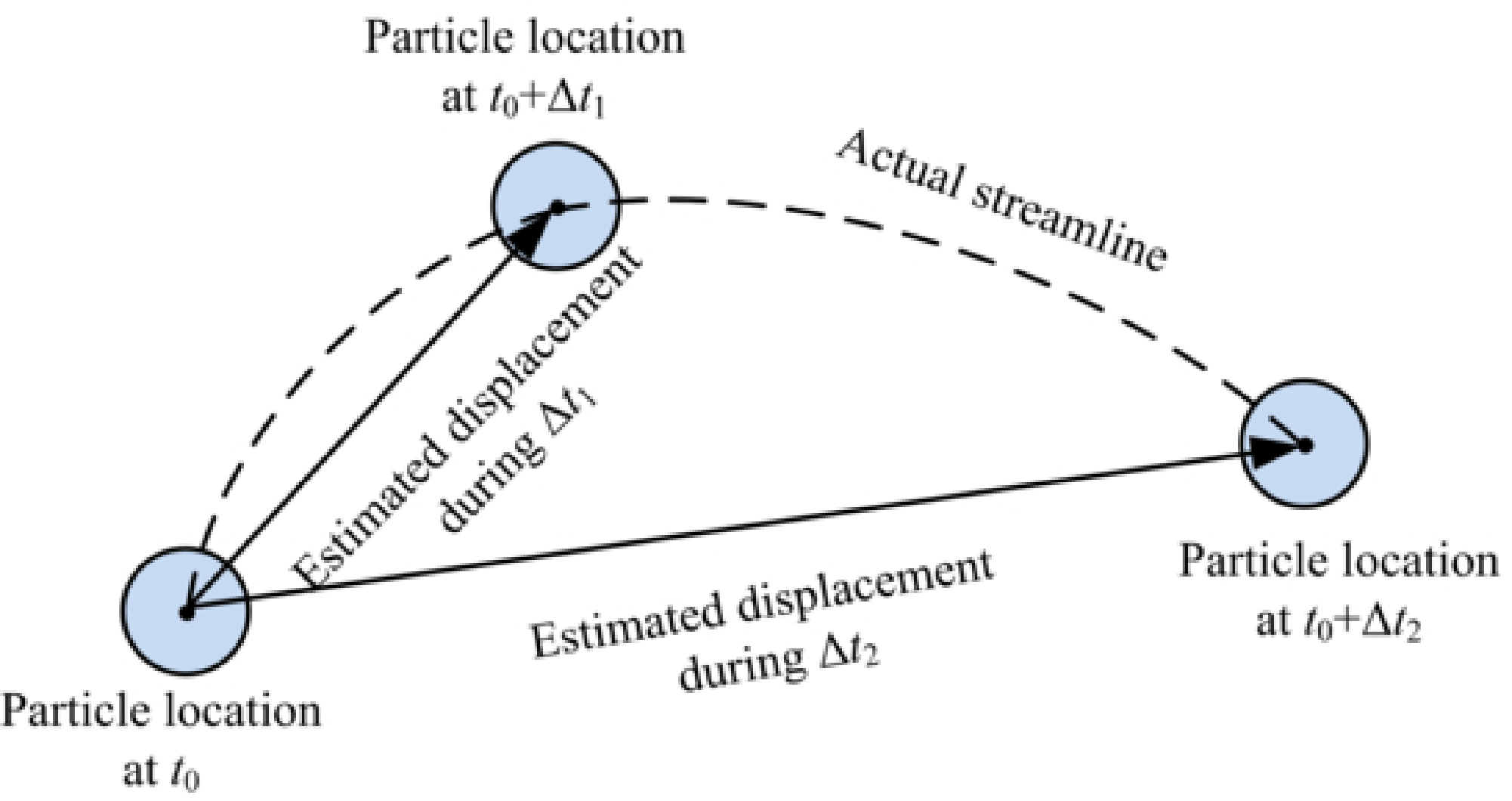
Particle location
at $t_0+\Delta t_1$
Actual streamline
Estimated displacement
during Δt_1
Estimated displacement
during Δt_2
Particle location
at $t_0+\Delta t_2$
Particle location
at t_0

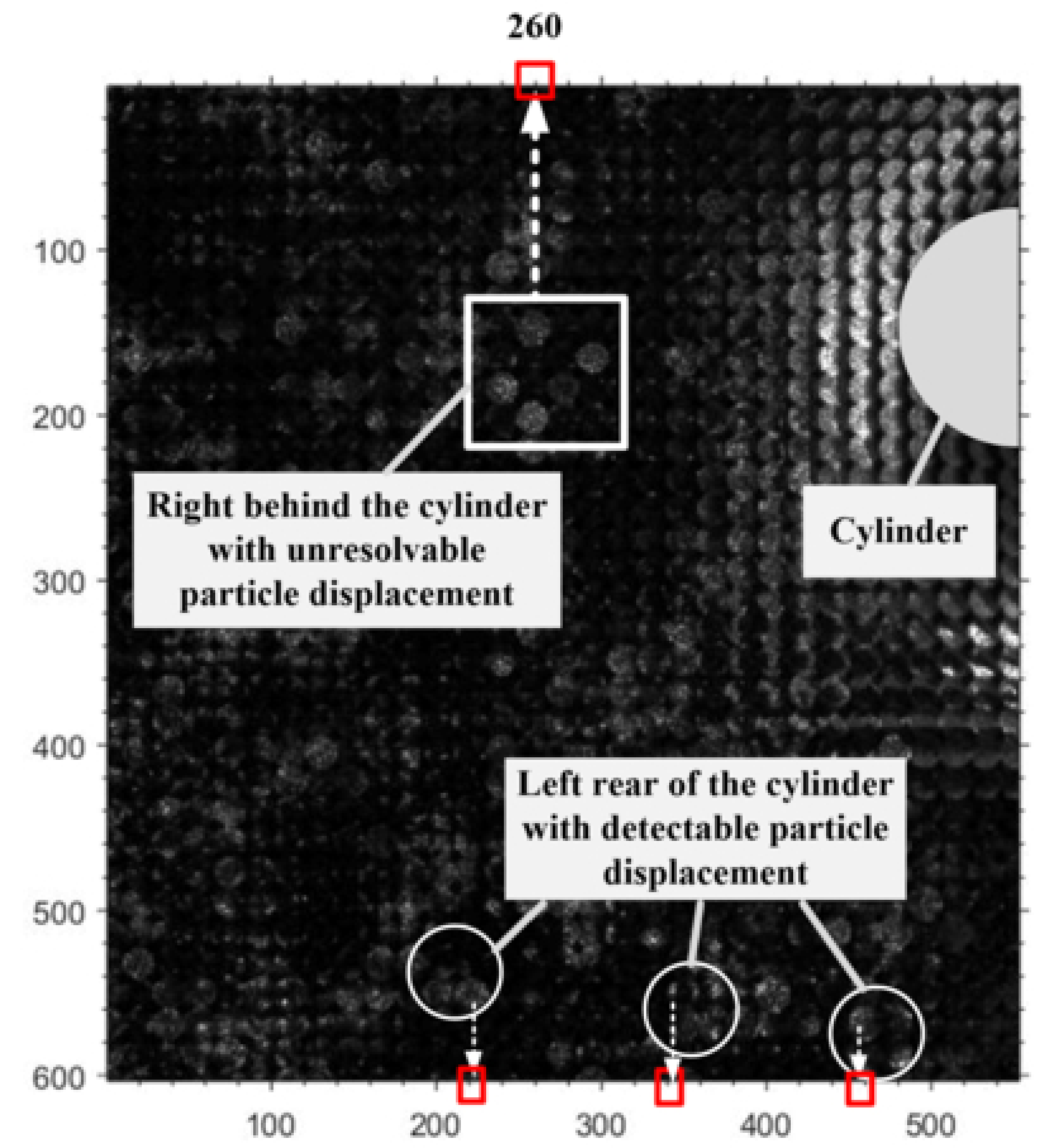
260
100
200
300
400
500
600
100
200
300
400
500
Right behind the cylinder with unresolvable particle displacement
Cylinder
Left rear of the cylinder with detectable particle displacement

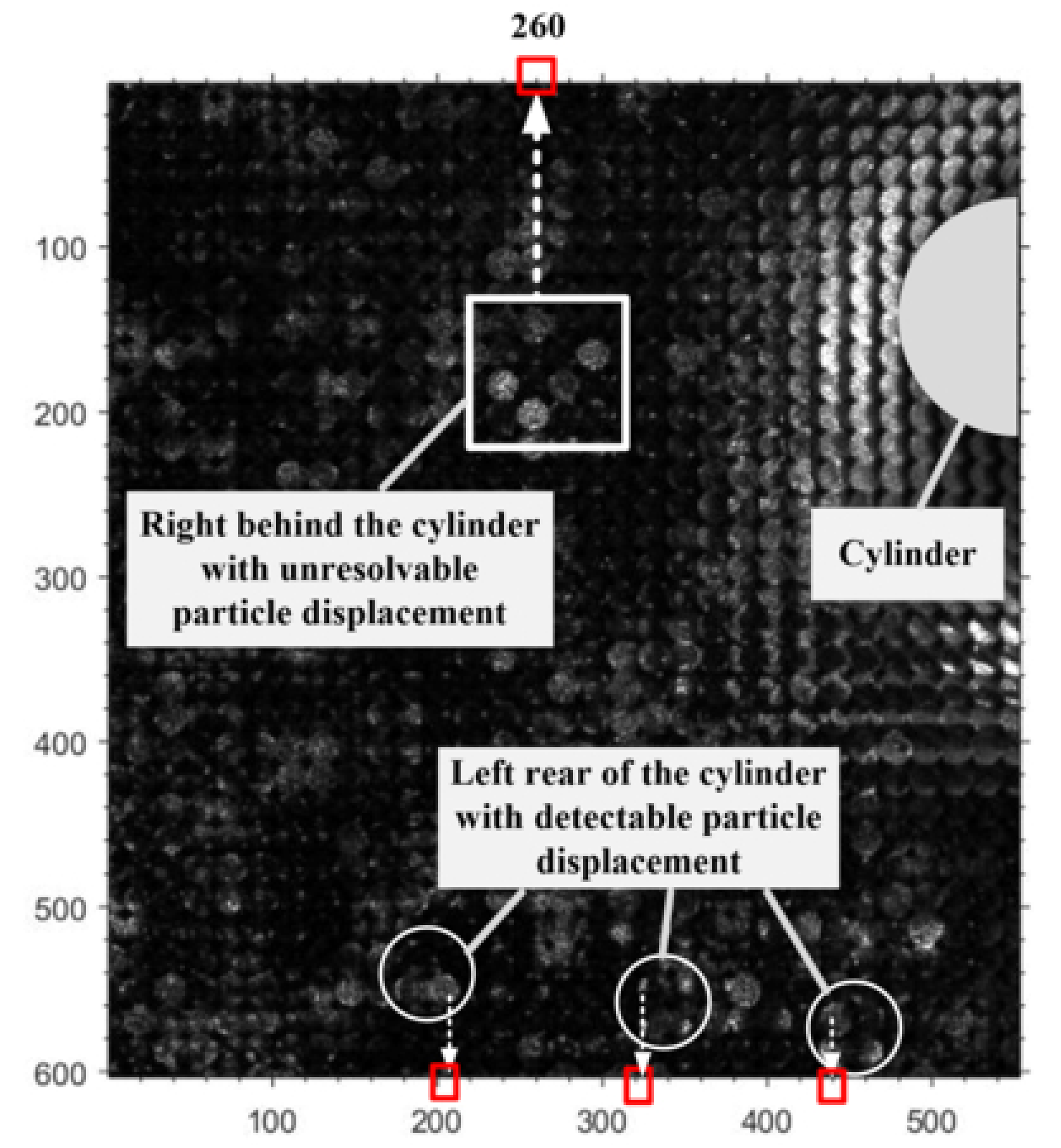
260
100
200
300
400
500
600
100
200
300
400
500
Right behind the cylinder with unresolvable particle displacement
Cylinder
Left rear of the cylinder with detectable particle displacement

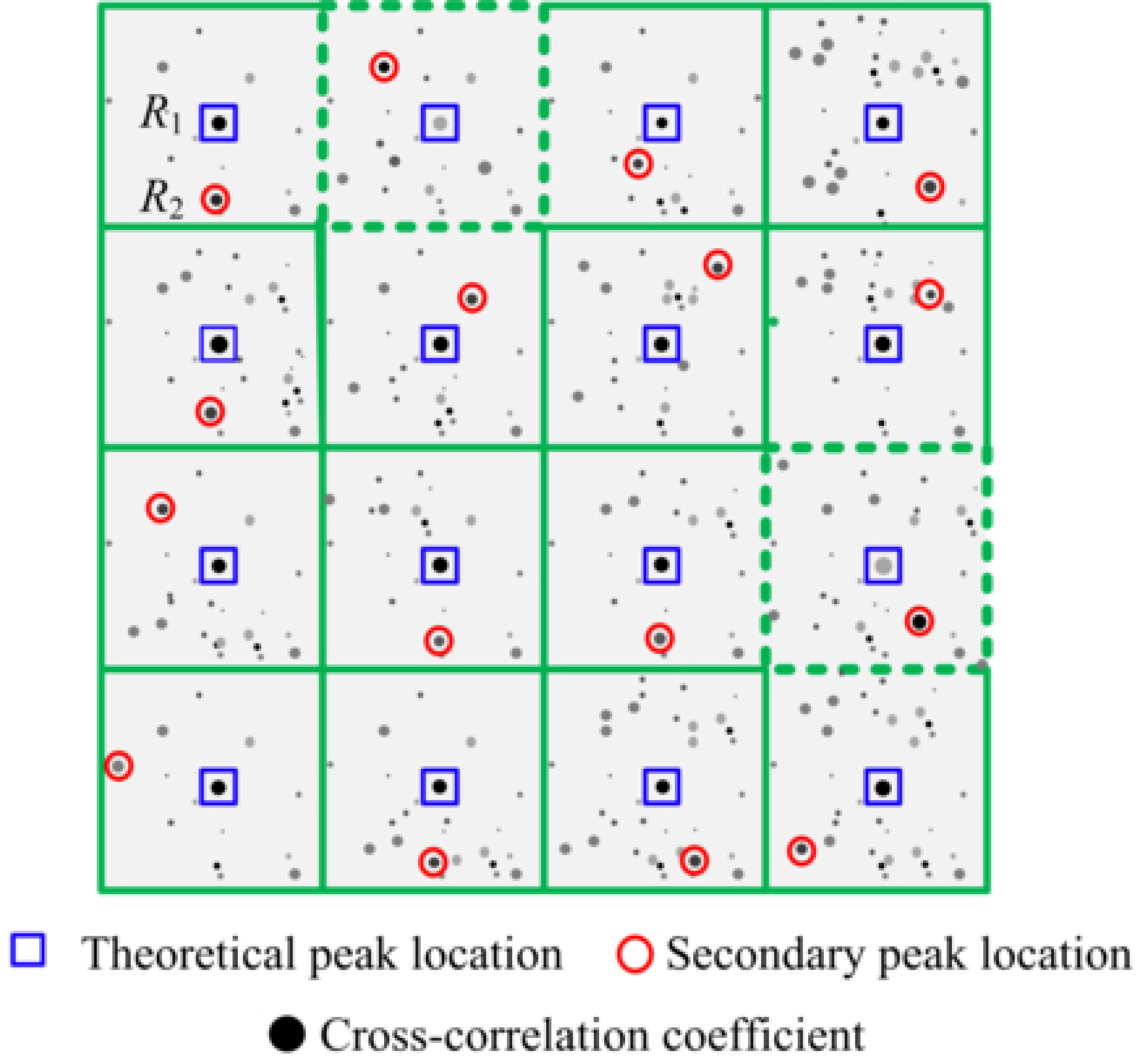
R_1
R_2
Theoretical peak location
Secondary peak location
Cross-correlation coefficient

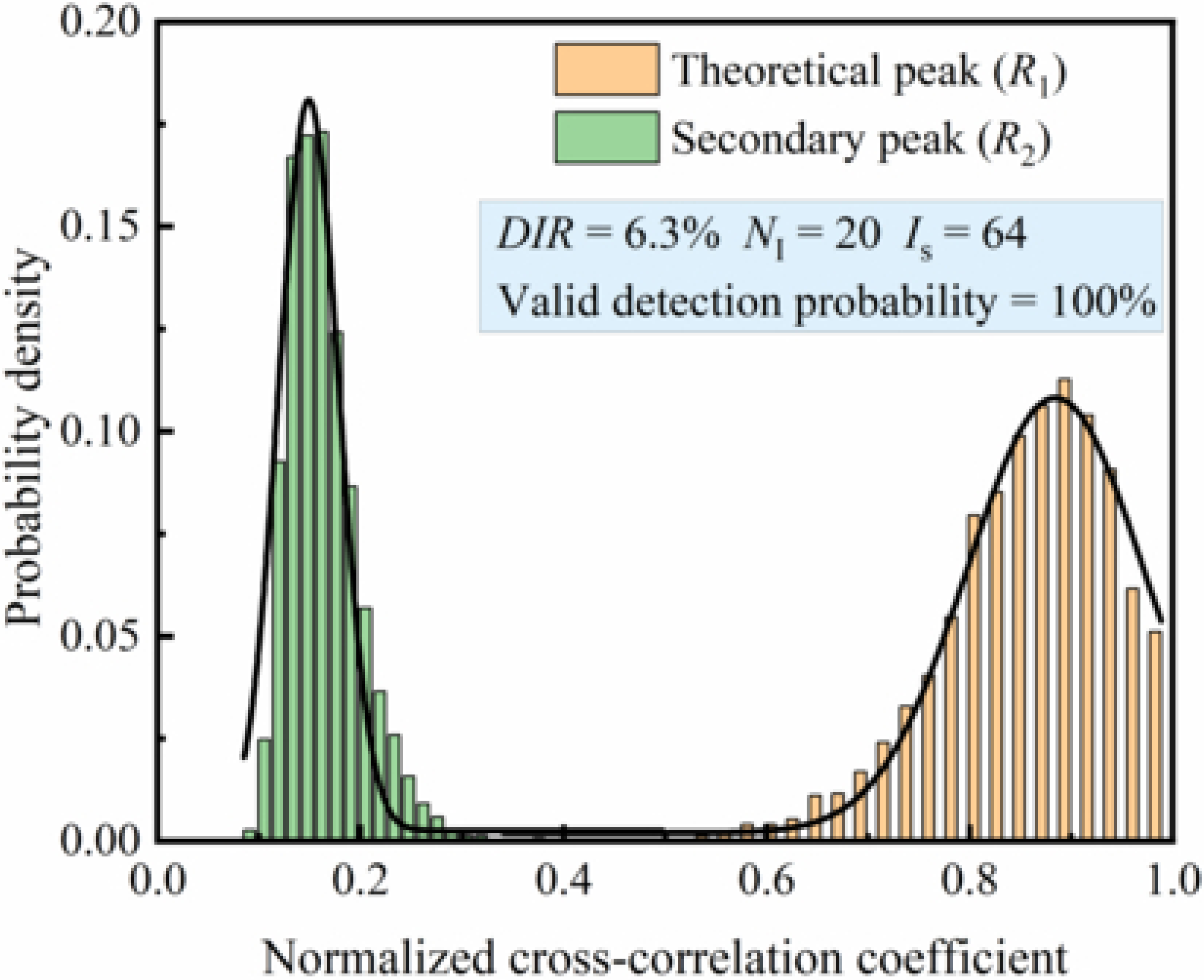
Theoretical peak (R_1)
Secondary peak (R_2)
DIR = 6.3% N_1 = 20 I_s = 64
Valid detection probability = 100%
Probability density
0.20
0.15
0.10
0.05
0.00
0.0
0.2
0.4
0.6
0.8
1.0
Normalized cross-correlation coefficient

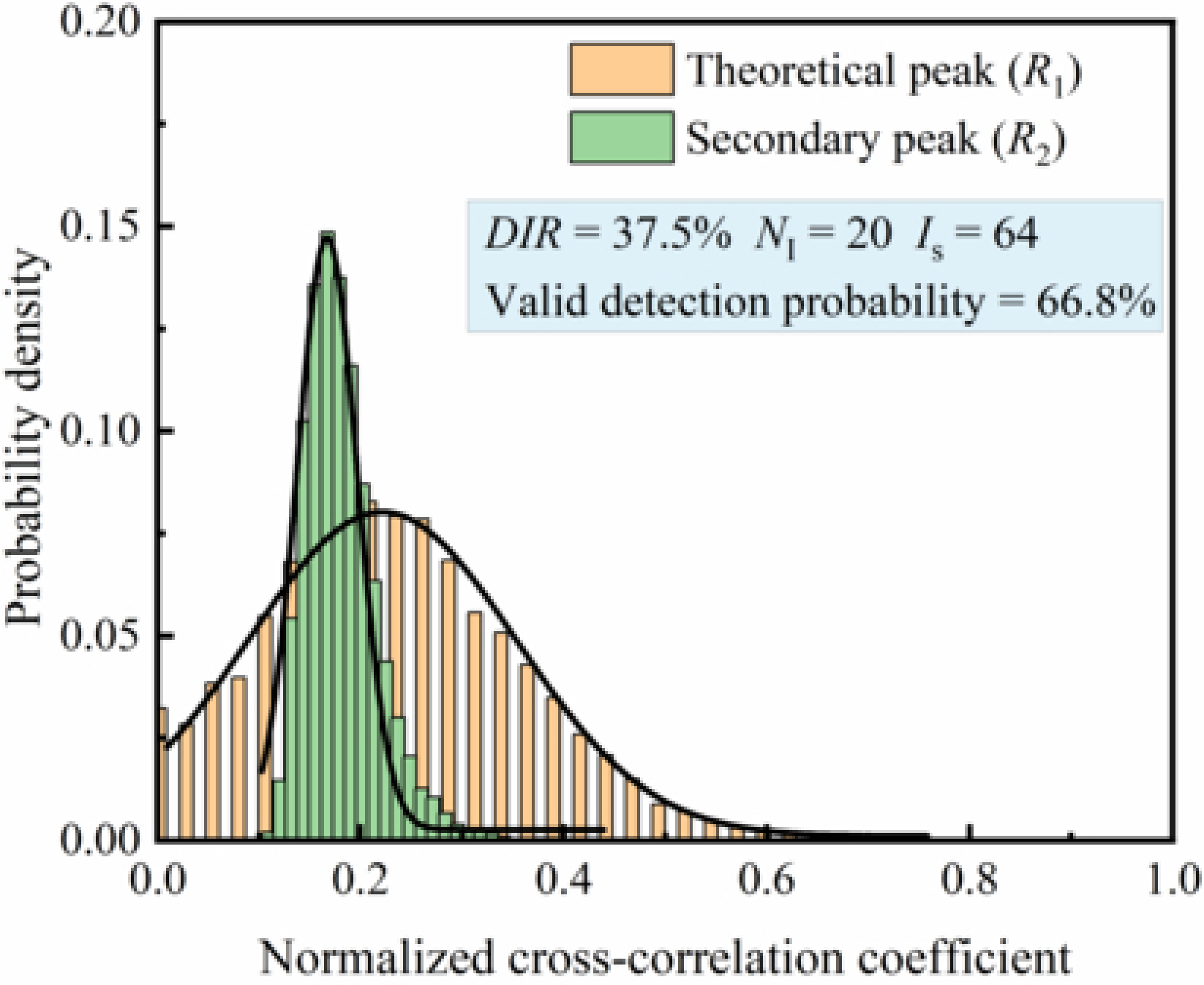
Theoretical peak (R_1)
Secondary peak (R_2)
DIR = 37.5% N_1 = 20 I_s = 64
Valid detection probability = 66.8%
Probability density
0.20
0.15
0.10
0.05
0.00
0.0
0.2
0.4
0.6
0.8
1.0
Normalized cross-correlation coefficient

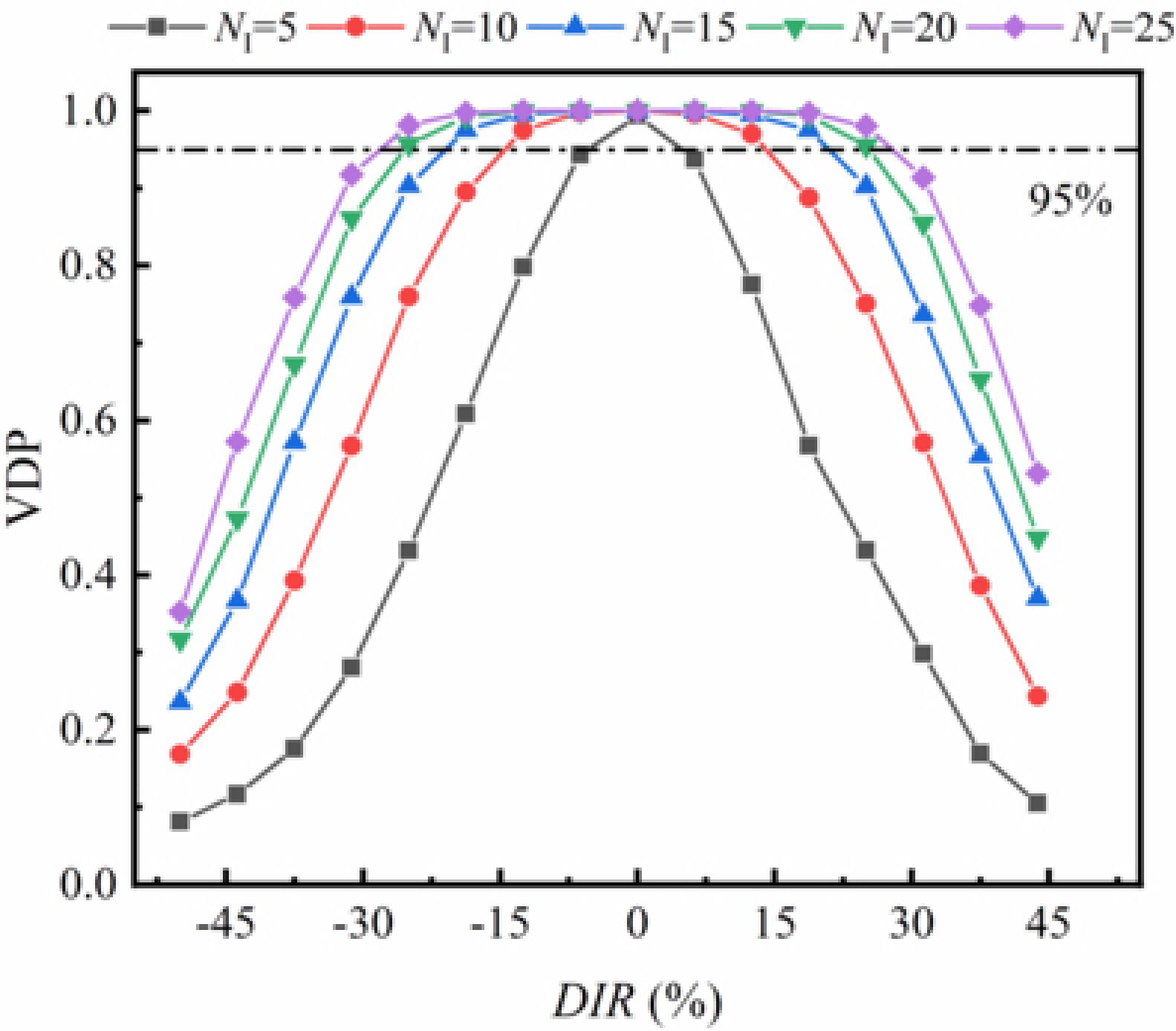
N_l=5
N_l=10
N_l=15
N_l=20
N_l=25
95%
VDP
1.0
0.8
0.6
0.4
0.2
0.0
-45
-30
-15
0
15
30
45
DIR (%)

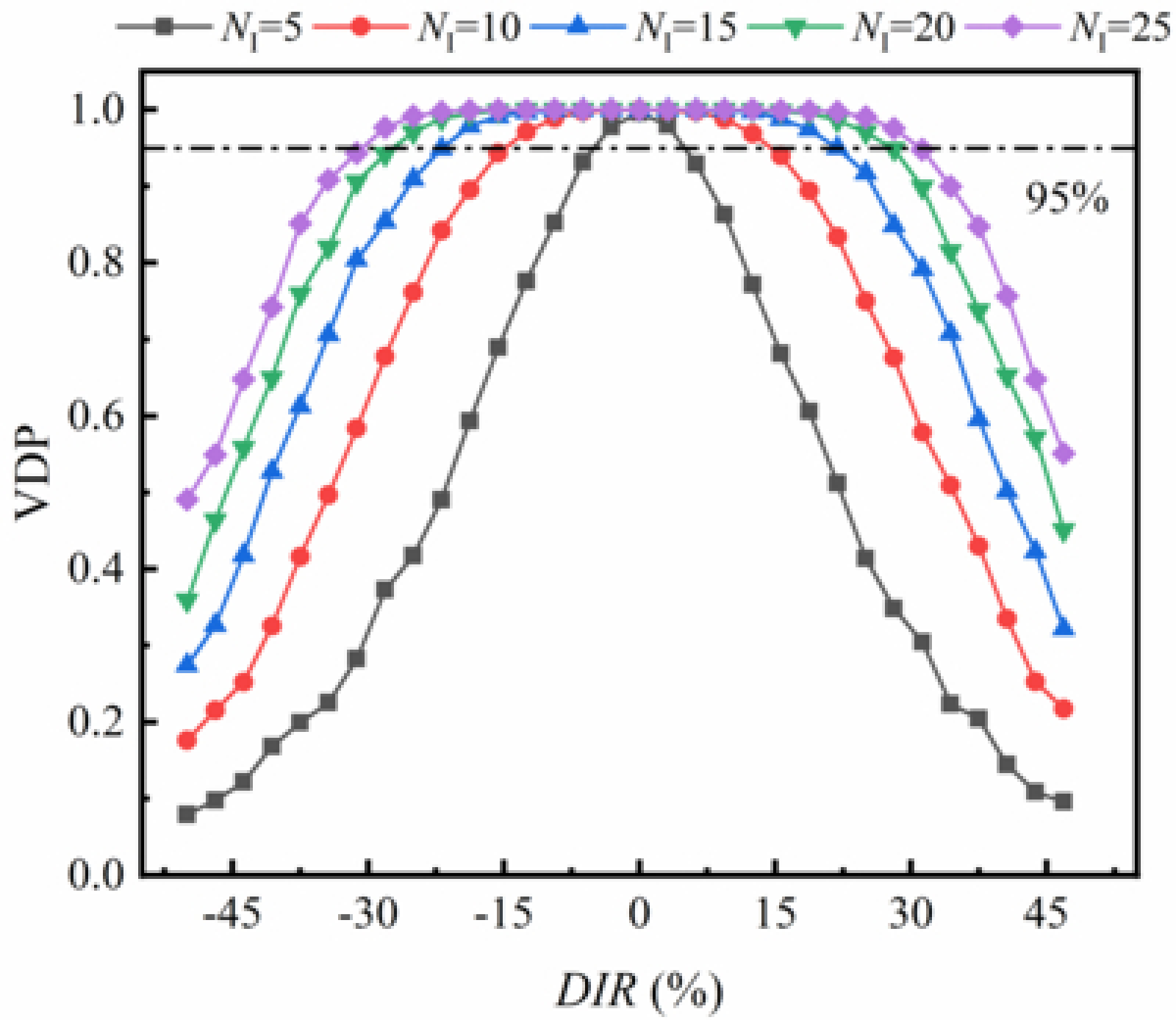
N_l=5
N_l=10
N_l=15
N_l=20
N_l=25
95%
VDP
1.0
0.8
0.6
0.4
0.2
0.0
-45
-30
-15
0
15
30
45
DIR (%)

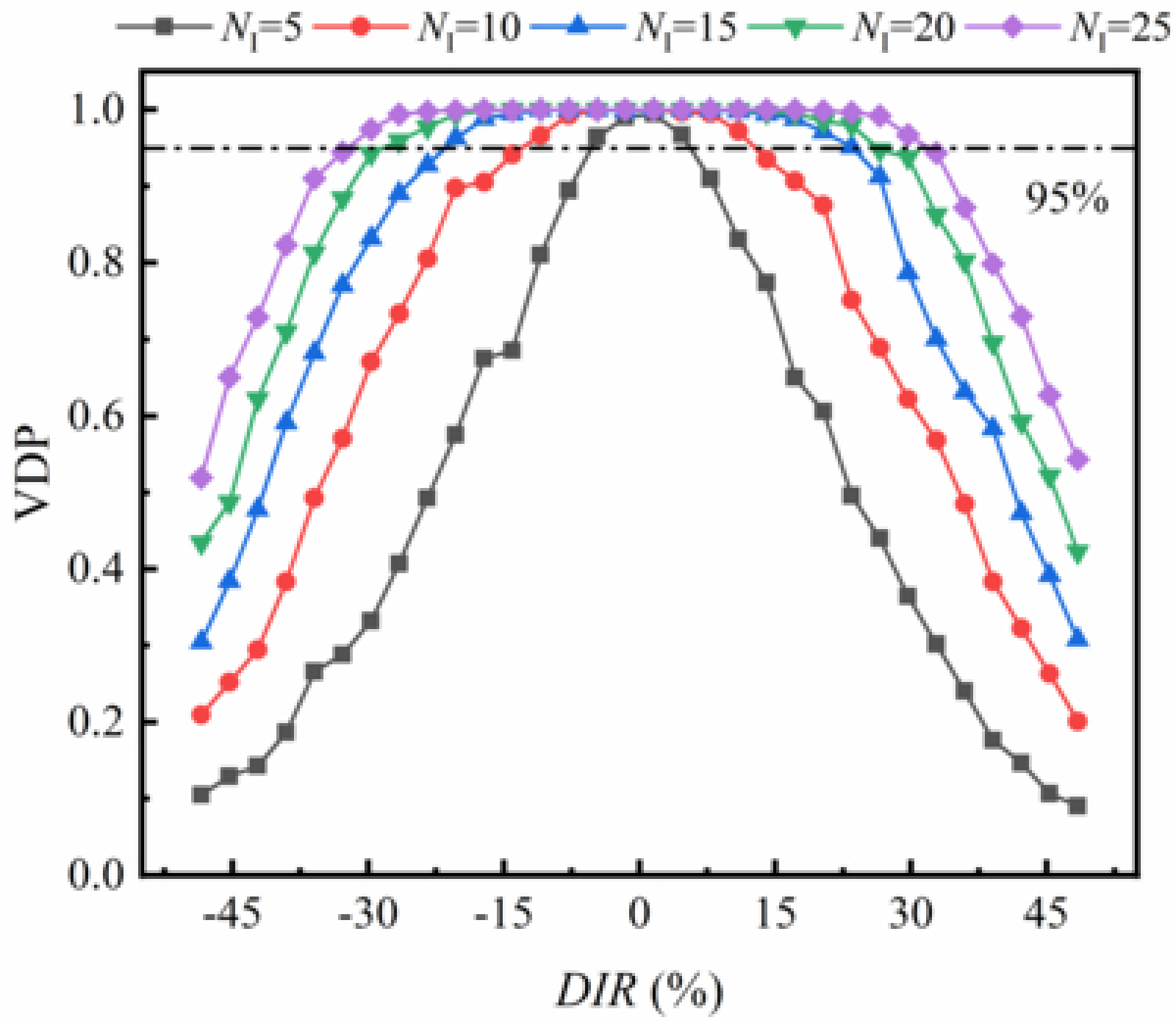
N_l=5
N_l=10
N_l=15
N_l=20
N_l=25
95%
VDP
1.0
0.8
0.6
0.4
0.2
0.0
-45
-30
-15
0
15
30
45
DIR (%)

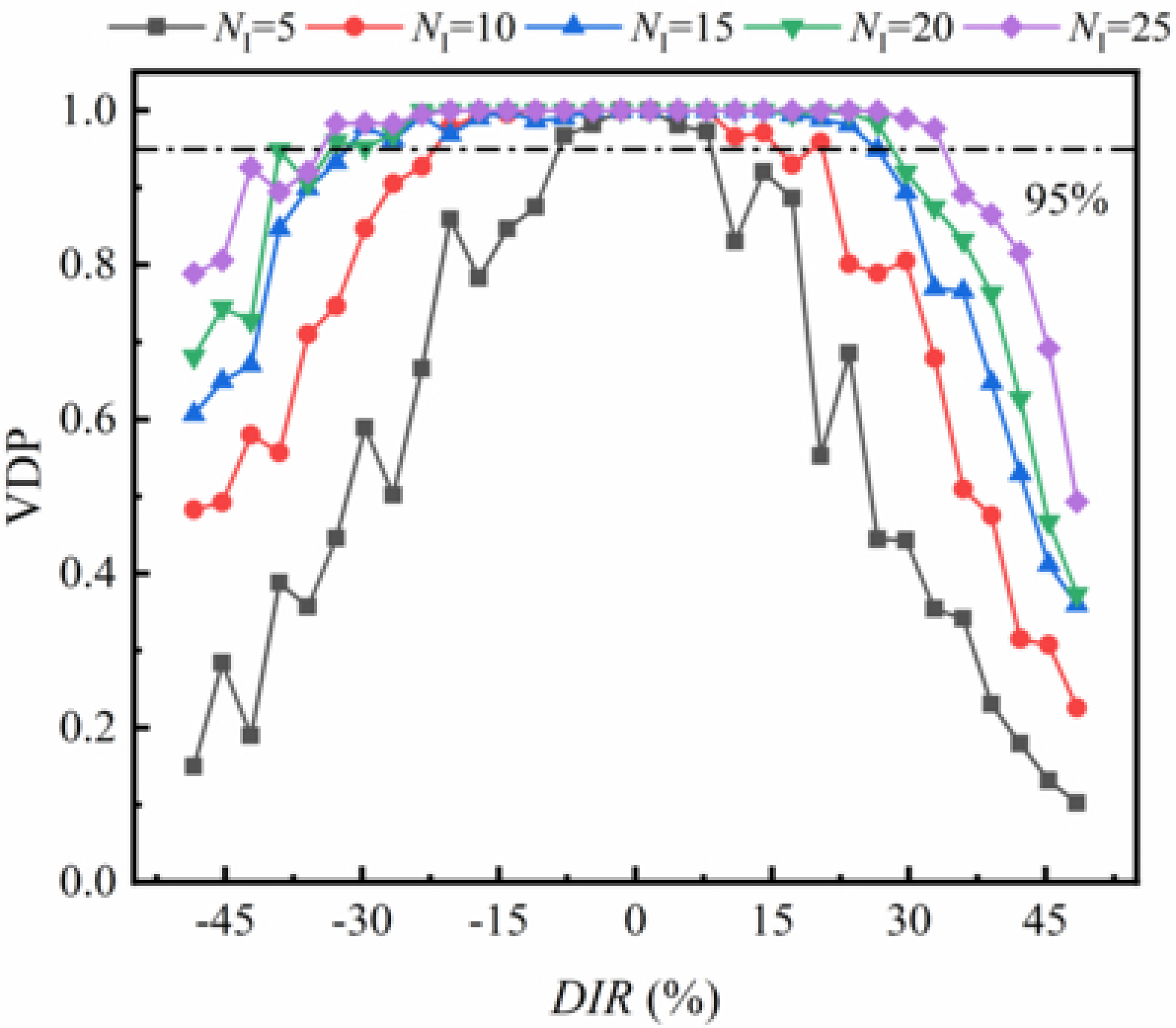
N_t=5
N_t=10
N_t=15
N_t=20
N_t=25
95%
VDP
1.0
0.8
0.6
0.4
0.2
0.0
-45
-30
-15
0
15
30
45
DIR (%)

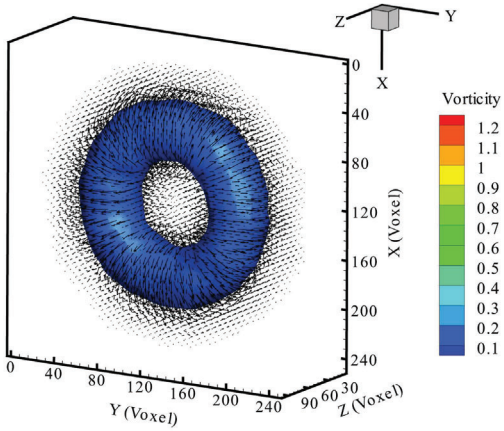

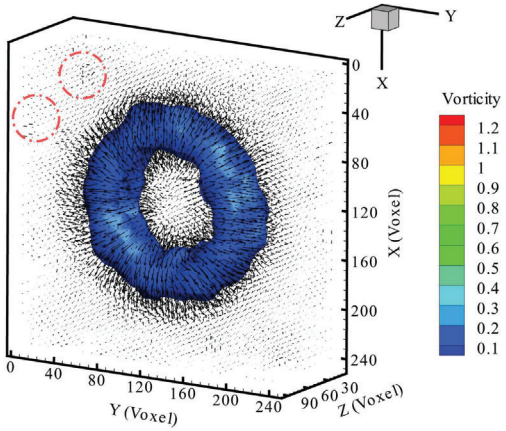

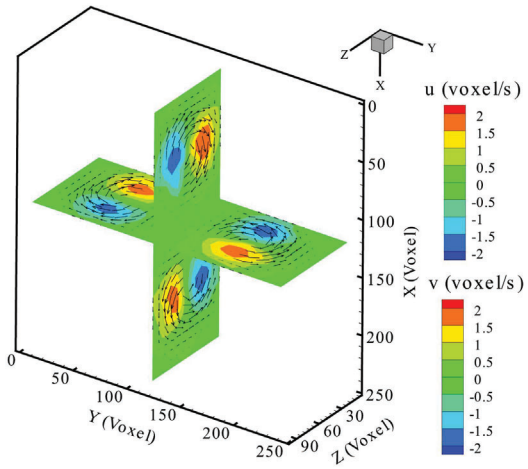

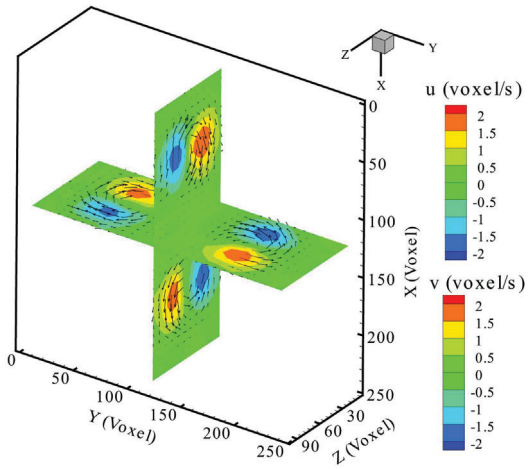

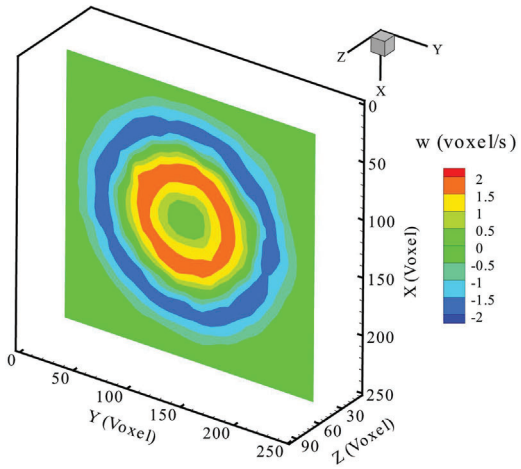

Accepted to Phys. Fluids 10.1063/5.0098933

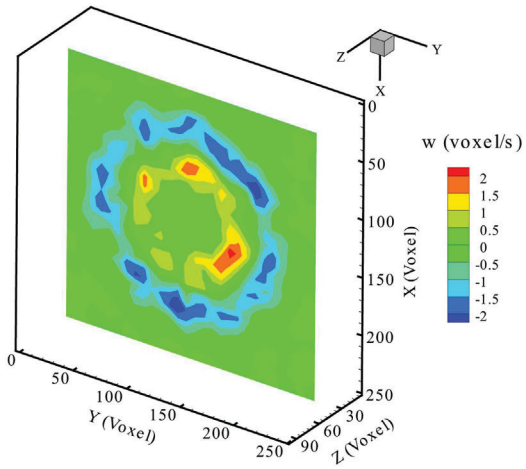

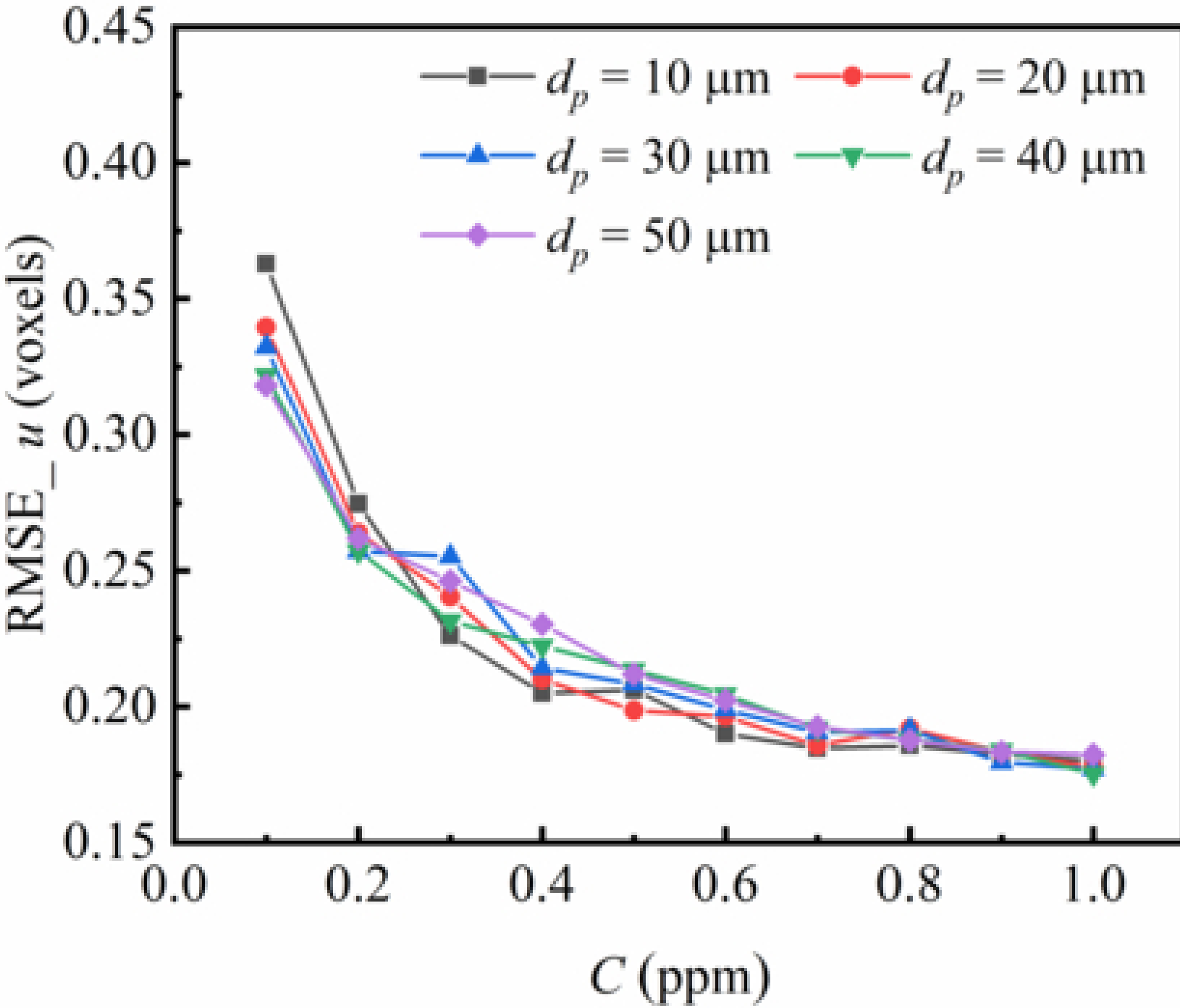
0.45
0.40
0.35
0.30
0.25
0.20
0.15
RMSE_u (voxels)
0.0
0.2
0.4
0.6
0.8
1.0
C (ppm)
d_p = 10 μm
d_p = 20 μm
d_p = 30 μm
d_p = 40 μm
d_p = 50 μm

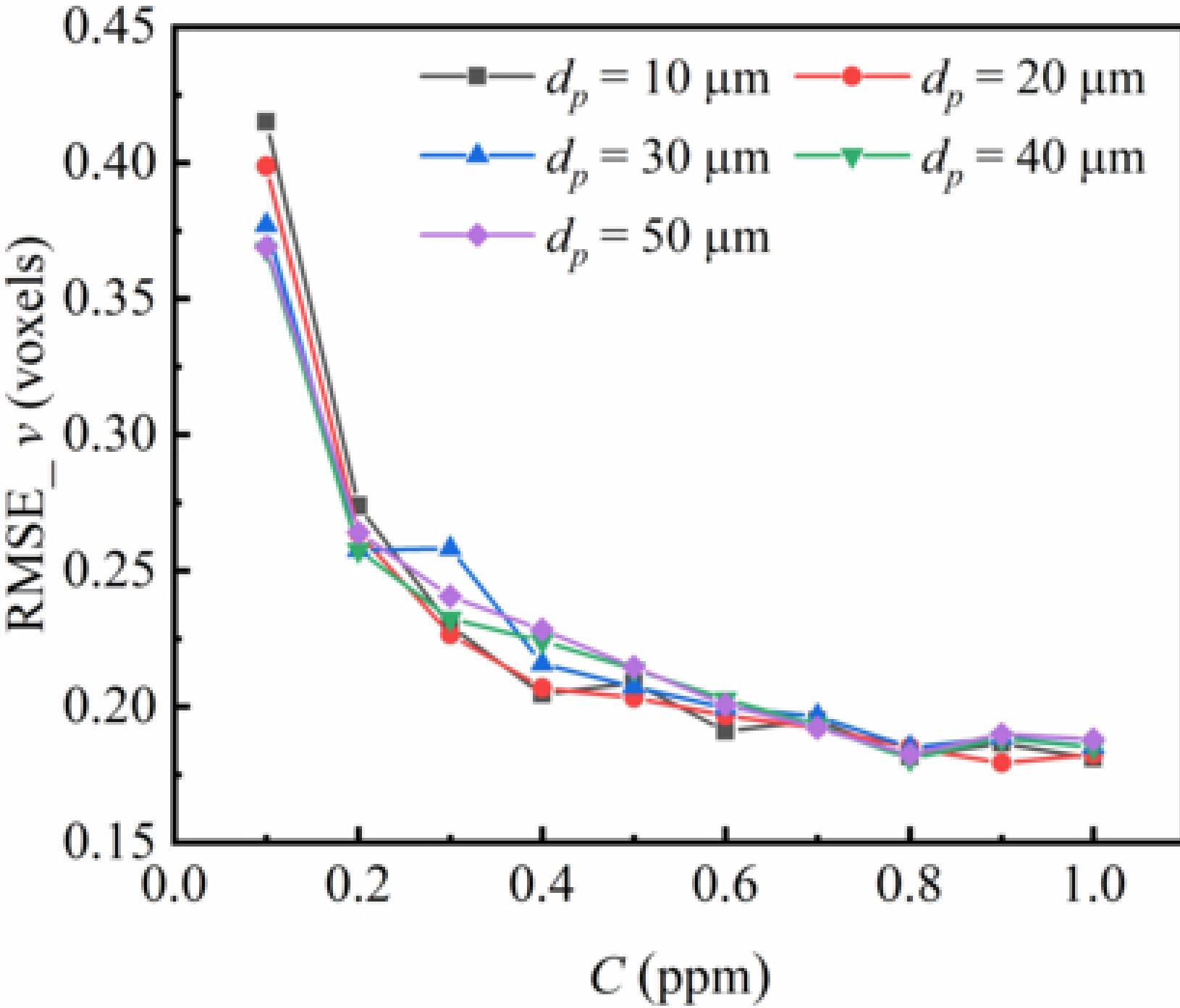
0.45
0.40
0.35
0.30
0.25
0.20
0.15
RMSE_v (voxels)
0.0
0.2
0.4
0.6
0.8
1.0
C (ppm)
d_p = 10 μm
d_p = 20 μm
d_p = 30 μm
d_p = 40 μm
d_p = 50 μm

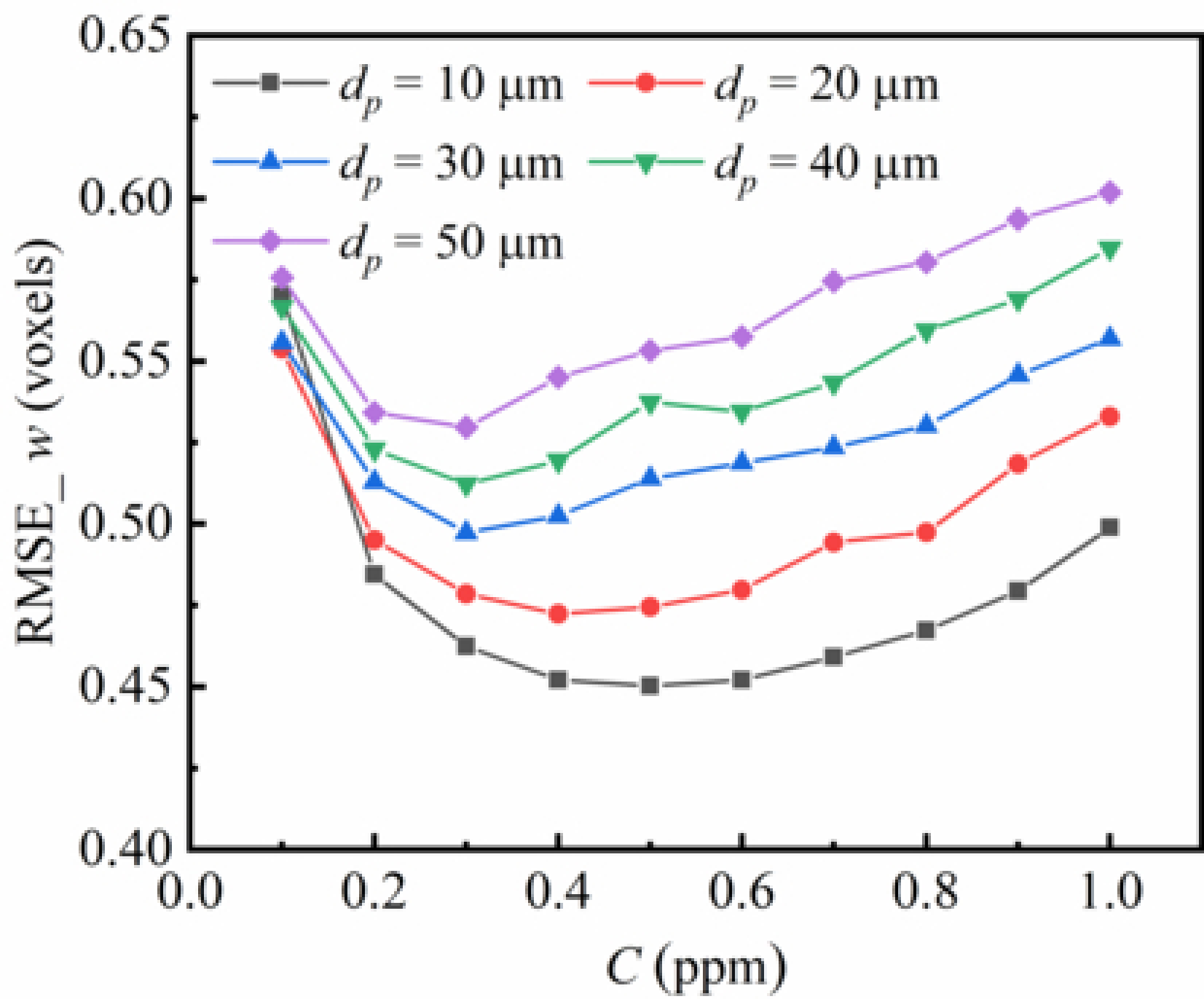
0.65
0.60
0.55
0.50
0.45
0.40
RMSE_w (voxels)
0.0
0.2
0.4
0.6
0.8
1.0
C (ppm)
d_p = 10 μm
d_p = 20 μm
d_p = 30 μm
d_p = 40 μm
d_p = 50 μm

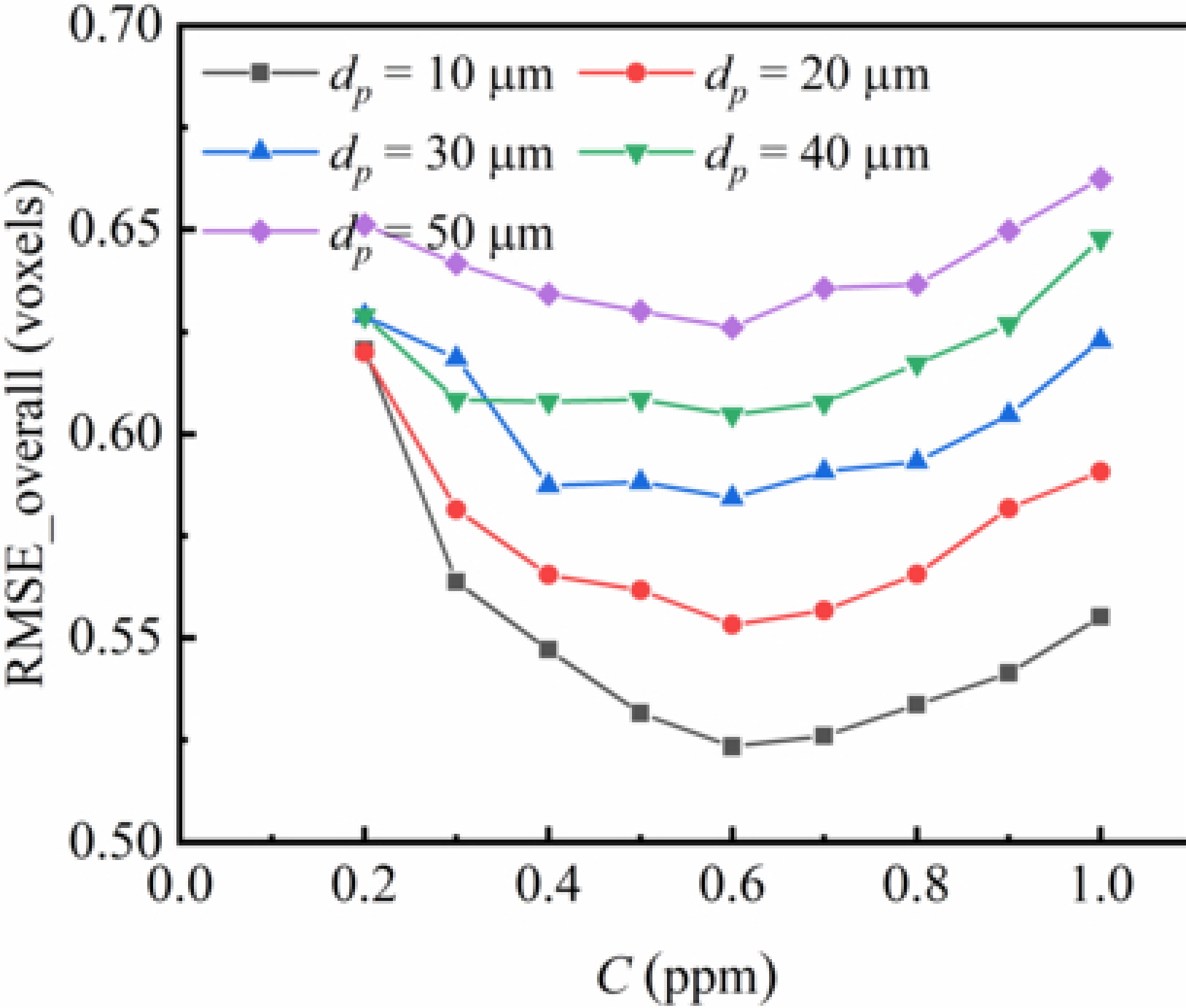
0.70
0.65
0.60
0.55
0.50
RMSE_overall (voxels)
0.0
0.2
0.4
0.6
0.8
1.0
C (ppm)
d_p = 10 μm
d_p = 20 μm
d_p = 30 μm
d_p = 40 μm
d_p = 50 μm

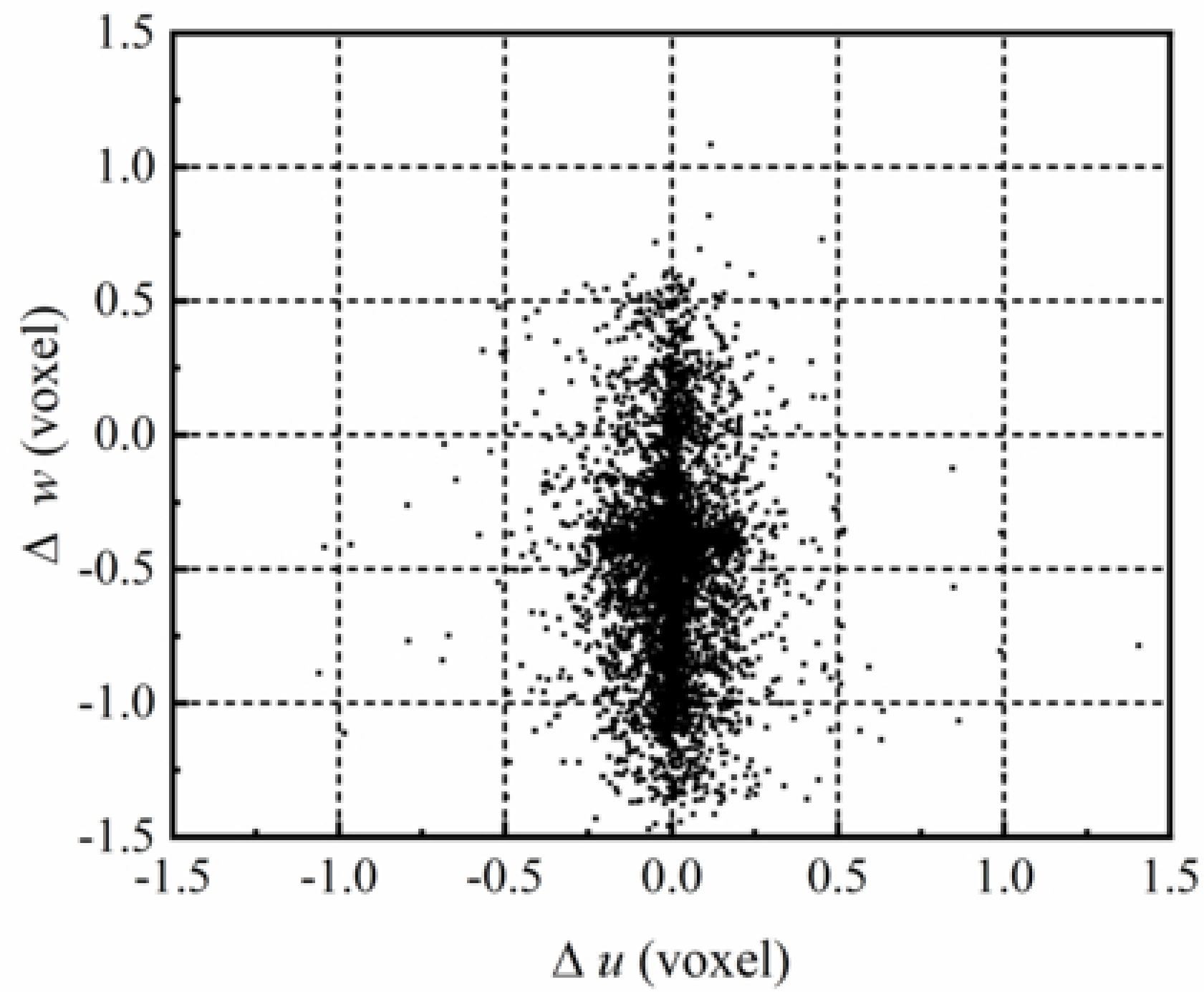
1.5
1.0
0.5
0.0
-0.5
-1.0
-1.5
Δ w (voxel)
-1.5
-1.0
-0.5
0.0
0.5
1.0
1.5
Δ u (voxel)

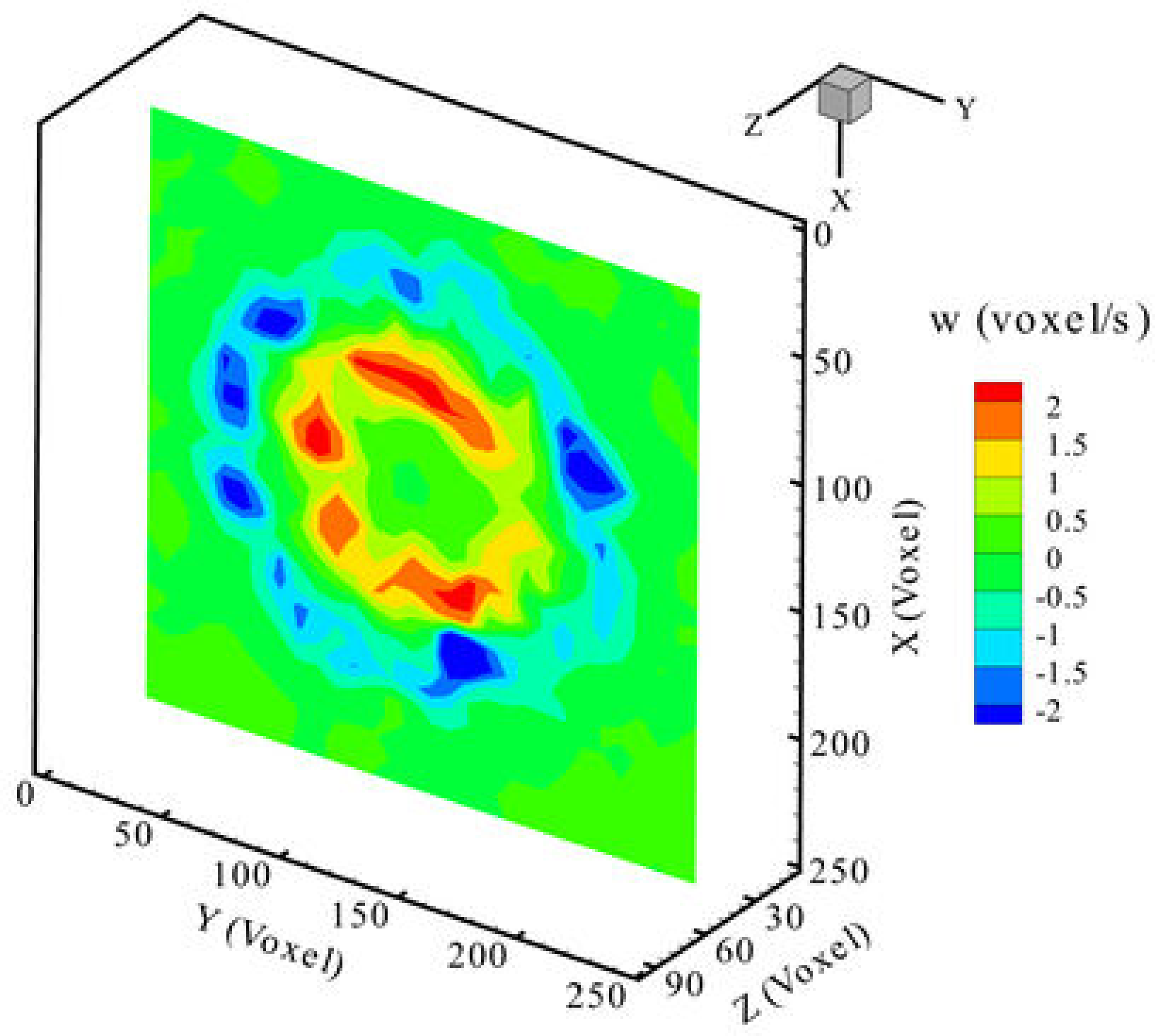
Z
Y
X
0
50
100
150
200
250
X (Voxel)
w (voxel/s)
2
1.5
1
0.5
0
-0.5
-1
-1.5
-2
0
50
100
150
200
250
Y (Voxel)
30
60
90
Z (Voxel)

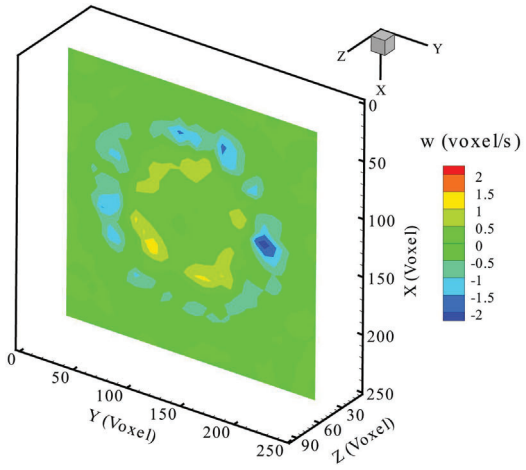

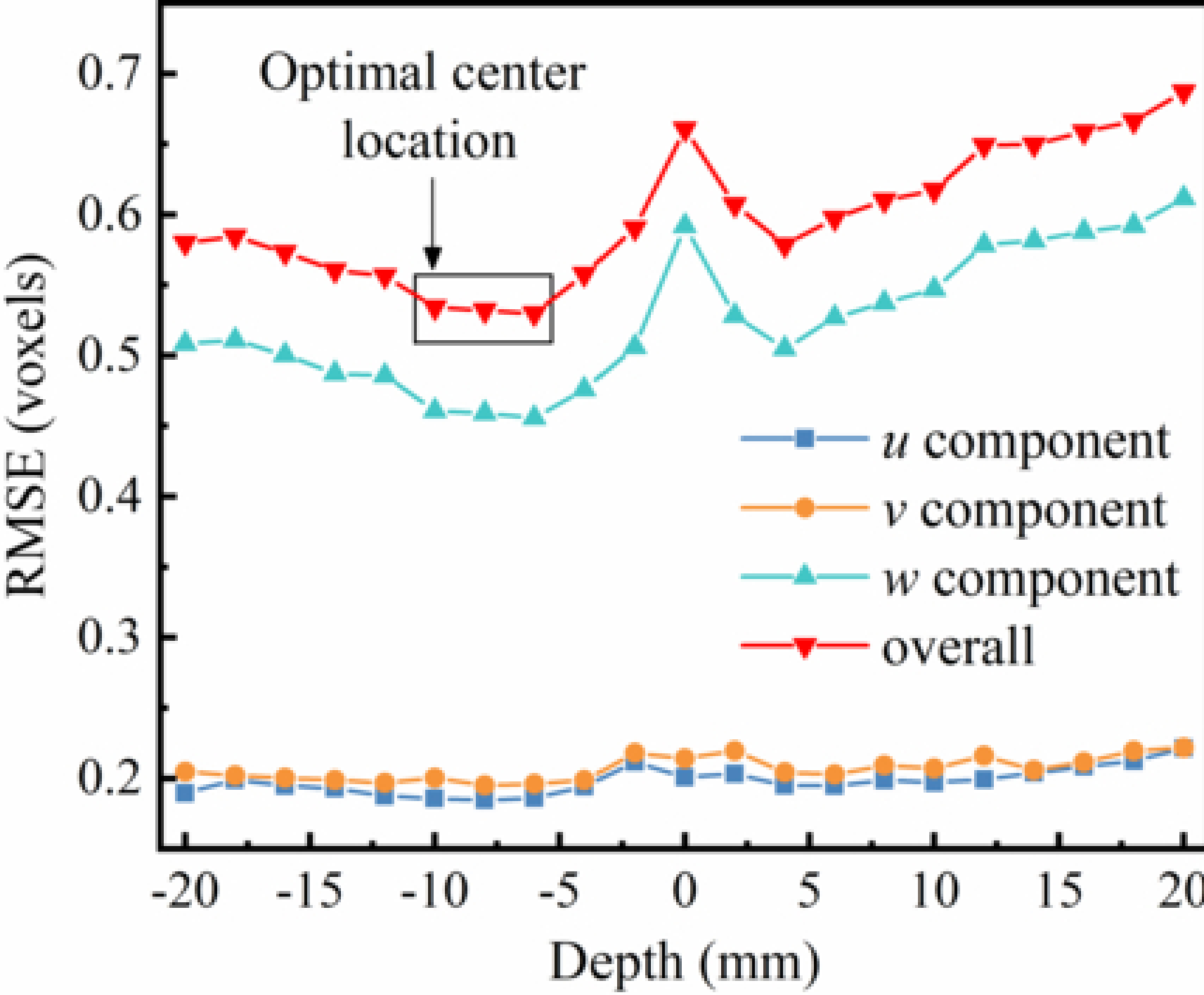
Optimal center location
RMSE (voxels)
0.7
0.6
0.5
0.4
0.3
0.2
-20
-15
-10
-5
0
5
10
15
20
Depth (mm)
u component
v component
w component
overall

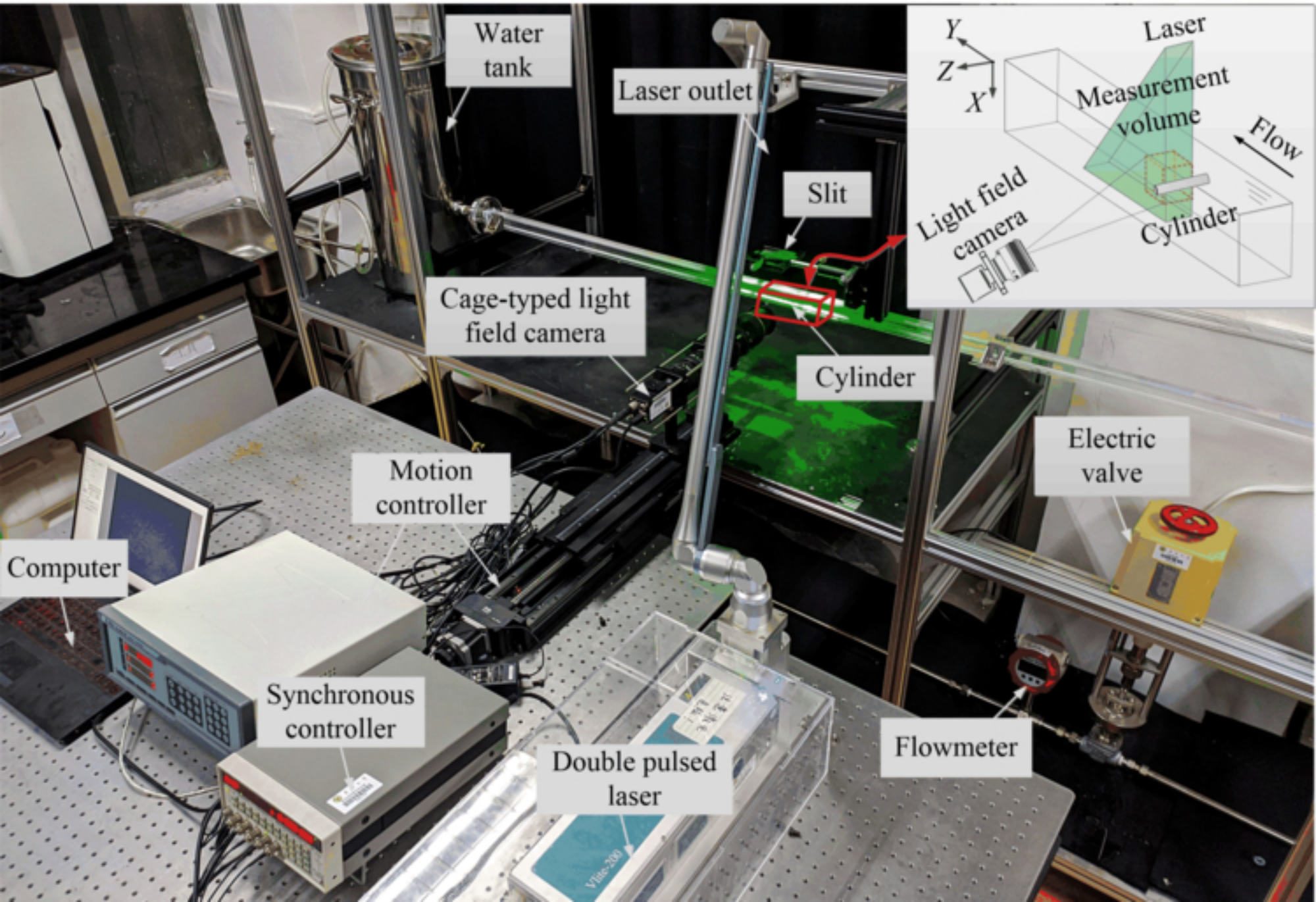
Water tank
Laser outlet
Slit
Cage-typed light field camera
Cylinder
Motion controller
Electric valve
Computer
Synchronous controller
Double pulsed laser
Flowmeter
Y
Z
X
Laser
Measurement volume
Flow
Light field camera
Cylinder

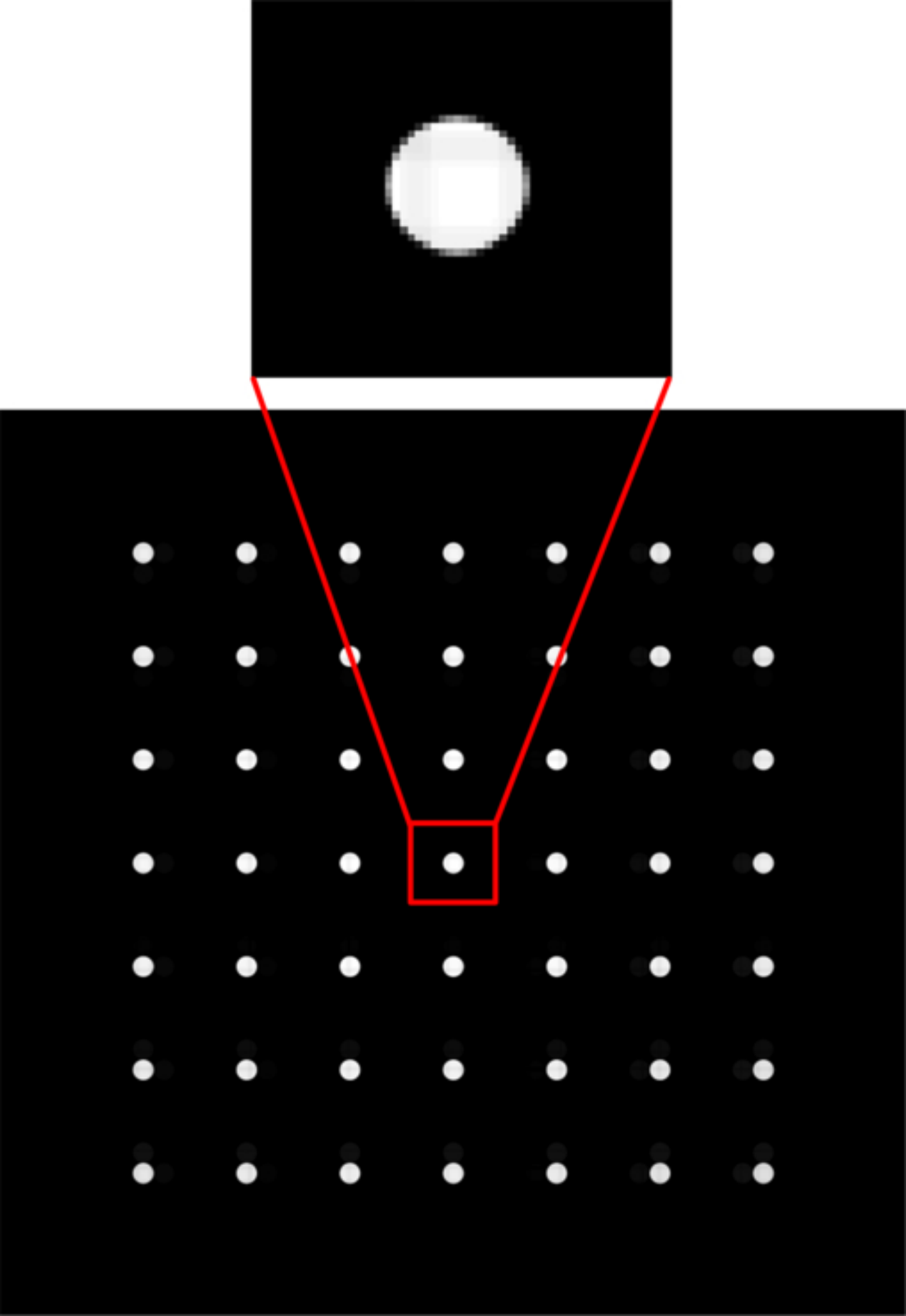

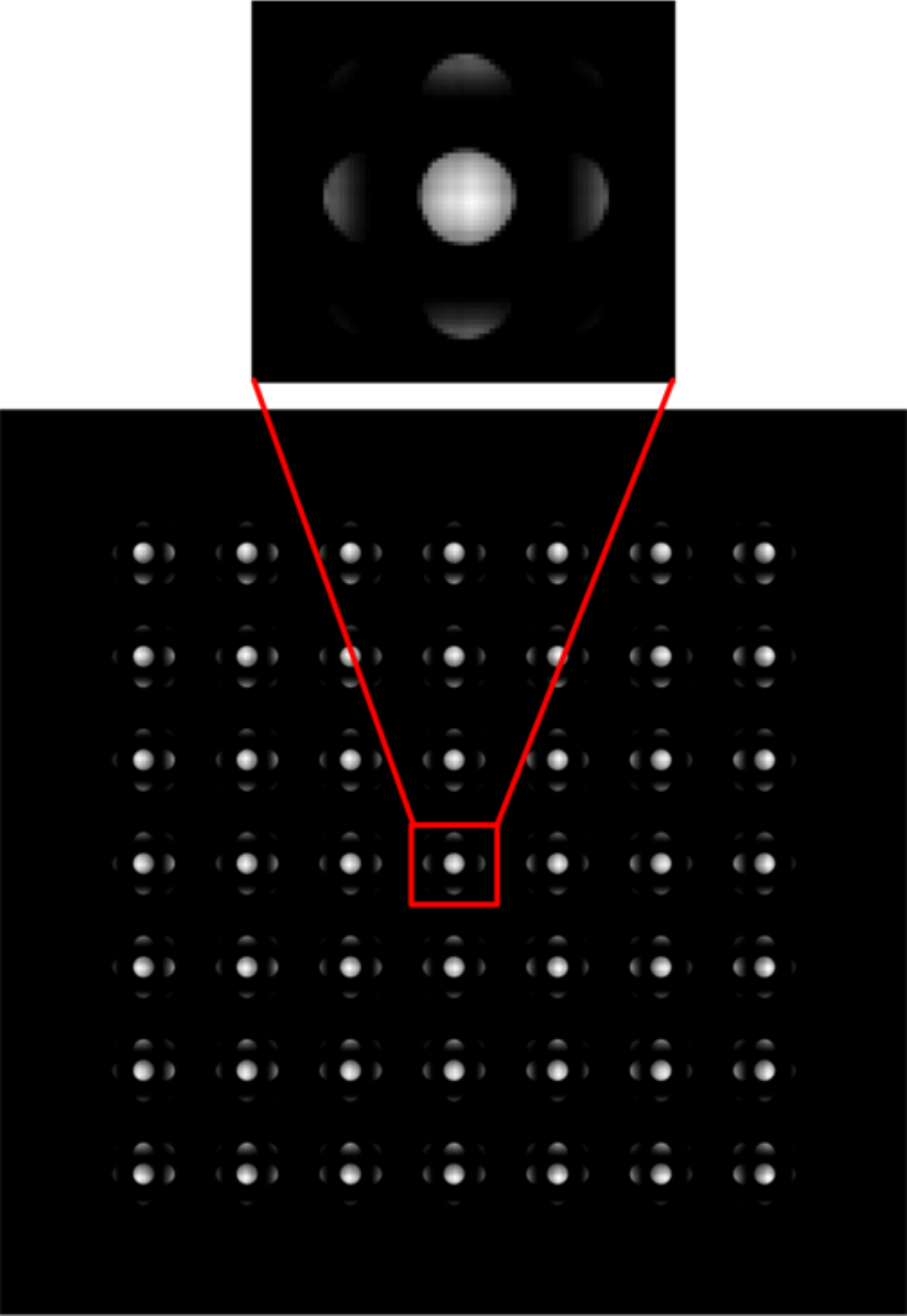

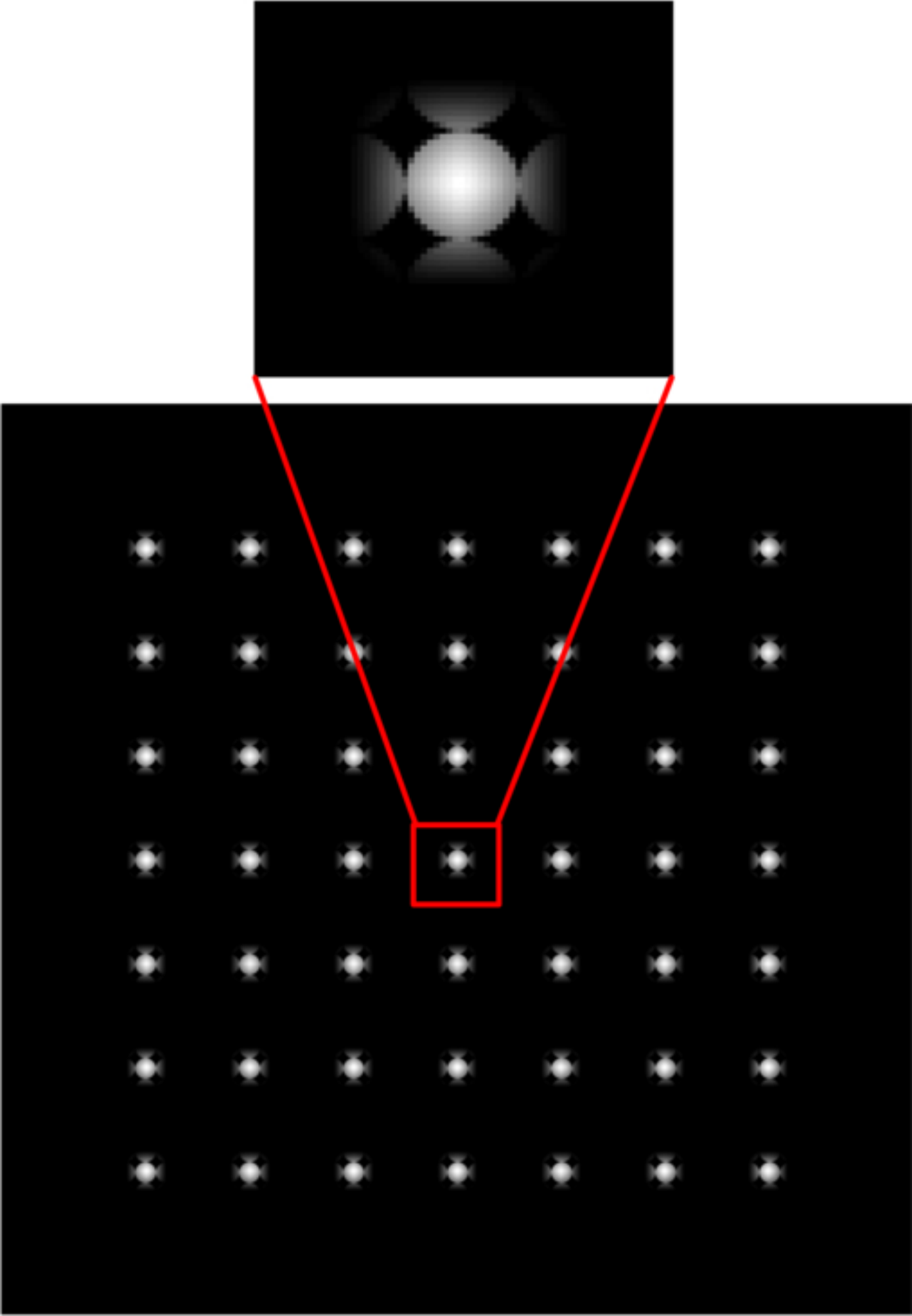

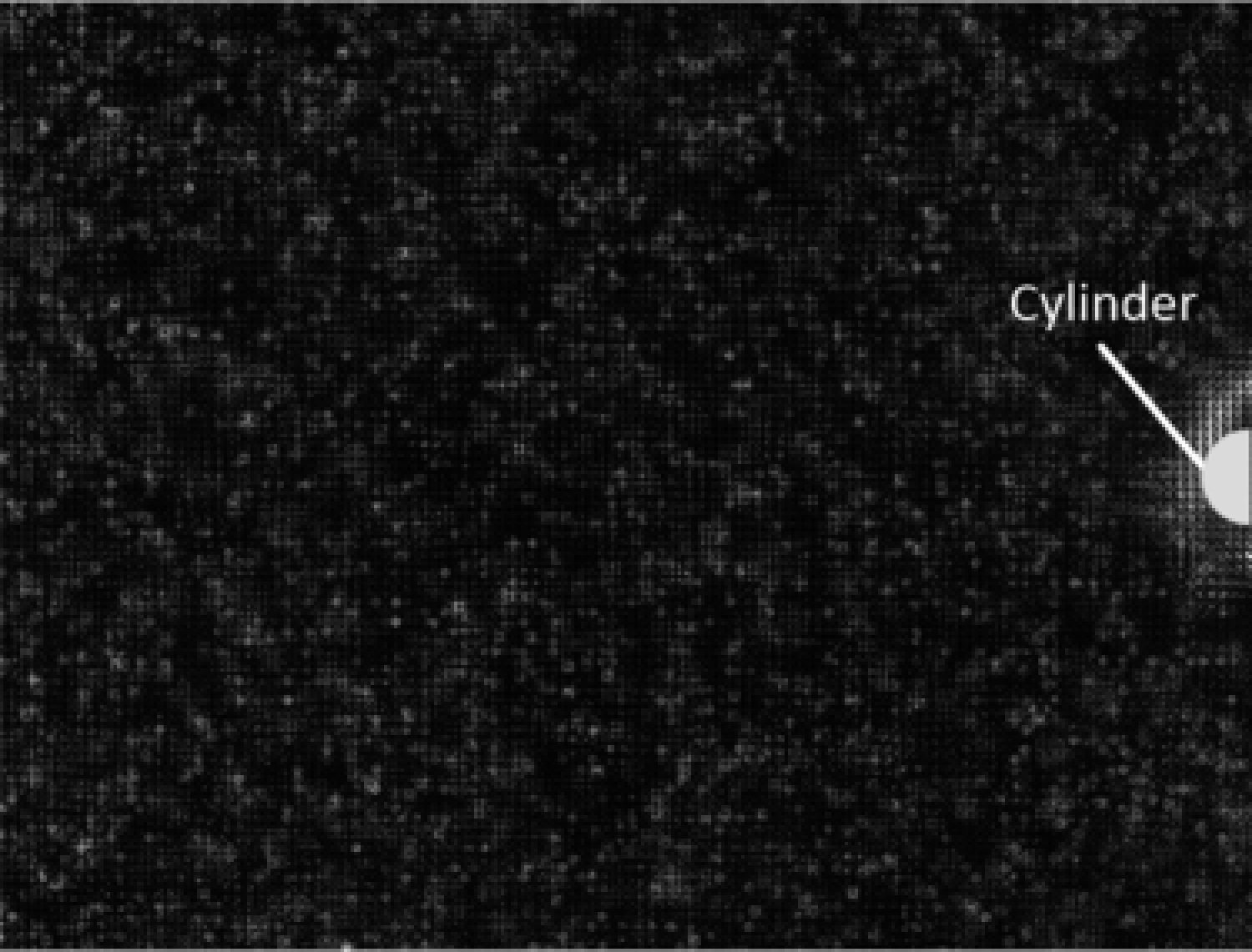
Cylinder

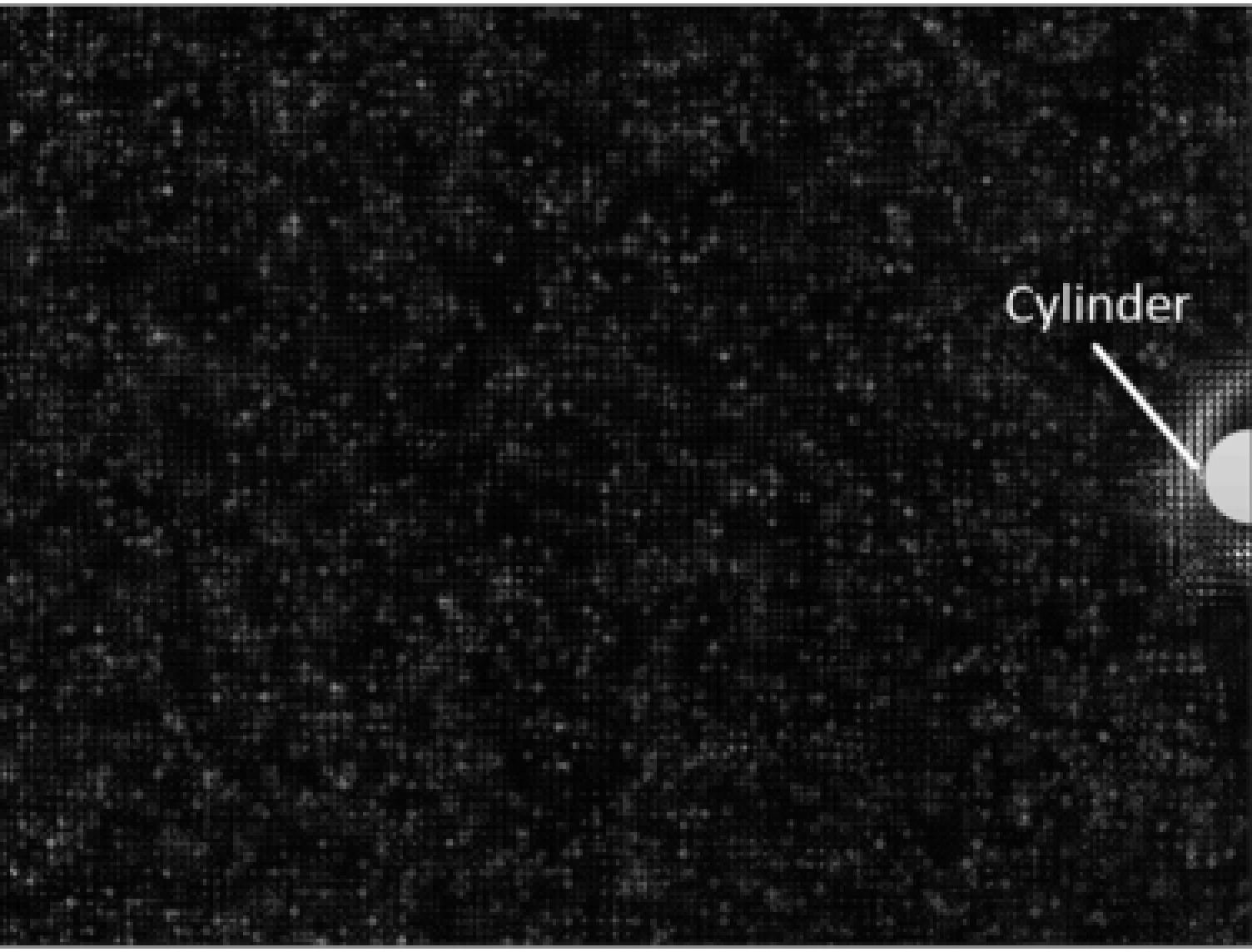
Cylinder

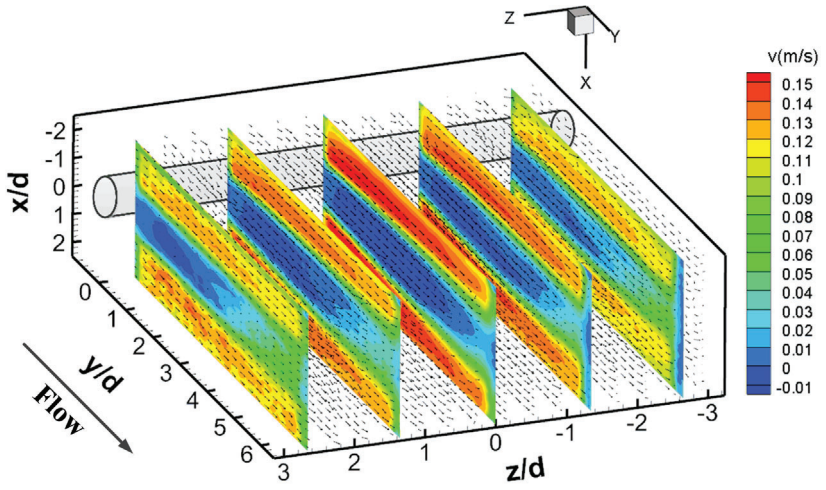

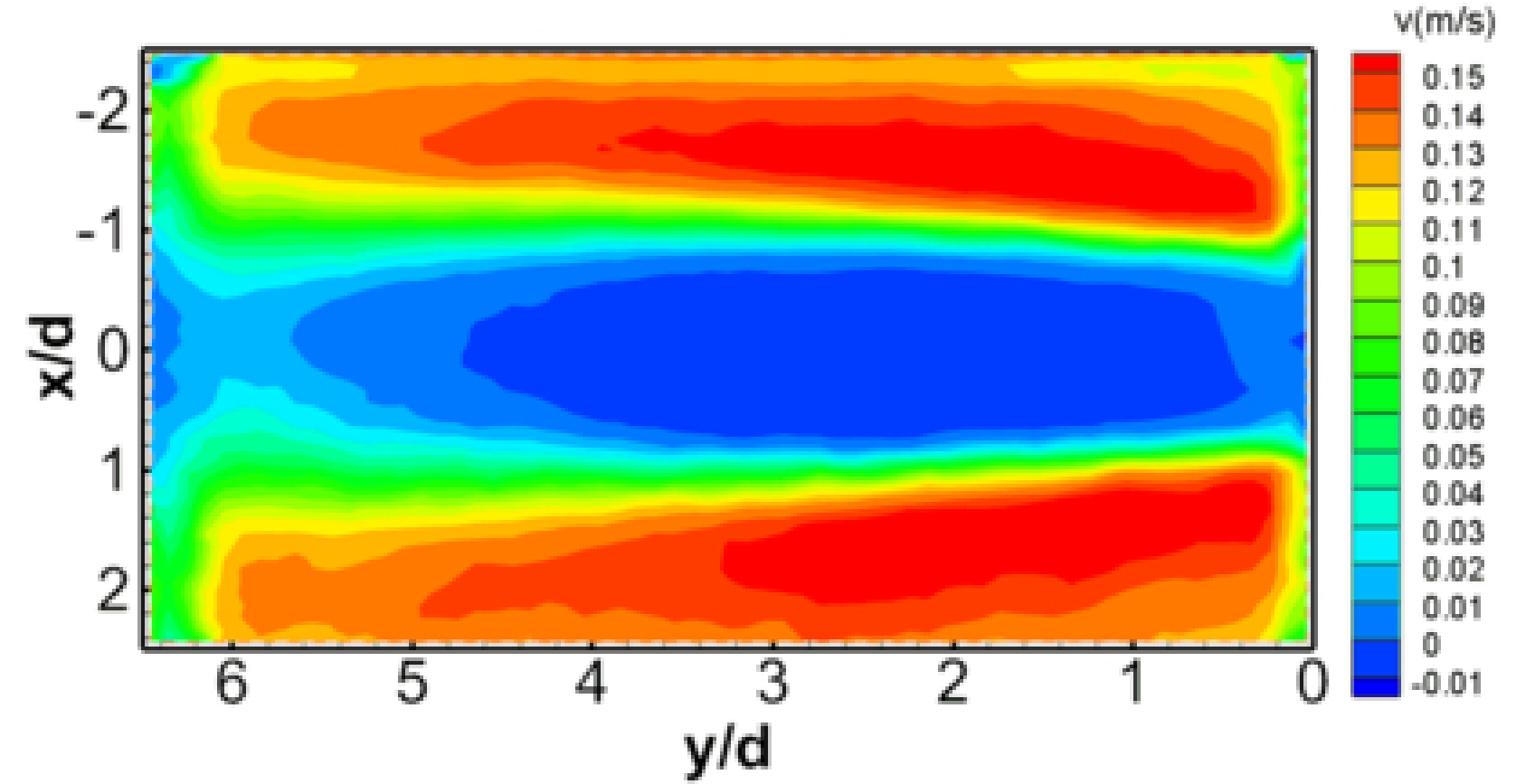
v(m/s)
0.15
0.14
0.13
0.12
0.11
0.1
0.09
0.08
0.07
0.06
0.05
0.04
0.03
0.02
0.01
0
-0.01
x/d
-2
-1
0
1
2
y/d
6
5
4
3
2
1
0

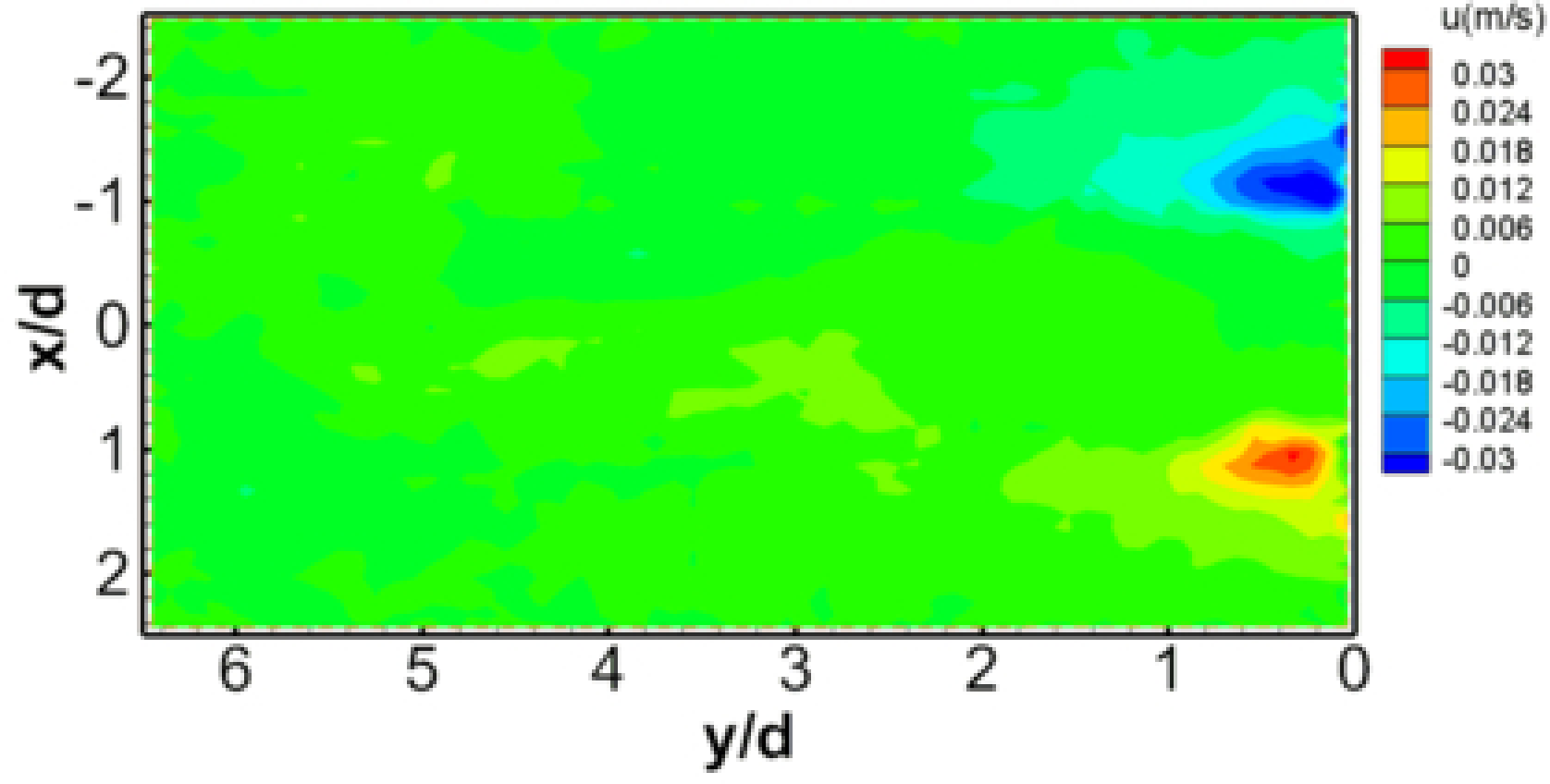
u(m/s)
0.03
0.024
0.018
0.012
0.006
0
-0.006
-0.012
-0.018
-0.024
-0.03
x/d
-2
-1
0
1
2
y/d
6
5
4
3
2
1
0

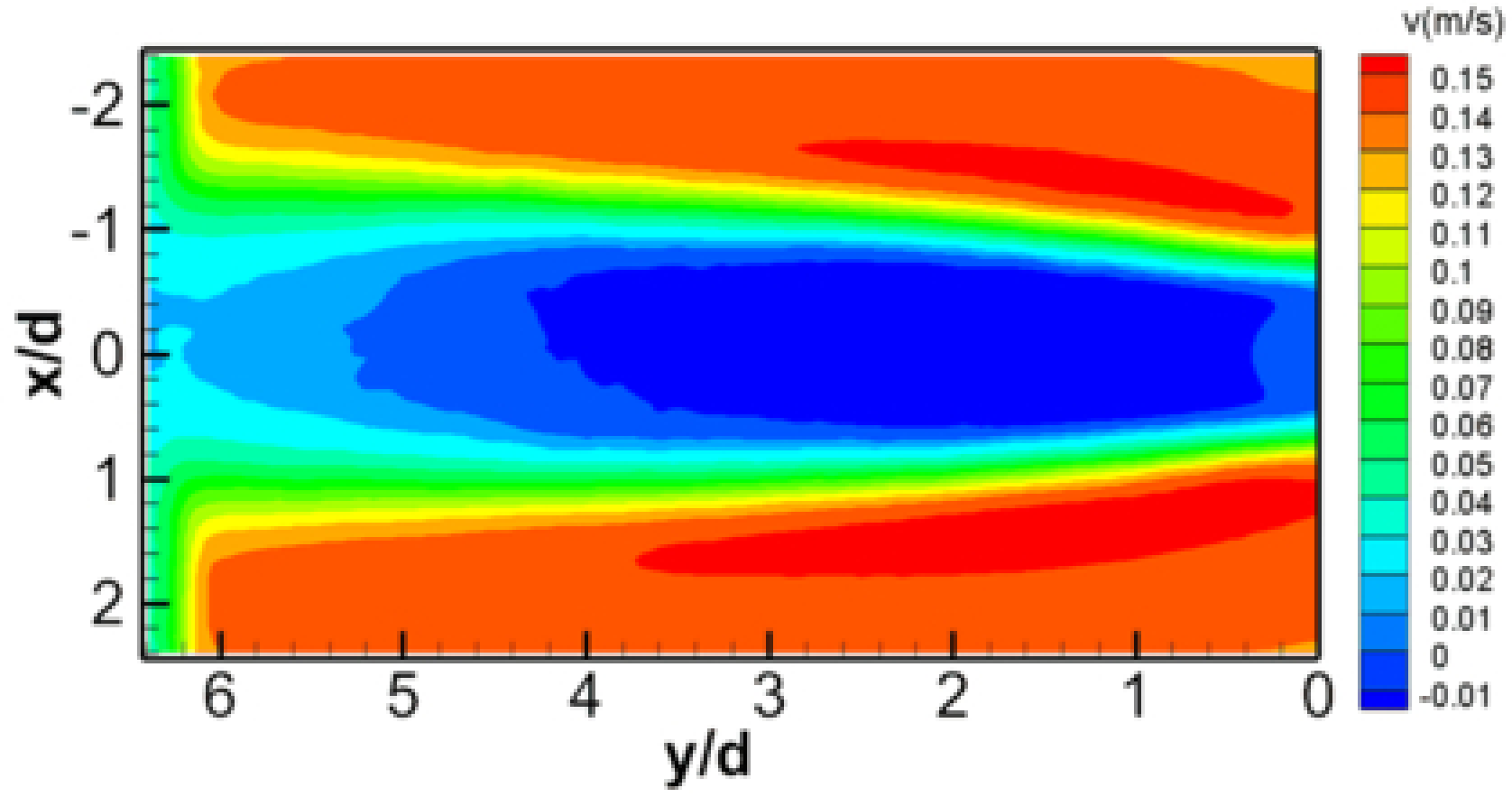
v(m/s)
0.15
0.14
0.13
0.12
0.11
0.1
0.09
0.08
0.07
0.06
0.05
0.04
0.03
0.02
0.01
0
-0.01
x/d
-2
-1
0
1
2
y/d
6
5
4
3
2
1
0

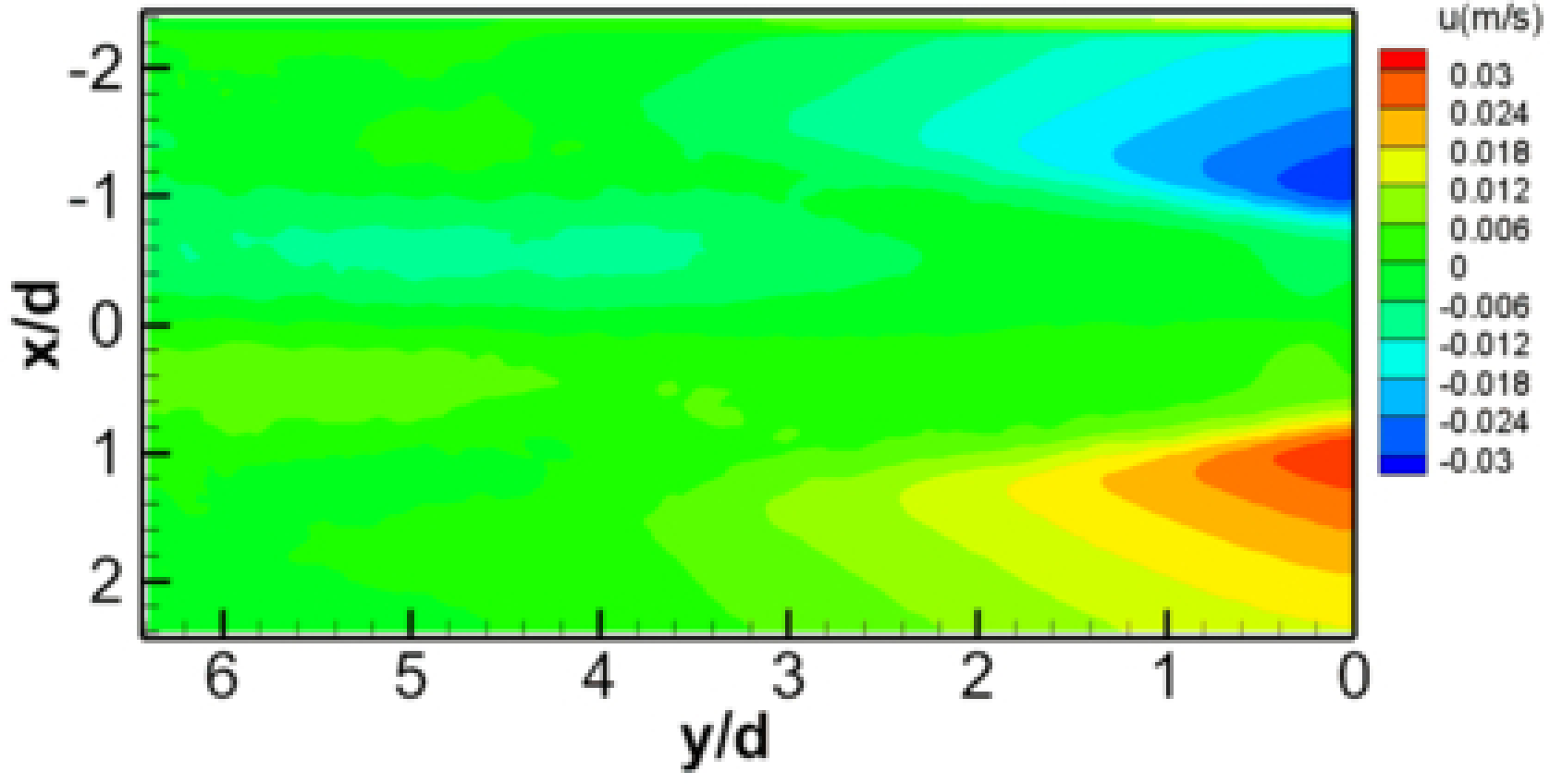
u(m/s)
0.03
0.024
0.018
0.012
0.006
0
-0.006
-0.012
-0.018
-0.024
-0.03
x/d
-2
-1
0
1
2
y/d
6
5
4
3
2
1
0

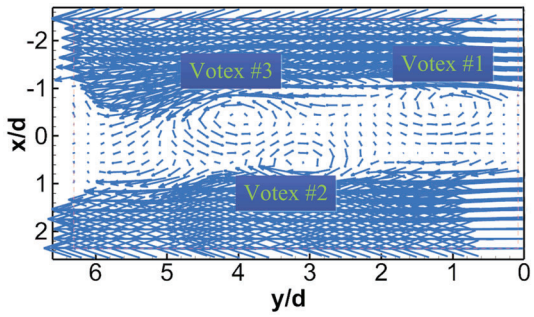

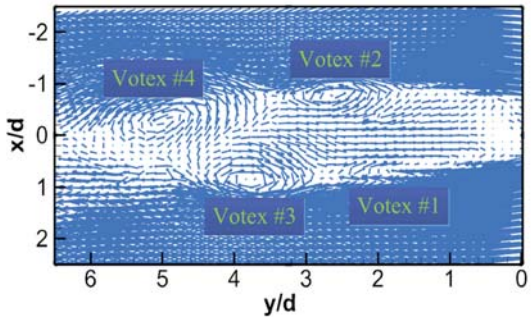

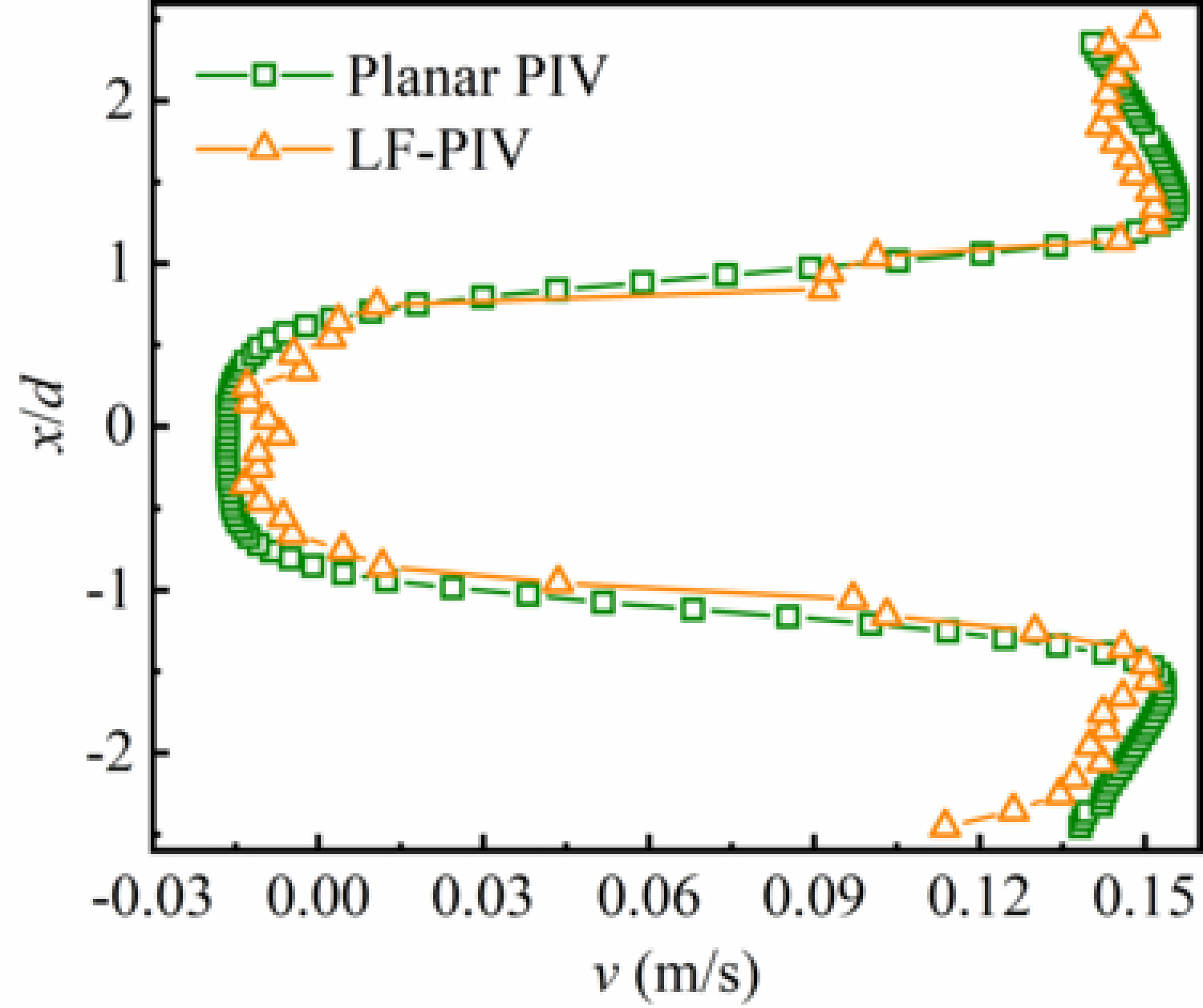
Planar PIV
LF-PIV
2
1
0
-1
-2
x/d
-0.03
0.00
0.03
0.06
0.09
0.12
0.15
v (m/s)

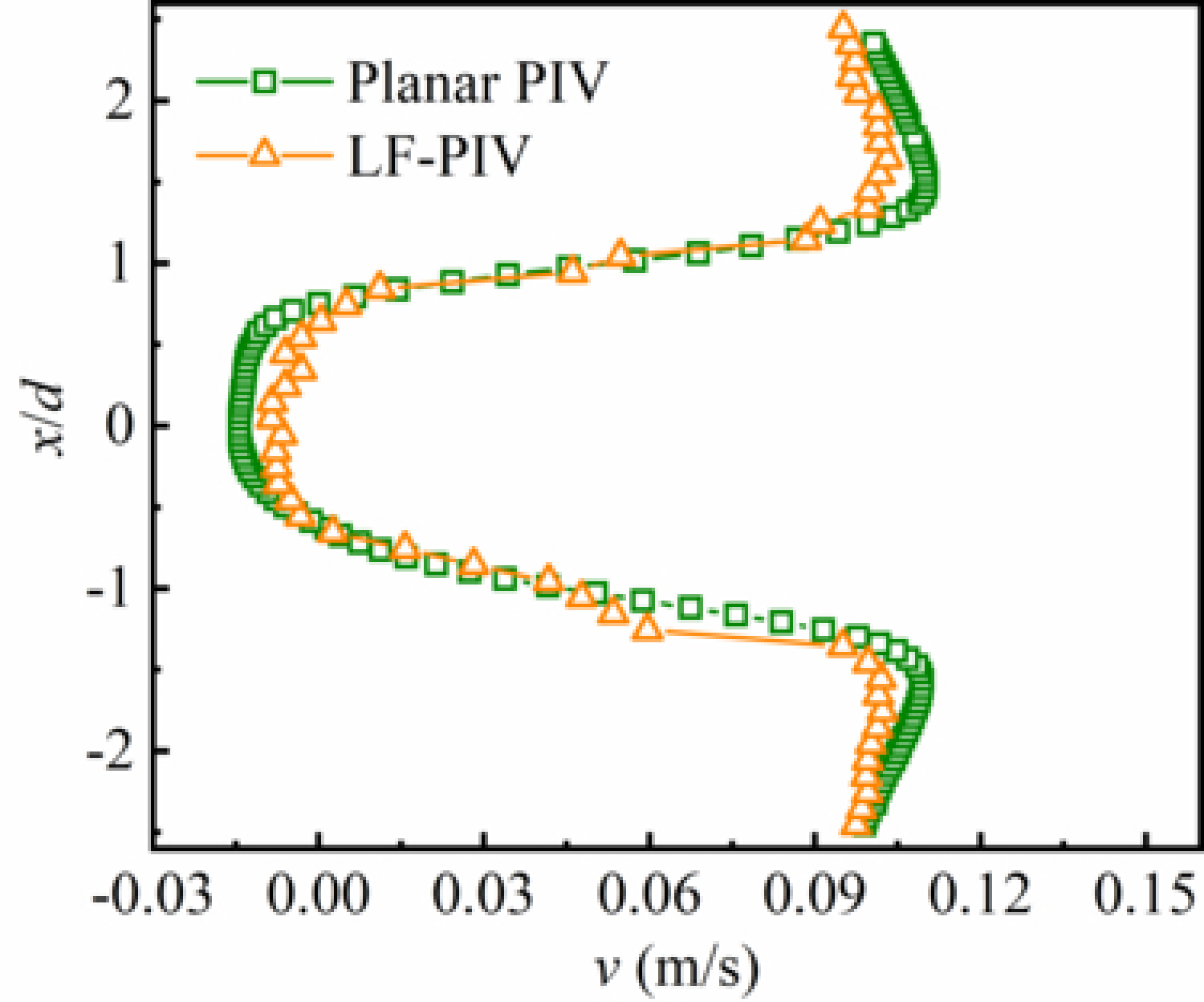
Planar PIV
LF-PIV
x/d
2
1
0
-1
-2
-0.03
0.00
0.03
0.06
0.09
0.12
0.15
v (m/s)

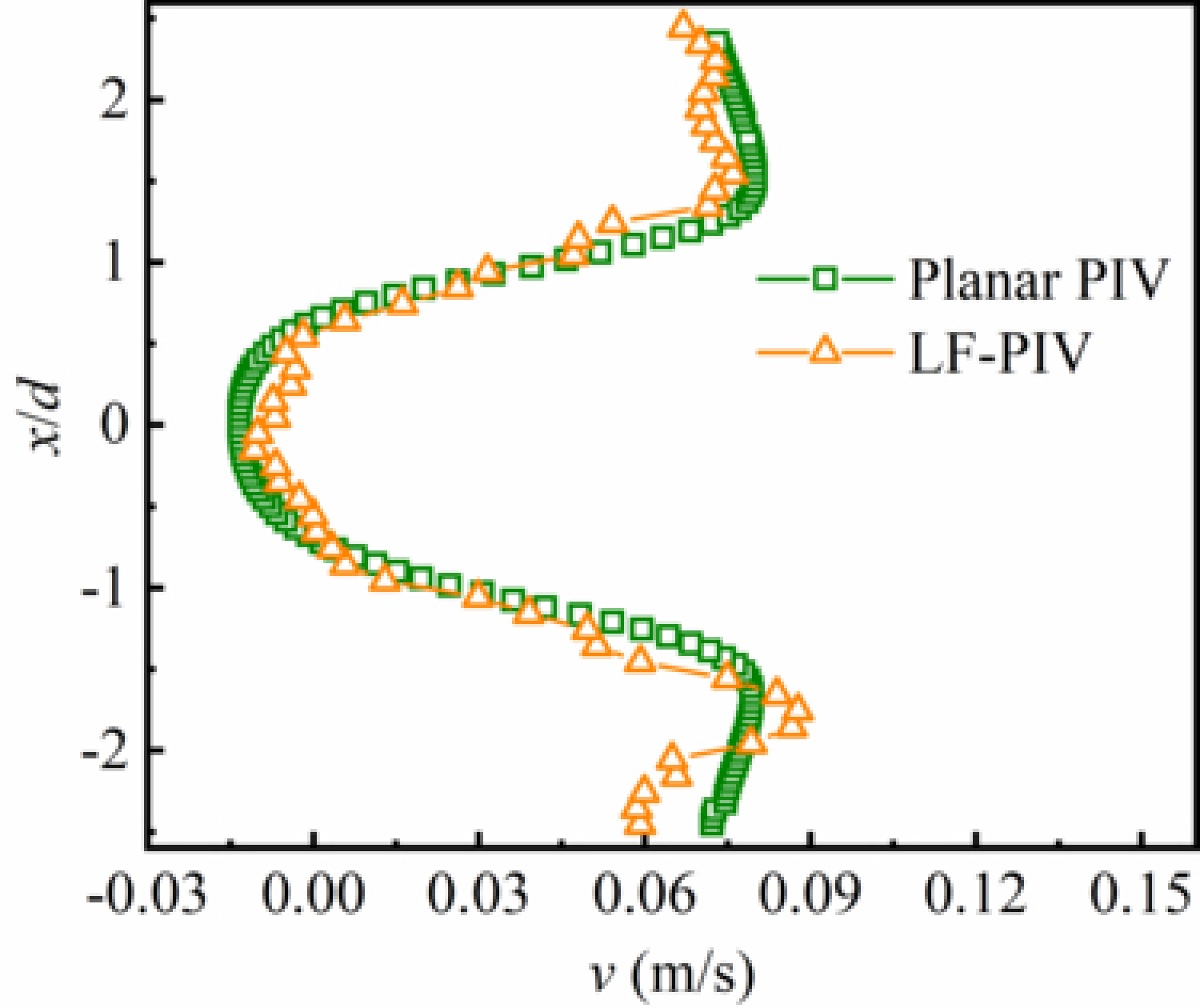
Planar PIV
LF-PIV
x/d
2
1
0
-1
-2
-0.03
0.00
0.03
0.06
0.09
0.12
0.15
v (m/s)

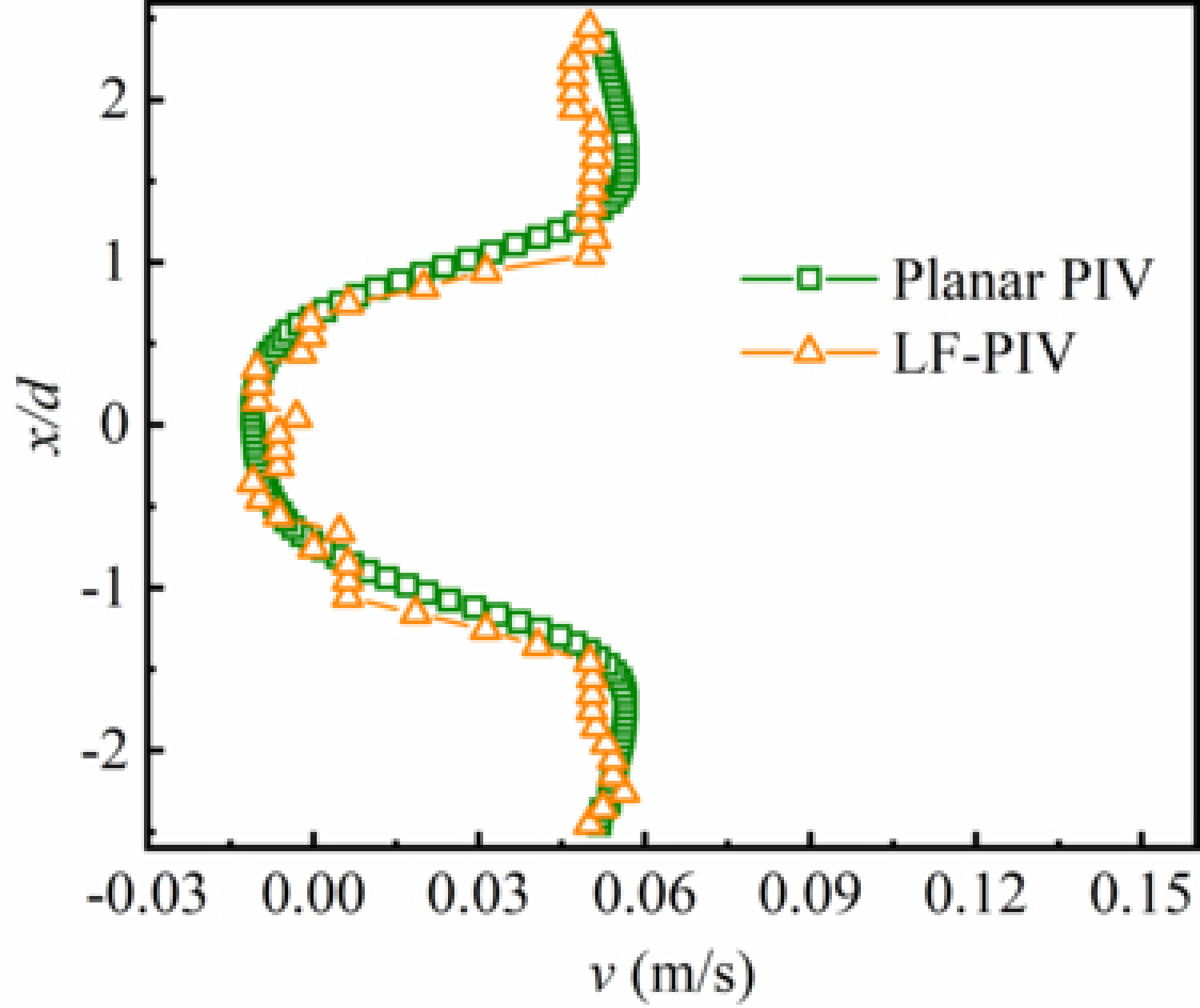
Planar PIV
LF-PIV
x/d
2
1
0
-1
-2
-0.03
0.00
0.03
0.06
0.09
0.12
0.15
v (m/s)

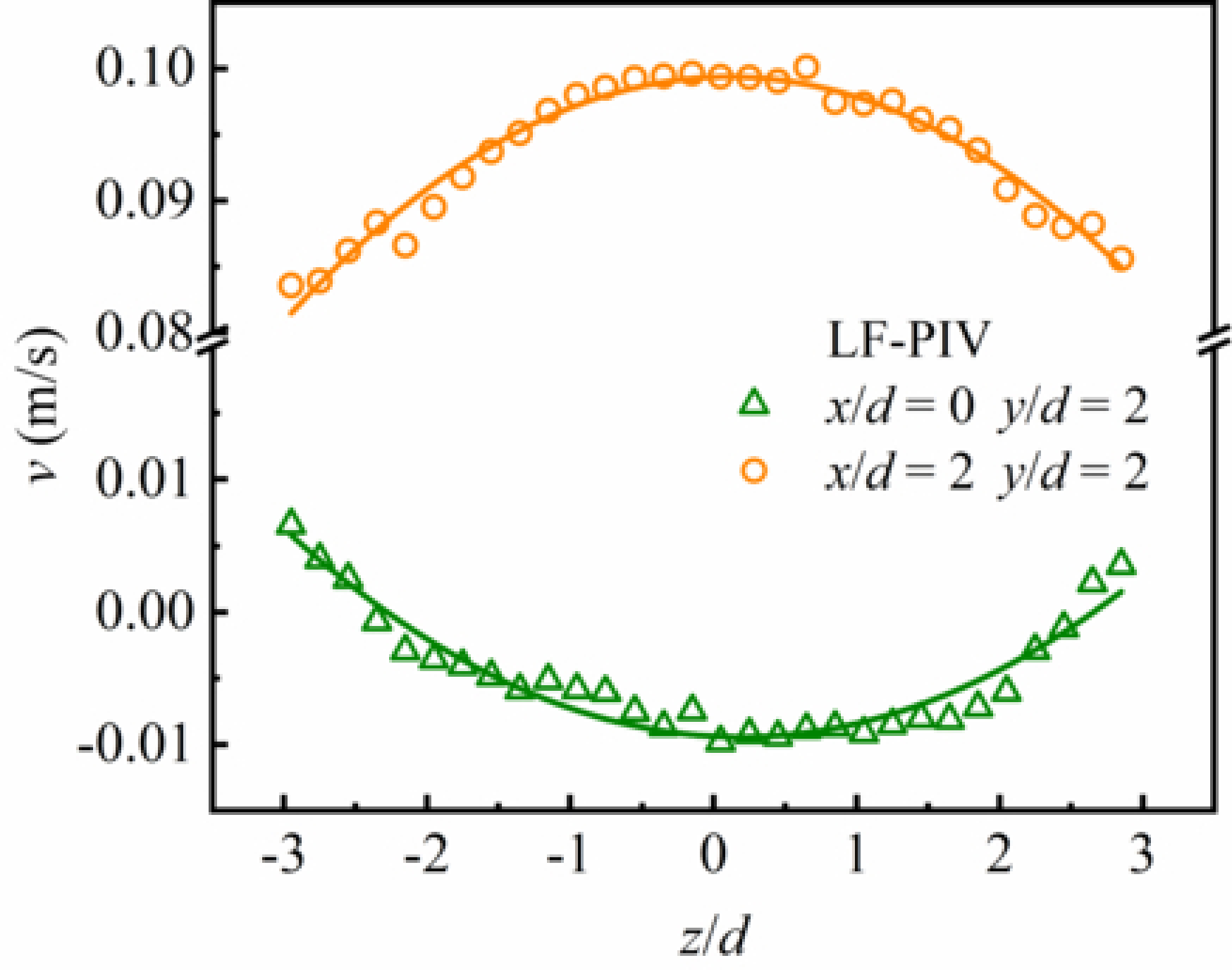
0.10
0.09
0.08
0.01
0.00
-0.01
v (m/s)
LF-PIV
x/d = 0 y/d = 2
x/d = 2 y/d = 2
-3
-2
-1
0
1
2
3
z/d